Novel Electrode Materials and Advanced Electrochemical Diagnostics for Electrochromic Devices

by

Rana Ahmad

A thesis submitted to the
School of Graduate and Postdoctoral Studies in partial
fulfillment of the requirements for the degree of

Master of Science in Materials Science

Faculty of Science

University of Ontario Institute of Technology (Ontario Tech University)

Oshawa, Ontario, Canada

April 2022

THESIS EXAMINATION INFORMATION

Submitted by: **Rana Ahmad**

Master of Science in **Materials Science**

Thesis title: Novel Electrode Materials and Advanced Electrochemical Diagnostics for Electrochromic Devices

An oral defense of this thesis took place on April 7th, 2022 in front of the following examining committee:

Examining Committee:

Chair of Examining Committee	Dr. Helene LeBlanc, Ontario Tech University
Research Supervisor	Dr. Olena V. Zenkina, Ontario Tech University
Research Co-supervisor	Dr. E. Bradley Easton, Ontario Tech University
Examining Committee Member	Dr. Liliana Trevani, Ontario Tech University
Examining Committee Member	Dr. Eric Keske, Trent University
Thesis Examiner	Dr. Yuri Bolshan, Ontario Tech University

The above committee determined that the thesis is acceptable in form and content and that a satisfactory knowledge of the field covered by the thesis was demonstrated by the candidate during an oral examination. A signed copy of the Certificate of Approval is available from the School of Graduate and Postdoctoral Studies.

ABSTRACT

Electrochromic materials (ECMs) are a class of “smart” materials used in a variety of applications due to the ability to alter their optical properties with the application of a potential. For these applications, ECMs are fashioned into electrochromic devices (ECDs). However, commercialization of ECDs are limited due to challenges with cyclic stability and optical durability. Commonly, it is seen that ECM development is vastly investigated, while insight into the overall ECD architecture is limited. In this work, the effect of the counter electrode (CE) and operating potentials were investigated using an Fe (II) terpyridine based complex as the ECM. From this, it was found that by improving the charge-storage properties at the CE and limiting the potential window used, ECD degradation could be minimized. Furthermore, by employing these modifications it was found that the lifetime of these ECDs were able to undergo months of constant cycling, as opposed to days, with further improvement to their optical properties.

Keywords: electrochromic; durability; electrode; impedance spectroscopy; degradation

AUTHOR'S DECLARATION

I hereby declare that this thesis consists of original work of which I have authored. This is a true copy of the thesis, including any required final revisions, as accepted by my examiners.

I authorize the University of Ontario Institute of Technology (Ontario Tech University) to lend this thesis to other institutions or individuals for the purpose of scholarly research. I further authorize the University of Ontario Institute of Technology (Ontario Tech University) to reproduce this thesis by photocopying or by other means, in total or in part, at the request of other institutions or individuals for the purpose of scholarly research. I understand that my thesis will be made electronically available to the public.

Rana Ahmad

STATEMENT OF CONTRIBUTIONS

The work described in Chapter 3 has been published as: Ahmad, R.; Laschuk, N. O.; Ebralidze, I.I.; Zenkina, O.V.; Easton, E.B., Probing the Influence of Counter Electrode Structure on Electrochromic Device Operating Potentials and Performance Using Electrochemical Impedance Spectroscopy. *ChemElectroChem* **2021,** *8* (12), 2193-2204. Doi: https://doi.org/10.1002/celc.202100195. Copyright 2021 Wiley-VCH GmbH. I was responsible for pre-treatment of substrates. I performed the functionalization of screen-printed surfaces with Fe 4'T complex. I synthesized the lithium gel electrolyte. I prepared all electrochromic devices (ECDs) I performed all electrochemical measurements such as cyclic voltammetry (CV) and electrochemical impedance spectroscopy (EIS). I was responsible for all electrochemical data analysis. I prepared all materials and solutions required for 3-electrode cell measurements. I measured all UV-Visible spectra and performed all Spectroelectrochemical measurements. I took all optical images. I independently wrote the first draft of the manuscript, contributed to figure preparation, as well as contributed to changes made during revisions.

The work described in Chapter 4 has been published as: Ahmad, R.; DiPalo, V.; Bell, M.; Ebraldize, I.I.; Zenkina, O.V.; Easton, E.B., Surface-Enhanced Counter Electrode Materials for the Fabrication of Ultradurable Electrochromic Devices. *ACS Applied Energy Materials* **2022**. Doi: https://doi.org/10.1021/acsaem.1c03480. Copyright 2022 American Chemical Society. I was responsible for the preparation of the ITO-50 nanoparticle (NP) paste. I performed the pre-treatment of ITO glass substrates. I performed the screen-printing of the ITO-50 NP paste onto ITO glass substrates. I synthesized the Fe 4'T complex using available 4'-(4-pyridyl)-2,2':6',2"-terpyridine ligand. I synthesized the

lithium gel electrolyte. I performed all Fe 4'T functionalization. I assembled all electrochromic devices. I prepared all materials for electrochemical measurements in liquid electrolyte. I performed all electrochemical measurements such as CV, EIS and galvanostatic charge-discharge (GCD) cycling. I was responsible for all electrochemical data analysis. I performed the following spectroelectrochemical measurements for the Fe 4'T/ITO NPs ECD: varying switching speeds and short-term (10 hours) cycling. I took the majority of photos. I contributed to the writing of the manuscript, figure preparation and changes made during revisions.

ACKNOWLEDGEMENTS

I would like to thank my supervisors, Dr. Olena Zenkina and Dr. Brad Easton for offering their guidance and support throughout these years. You both gave me the opportunity to build confidence in my knowledge and skillsets; something I was unsure of prior to my time in the lab. Despite the midst of my Masters occurring during a pandemic, you were both present and understanding of any resulting struggles and I appreciate that immensely. I would also like to thank my committee members, Dr. Liliana Trevani and Dr. Eric Keske for their aid and suggestions during our meetings, helping to further guide me towards a successful dissertation.

I'd like to thank Dr. Nadia Laschuk for being an outstanding mentor and teaching me everything I needed to know to get to this point. You were an extremely patient and thorough mentor, ultimately helping me gain my own independence in the lab. Furthermore, I'd like to thank Jade Poisson for encouraging me to try my hand at research; I had no intentions of ever taking the path towards academia, but here we are over 2 years later and I'm glad I did it.

I would not have been able to get to this point without the amazing people I've met in the Easton and Zenkina groups. Holly, Nadia, Keenan, Adaobi, Peter, Reza, Vittoria, Mackenzie and others; Some of you have been around longer while others are fairly fresh, but no matter what we've all been able to get along great and have always had fun times in and outside of the office. Especially during this pandemic, you've all played a huge part in maintaining my sanity and I appreciate all the time we've spent together.

I'd like to thank my closest friends; Alisha and Lindsay. You have both been extremely patient with me over these years; I know I was always busy and distant during

my time in school but I have always appreciated you both. Thank you for being so supportive.

I'd like to thank my partner in crime Charlene Fernandez for taking this journey through academia with me. Throughout undergrad and our Masters, you have consistently made me a better person and chemist, while helping me through the most difficult moments of my life. None of this would have been possible without you, and I imagine my life would be entirely different if it hadn't been for that day we were assigned as lab partners.

Most importantly, I'd like to thank my parents for everything they've done to support me. You uprooted your lives and left your families to come to Canada and give my siblings and I a better life. I would not have had any of the opportunities I've had so far if you hadn't made that sacrifice and I hope that I've been able to make you proud of that decision. Thank you for always going above and beyond.

TABLE OF CONTENTS

LIST OF TABLES

CHAPTER 3

CHAPTER 4

LIST OF FIGURES

CHAPTER 1

CHAPTER 2

CHAPTER 3

CHAPTER 4

LIST OF ABBREVIATIONS AND SYMBOLS

4'T	iron (II) 4′-(pyridin-4-yl)-2,2′:6′,2″-terpyridine
AZO	aluminum doped zinc oxide
AC	alternating current
ATO	antimony doped tin oxide
BET	brunauer-emmett-teller surface analysis
C	capacitance
CD	colour difference
C_{dl}	double-layer capacitance
CE	counter-electrode
CPE	constant phase element
CV	cyclic voltammetry, cyclic voltammogram
$E_{1/2}$	redox potential, half-wave potential
ECD	electrochromic device
ECM	electrochromic material
ECP	electrochromic polymer
EDL	electrical double layer
EIS	electrochemical impedance spectroscopy
FTO	fluorine doped tin oxide
GCD	galvanostatic charge-discharge
i	current
ITO	indium tin oxide
ITO-50	ITO coated glass screenprinted with an ITO nanoparticle paste with particles < 50 nm in diameter
IUPAC	International Union of Pure and Applied Chemistry
UPL	upper potential limit
LPL	lower potential limit
LMCT	ligand to metal charge transfer

MLCT	metal to ligand charge ransfer
OD	optical density
PEDOT	poly(3,4-ethylenedioxythiophene)
PSS	polystyrene sulfonate
PEDOT:PSS	mixture of PEDOT and PSS polymers
ProDOT	3,4-Propylenedioxythiophene
PPy	polypyrrole
PMMA	poly(methyl methacrylate)
PVP	polyvinylpyrrolidone
RE	reference electrode
R_{CT}	charge-transfer resistance
$R_{electrolyte}$	electrolyte resistance
R_{ionic}	ionic resistance
$R_{electronic}$	electronic resistance
R_{Σ}	sum of ionic and electronic resistance
SEC	spectroelectrochemistry, spectroelectrochemical
SEM	scanning electron microscopy
SI	supporting information
t	time in seconds
T_b	bleached transmittance
T_c	coloured transmittance
TBAHFP	tetrabutyl ammonium hexaflurophosphate
TLM	transmission line model
WE	working electrode
XPS	X-ray photoelectron spectroscopy
Z	impedance
Z’	real impedance
Z”	imaginary impedance

Z_w	Warburg impedance
ΔOD	change in optical density
η	colouration efficiency
Q	injected/ejected charge
λ	wavelength (nm)
λ_{max}	maximum absorption wavelength (nm)
ω	angular frequency (radians)
Ω	electrical resistance

Chapter 1. Introduction

1.1 Electrochromic Materials

Throughout the years, there has been increasing pressure to develop sustainable, eco-friendly technologies, such as those that decrease our electrical consumption, in order to minimize negative impacts on the environment. In the past decade, it was seen that building energy use in the United States accounted for 41% of total prime energy consumption. Furthermore, 30% of global energy-related CO_2 emissions are linked to energy consumption within the building sector.[1] Therefore, it is important to develop new technologies and sustainable materials that can reduce building energy consumption due to heating, cooling and lighting. One field of research with major applications as environmentally friendly building materials is electrochromic development.

The phenomenon of electrochromism has the capacity to enhance the design of materials and devices we use, as a new class of "smart" materials. By definition, materials that exhibit electrochromic properties are those that are able to exhibit a change in their optical properties (such as colour and transparency) through the application of a voltage.[2] However, electrochromic materials have the added benefit of being easily tunable as opposed to a dependency on a spontaneous external stimulus, such as with thermochromic materials. In addition, these materials are typically able to undergo their electrochromic transitions with very little applied voltage as well as the ability to sustain that state without additional added stimulus, a phenomenon known as electrochromic memory. As a result, electrochromic materials have been heavily investigated for environmentally friendly building materials such as "smart" windows.[3, 4] With commercialization, these materials have the potential to reduce heating and cooling costs with very little electrical input and

negate the need for other shading devices such as blinds and curtains.[5] Additionally, electrochromic materials have the potential to be used for other applications such as wearable technologies and displays.[6]

Electrochromic materials (ECMs) are able to exhibit their colour-changing properties through redox reactions which occur due to an applied potential as a driving force. The change in the oxidation state of the electrochromic material consequently results in a change in colour or opacity for that material. A vast range of compounds can be used to design these ECMs, such as: metal oxides, conjugated conductive polymers, organic molecules and coordination complexes.

Tungsten trioxide (WO_3) is one of the most commonly investigated metal oxides for electrochromic applications, as well as the first well-studied example as described by Deb in 1973.[7] The most common mechanism for WO_3 electrochromism is the insertion/extraction of protons and electrons as denoted by the following equation:[8-10]

$$[WO_3 + xM^+ + e^-]_{bleached} \leftrightarrow [M_xWO_3]_{coloured}$$

Where M^+ can represent a range of cations such as H^+, Li^+, Na^+ and K^+. When a voltage is applied, this drives the movement of electrons and charge-balancing of ions in order to facilitate a colour change to deep-blue. Other metal oxides are also known to show electrochromic properties such as molybdenum and vanadium oxides which are considered "cathodic" oxides as their intense absorbance is achieved through reduction. Alternatively, "anodic" oxides such as nickel oxide achieve strong-colouration through oxidative processes.[10, 11]

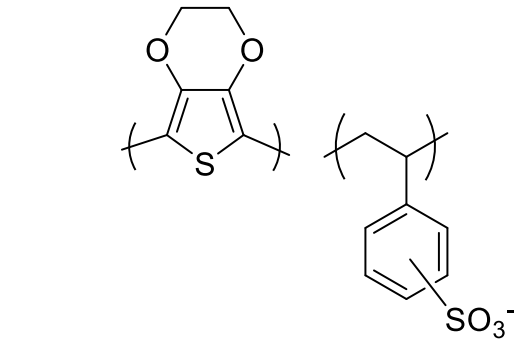

Poly(3,4-ethylenedioxythiophene):Polystyrene sulfonate
PEDOT:PSS

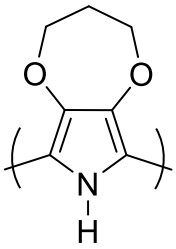

3,4-propylenedioxypyrrole
ProDOP

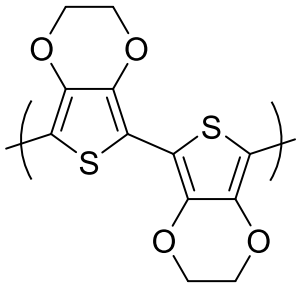

Poly(3,4-ethylenedioxythiophene)
PEDOT

Figure 1.1 Examples of electrochromic conductive polymers

Alternatively, conjugated conductive polymers (or intrinsically conductive polymers) are another popular class of materials being investigated for their electrochromic properties. These materials have inherent conductive properties due to π-conjugated systems allowing for electron delocalisation and movement.[12] In addition to their unique electrical properties, conjugated conductive polymers display unique optical properties as well as the potential for solution-processability;[13] an important trait for commercial scale-up. Examples of these types of polymers are shown in Figure 1.1. Research by Reynolds et al.[14] has shown that N-substituted poly(3,4-propylenedioxypyrrole) can display strong colourations through oxidative processes, with fine tuning of attained colours through polymer blending or formation of co-polymers. More commonly, PEDOT been combined with polystyrene sulfonate (PSS) to form a mixture of the two ionomers known as PEDOT:PSS.[15-17] This

mixture has sustained popularity both for its substantial conductivity and transparency, allowing it to be an effective replacement for more expensive and tedious conductive films, but also for its reversible electrochromism.

Another class of materials frequently investigated are transition-metal-based coordination complexes as these materials demonstrate intense colorations and reversible redox activity with colour tunability through ligand[18] and metal-centre[19, 20] modifications. These colourations commonly arise from charge-transfer interactions between molecular orbitals that are metal and ligand-like in character. A material that displays a transfer of charge density from the metal to ligand-like orbitals displays metal-to-ligand charge transfer absorption (MLCT). Alternatively, a complex where the charge density shifts from ligand to metal-like orbitals is described as ligand-to-metal charge transfer absorption (LMCT). While the stabilization of the metal-centres in coordination complexes varies based on the ligand of choice, polypyridyl complexes are commonly of interest as ligands such as bipyridine and terpyridine (Figure 1.2) can form stable tris[21] and bis[22] coordination complexes with d^6 transition metals. For instance, van der Boom has demonstrated that stable polypyridyl complexes can be formed using transition metals such as iron, osmium, and ruthenium with a wide range of addressable colours.[23]

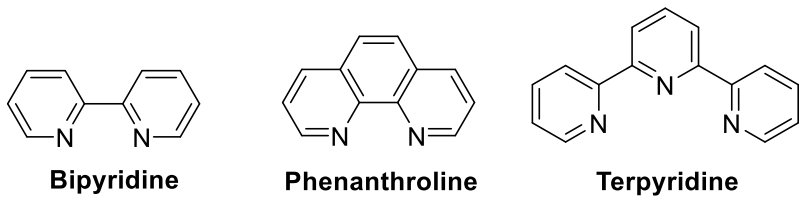

Figure 1.2. Examples of polypyridyl ligands

1.2 Properties of ECMs

In order for an electrochromic material to be a viable candidate for practical applications they must display properties such as: high optical density, high colouration efficiency, fast switching speeds and optical durability. Optical density refers to the contrast ratio between the coloured and bleached (or the alternate colour) state as defined by Equation 1.1.

$$OD = \log\left(\frac{T_b}{T_c}\right) \tag{1. 1}$$

Where T_b is the transmittance in the bleached state and T_c is the transmittance in the coloured state. For electrochromic materials with a single bleached-to-coloured transition state, optical density is determined using the wavelength in which the greatest contrast is achieved (λ_{max}).

Colouration efficiency (denoted by η) is another important parameter as it represents the change in optical density as a function of the injected charge; ideally, the greater the colouration efficiency, the less energy is required to facilitate a significant colour change. This parameter can be described by Equation 1.2:

$$\eta = \frac{\Delta OD}{Q} \tag{1. 2}$$

Where η represents colouration efficiency, ΔOD represents the change in optical density and Q represents the injected or ejected charge. By creating a plot of ΔOD vs Q, the colouration efficiency can be extrapolated from the slope of the linear region.

Furthermore, the response time or switching speeds of electrochromic materials are important to investigate. This can be described using parameters known as bleaching (t_b) and colouring (t_c) times, often described in seconds. When investigating an ECM, this parameter can be investigated by applying a bleaching or colouring potential and recording the amount of time necessary to achieve 95% of the minimum or maximum absorbance. Ultimately, the ideal t_b and t_c values for the material are entirely dependent on the application for which they are used; fast switching times may be required for electrochromic signage whereas slower switching times may be sufficient for applications where switching will not occur frequently.

Lastly, optical durability is a parameter that may be the most important when comparing ECMs. Optical durability refers to the ability of the material to maintain its initial ΔOD even after consistent cycling. This property is especially important for commercialization as it is a necessity for the materials to be able to endure long periods of use without compromising the quality and vibrancy of colours achieved. Additionally, this property describes the ability for the material to consistently switch at certain speeds while obtaining its maximum ΔOD; an observation where there is a decrease in optical density at faster switching speeds may indicate that the the redox-transition occurs too slowly.

1.3 Electrochromic Device Architecture

As previously mentioned, ECMs are materials that change optical properties when a potential is applied. However, in practical use these materials cannot be used alone and must be fashioned into an electrochromic device (ECD); an electrochemical cell which contains all the components necessary for electrochromic transitions to occur. Today, many different ECD architectures have been investigated, but the most basic form of electrochromic device comprises of three major components (Figure 1.3): 1) an electrochromic layer (the ECM), 2) conductive electrodes and 3) an ion conductor/electrolyte layer.

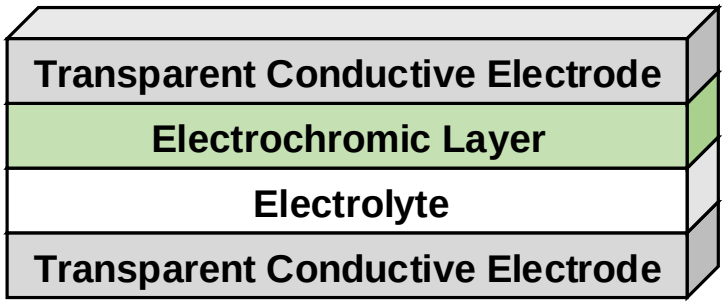

Figure 1.3 Diagram of basic electrochromic device architecture

When incorporated into an ECD, electrochromic materials must be deposited onto an electrically conductive substrate (via physisorption or chemisorption) to create an electrochromic layer. Functionally, the combination of ECM on a conductive substrate acts as the working electrode (WE) within the electrochemical cell.

There are a vast range of electrically conductive electrodes that can be used for ECDs; the ideal substrate is typically dependent on the application of the ECD itself. For example, Indium tin oxide (ITO) coated glass is one of the most common electrode

materials used for ECD design due to its optical transparency and electrical conductivity, resulting in its frequent use for the development of electrochromic windows. The ease with which it can be deposited consistently as a thin film further illustrates its widespread commercial availability. Other alternatives to ITO include fluorine-doped tin oxide (FTO), aluminum-doped zinc oxide (AZO), and antimony-doped tin oxide (ATO) coated glass substrates; all of which present at a lower cost than ITO with variations in properties such as conductivity, transparency, thermal stability and resistivity. Nevertheless, conductive glass substrates present a challenge for the development of flexible or solution-processable ECDs. Consequently, the previously mentioned oxides, as well as silver nanowires and graphene, have been used as coatings on flexible substrates to allow for the development of flexible and wearable optoelectronics. Conjugated conductive polymer coatings have also been investigated, with widespread interest due to their solution processability. These coatings are based on polymers such as: polyacetylene, polypyrrole (PPy), and Poly(3,4-ethylenedioxythiophene) (PEDOT). As mentioned prior, the electrochromic layer is required to be deposited on a conductive substrate in order to behave as the working electrode, however conductive substrates must also be used for the counter electrode (CE); the component that closes the electrochemical circuit and allows for passing of current. Conveniently, a wide range of materials and substrates have the ability to be used within ECD architecture as electrodes where specific properties such as transparency and rigidity can be determined based on the purposes of the device and materials chosen accordingly.

The last fundamental component of an ECD is the ion conductor or electrolyte layer; the component that allows for diffusion of ions between the electrodes to facilitate redox reactions occurring at the ECM interface. Phases of electrolytes include liquid, gel

and solid where solution-based electrolytes have the benefit of increased rates of diffusion and ion transport but may be prone to leakage in solid-state devices, while gel and solid electrolytes have increased practicality in functional devices but suffer from slower ion diffusion rates. Lithium is commonly the ion of choice, particularly for liquid and gel electrolytes, as the small ion size correlates to higher energy density; Lithium triflate, lithium perchlorate and lithium trifluorosulfonamide are typically used as the Li salt precursor. Gel electrolytes are commonly synthesized using a lithium salt, polymers such as polymethyl (methacrylate) (PMMA), polyvinyl pyrrolidone (PVP), or PEDOT and plasticizing agents such as propylene carbonate, in combination with a polar aprotic solvent.

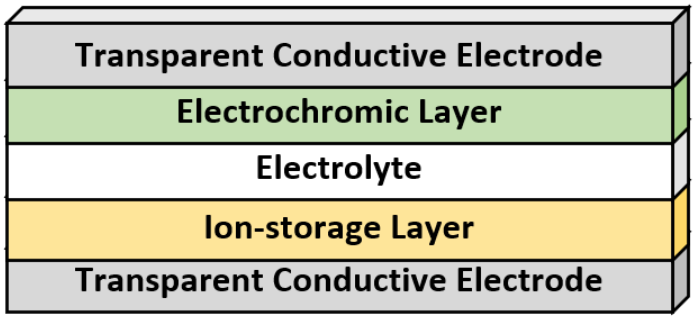

Figure 1.4 Structure of an ECD with an ion-storage layer

In recent years, further adjustments have been made to the typical ECD architecture. Specifically, the incorporation of additional layers in the device structure has been investigated to improve device performance and/or introduce new properties to the device. [24] One such example is the introduction of an ion storage layer (Figure 1.4). Typically, CEs such as ITO coated glass do not exhibit significant charge-storage properties due to their rough surfaces and minimal porosity, ultimately affecting the ability to sufficiently balance the charge present at the WE. As a result, ion storage materials have been added to the ECD

architecture in order to introduce layers that are better able to store ions, which improves switching speeds and device stability. One example of an ion-storage layer is the layer of screen-printed TiO_2 anatase on ITO glass which has high transmittance, but is also able to improve upon charge-storage capabilities at the counter-electrode.[25, 26] Other minimally coloured metal oxides such as Nb_2O_5 have been investigated, an example of which was performed by Mei et al. for the purposes of improving cycling lifetime without affecting the colour contrast of the system which may occur when using metal oxides with significant colouration efficiencies such as WO_3.[27]

1.4 Optical Analysis of Electrochromic Devices

As mentioned in Chapter 1.2, it is a necessity to investigate the optical properties of ECDs for the purposes of comparison and viability for applications. To measure these optical properties, UV-Visible Spectroscopy is employed; this technique allows for the measurement of absorbance, transmittance, or reflectance of a material over a range or single wavelength. In order to measure properties such as the optical density of an ECD, UV-Visible spectroscopic measurements must be coupled with an electrochemical application; this technique is commonly referred to as Spectroelectrochemistry (SEC).

A common SEC technique to measure optical density is to measure the absorbance of an ECD in its varying optical states. *In situ*, a potential is applied to the device to hold it in a particular state (bleached or coloured) and the spectra is measured over the visible region. Afterwards, an alternate potential can be applied to drive the opposing state, and the spectra will be measured. For an ECD that transitions from coloured to bleached, a decrease in absorbance at the λ_{max} will be seen in the bleached state, allowing for determination of optical density using Equation 1.1.

Furthermore, to understand the ability of an ECD to fully switch between redox states, absorbance vs time studies can be performed where the ECD is switching between states at a designated time period. Simultaneously, the absorbance of the system is measured in order to understand how long it takes the system to fully colour or bleach. At longer switching intervals, ECDs are more likely to reach their maximum optical density, however depending on electron transfer rates of the system, faster switching intervals may result in a decrease in optical density due to an insufficient amount of time provided for full redox conversion.

1.5 Electrochemical Performance of Electrochromic Devices

When considering the viability of an ECD, optical and spectroelectrochemical analysis is a fundamental technique to characterize and understand a devices performance and properties. However, these methods are better combined with explicit electrochemical studies, which can provide information about processes that may not be clear within optical data. For instance, understanding operating potentials of a system and probing the presence of side-reactions both prior to and during device cycling is a possibility when incorporating electrochemical analysis. In the following subsection, background on useful electrochemical techniques for electrochromic device design is provided.

1.5.1 Cyclic Voltammetry

Cyclic Voltammetry (or CV) is a commonly used electrochemical technique to study redox properties of an analyte either in solution or adsorbed onto an electrode.[28] In practice, this technique is performed by linearly ramping the applied voltage at the WE at a constant rate (referred to as sweep rate, in mV/s or V/s) and measuring the current at that

electrode to create a cyclic voltammogram. This is typically performed in a 3-electrode cell configuration, with a reference electrode (RE) and counter electrode (CE), where the role of the reference is to provide a stable well-known potential to accurately probe the potential at the working electrode. However, in the solid-state configuration, it is difficult to incorporate a reference electrode in the device architecture which may pose challenges discussed later in this thesis.

CV is a technique that is especially important to the development of ECMs/ECDs as electrochromism is a phenomenon that occurs due to oxidative and reductive processes. As a result, CV can be used to monitor properties of a material such as: electrochemical reversibility, chemical reversibility and half-wave potentials ($E_{1/2}$) of the desired redox couple.

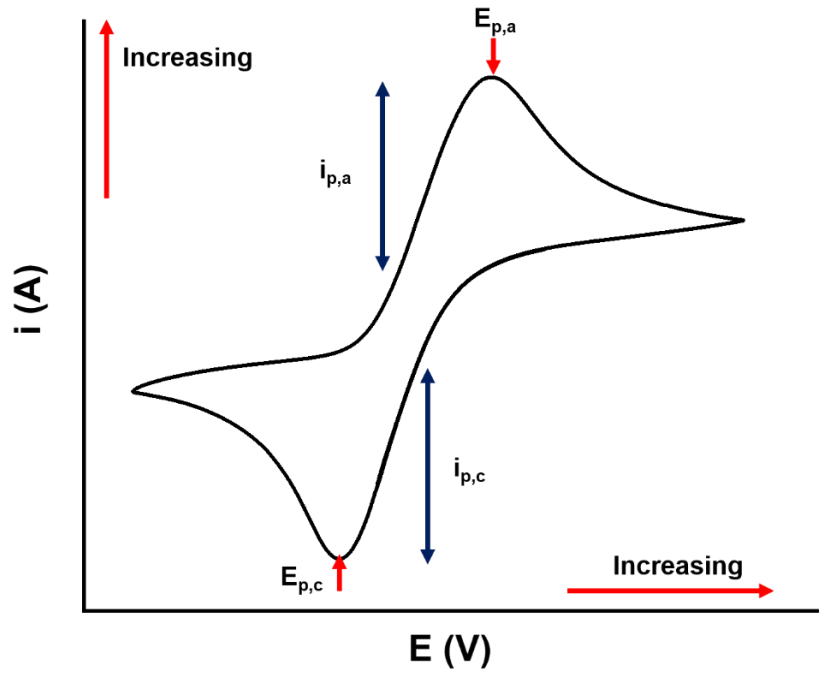

Figure 1.5 Cyclic voltammogram with IUPAC conventions

The cyclic voltammogram shown in Figure 1.5 is displayed using IUPAC conventions, where the x-axis is labelled with increasing potential, thus the peak maximums are a result of oxidative processes while peak minima are a result of reductive processes. Electrochemical reversibility can be determined by the separation between redox peak potentials (ΔE_p) using equation 1.3:

$$\Delta E_p = E_{p,a} - E_{p,c} \quad (1.3)$$

Where $E_{p,a}$ refers to the anodic peak potential and $E_{p,c}$ refers to the cathodic peak potential. Using this equation, if ΔE_p is 59 mV the reaction is considered to be electrochemically reversible. With electrochemical reactions that are more difficult to drive, ΔE_p will increase due to the need for more positive and negative potentials. Chemical reversibility can be determined from anodic and cathodic peak currents ($i_{p,a}$ and $i_{p,c}$ respectively) where the ratio of these currents should be close to or equal to 1 in order to be considered chemically reversible. Significant variation between the anodic and cathodic peak, or even the loss of a reverse peak may suggest the production of a species unable to participate in the redox reaction.

Half-wave potentials ($E_{1/2}$) of a redox couple can be determined simply by calculating the average of the peak anodic and peak cathodic potentials, as described in equation 1.4:

$$E_{1/2} = \frac{E_{p,a} + E_{p,c}}{2} \quad (1.4)$$

$E_{1/2}$ values can be described as a fingerprint for an electrochemical reaction under a specific set of conditions. Variations in $E_{1/2}$ can be seen for the same electrochemical reaction if

there are changes in conditions such as electrolyte, concentration and temperature. With respect to ECDs, $E_{1/2}$ values allow insight into the magnitude of potential required to drive the colour-changing process, while also being required for other electrochemical measurements where processes occurring at the redox potential are being investigated.

1.5.2 Electrochemical Impedance Spectroscopy

An additional electrochemical technique, yet one that is not fully exploited in many cases, is electrochemical impedance spectroscopy (EIS). EIS is a powerful method of analysis that allows for detailed insight into the properties and behaviour of electrode materials and the transformations occurring at their interfaces. Aside from the requirement of instrumentation to allow for impedance measurements, EIS is a technique that can be performed on any electrochemical cell with no changes required to the cell configuration. Despite this, EIS is a technique that is not commonly seen in the literature pertaining to the development of ECDs therefore the basics of this technique will be outlined in this section with detailed examples of its use shown in the proceeding chapters.

In practice, impedance measurements are performed by applying a small AC perturbation (commonly 5 mV) superimposed over a fixed DC bias potential. The frequency of the system (in Hz) is scanned from high to low; resulting in varying responses relating to internal processes. Impedance (Z), otherwise known as the ability for a material to resist alternating current (described as a vector sum of resistance and reactance), is measured over the range of frequencies and in practice, data such as real (Z') and imaginary (Z") impedance is the output. In short, real impedance can be described as the resistive contribution while imaginary impedance can be described as the contribution from

reactance. A graphical representation of Z' vs -Z" is called a Nyquist plot, an example of which is shown below in Figure 1.6.[29]

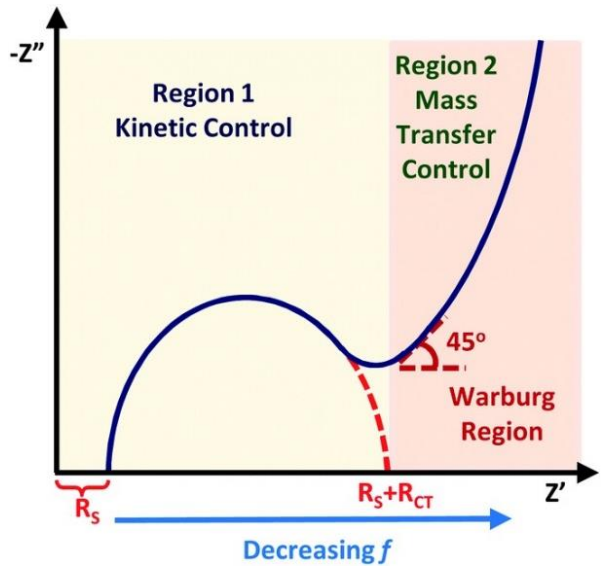

Figure 1.6 Example of a Nyquist plot. Reprinted with permission from Laschuk, N. O.; Easton, E. B.; Zenkina, O. V., Reducing the Resistance for the Use of Electrochemical Impedance Spectroscopy Analysis in Materials Chemistry. RSC Advances **2021,** 11 (45), 27925-27936.

It is possible to extract characteristic features from a Nyquist plot, which can then be related to the internal processes of the system. As an example, solution or electrolyte resistance (R_s) can be quantified as the x-intercept value of the Nyquist plot. For electrochemical cells or ECDs using a liquid electrolyte it is common to see lower values of electrolyte resistance, however with the incorporation of gel and solid electrolytes with larger diffusion layers, the electrolyte resistance typically increases. At the mid to high-frequency region of the Nyquist plot, it is possible to see a semi-circle arc feature that is characteristic of charge-transfer resistance (R_{ct}) processes; behaviour that is seen when there is a rate limitation with ion transfer between the electrode-electrolyte interfaces. Commonly, this is seen when applying a DC potential that drives a faradaic reaction; in Chapter 1.5.2,

determination of $E_{1/2}$ values from cyclic voltammograms were described and are commonly used as a DC bias for EIS to probe behaviour at that potential. However, if the redox reaction occurs rapidly, the charge-transfer resistance arc will often be minuscule or absent. Directly proceeding this region (if present) is the Warburg region; the region at which diffusion and mass transport behaviour is recognized. In an ideal case, a linear region with a 45-degree angle is present which typically trends linear as frequency decreases. This vertical, linear response is typically indicative of capacitive behaviour while deviations can be indicative of non-ideal or resistive processes. This data can also be modelled after electrochemical circuits through simulation and circuit fitting measurements; the two models discussed in this thesis being the Randles-type circuit and the Transmission line model (TLM), further described in Chapter 3. Although these two models are discussed, many other equivalent circuit models can be used to describe an electrochemical system, all dependent on the materials present and their roles.

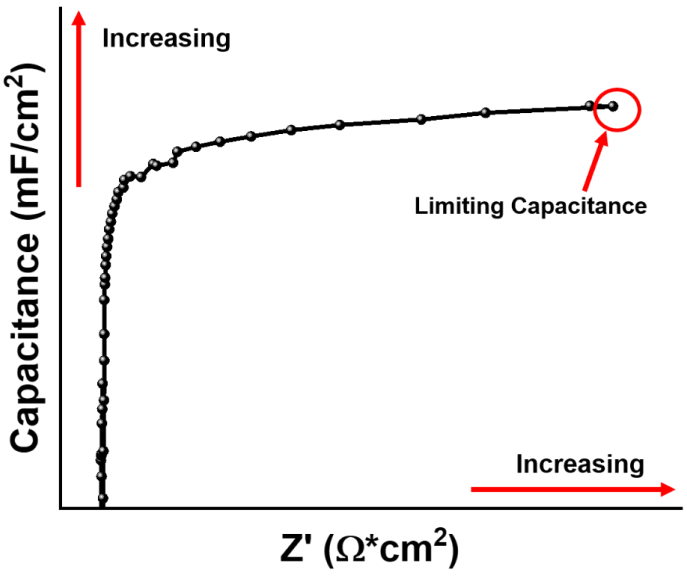

Figure 1.7 Example of a capacitance plot, produced from experimental EIS data

1.6 Challenges in the development of durable ECDs

Despite the growing interest in electrochromic materials, cycling stability and performance of electrochromic devices remains a major barrier before these devices are able to see widespread use in the future. As mentioned in Chapter 1.3, a typical electrochromic device is comprised of the electrochromic layer, an electrolyte or ion conductor and transparent conductive electrodes. In ECD design, it is common to see transparent conductive glass such as ITO coated glass used as a counter-electrode without further modifications. ITO is known to have poor charge-storage capabilities, which leads to issues with charge compensation[30] particularly in an ECD where there are commonly only two electrodes; the WE and CE.

For research purposes, it is common to use ITO as it boasts high conductivity, an important factor for the electrochemical device, as well as high transparency; a feature necessary for the development of electrochromic windows. However, there are significant challenges when using ITO for devices that require long-term operation. In a 2-electrode cell configuration, a CE without a charge-storage layer such as ITO coated glass may need to reach more anodic and cathodic potentials than desired in order to compensate for the potential at the working electrode. For short cycling periods this may not be an issue, but over time this electrode polarization can lead to adverse reactions within the cell that can ultimately cause the ECD to fail prematurely through degradation. One such example seen in the literature is the ability for ITO to undergo irreversible reduction reactions. In the work performed by Liu et al, ITO was observed to undergo electrochemical reduction to form metallic indium and tin; this reduction creates a metallic surface film and reduces the transparency and conductivity of the electrode.[31] Commonly, it is seen in the literature that

an ECD will be reported to have a loss in optical density and decay in performance without a clear explanation as to the mechanisms that cause it; in the case of ECDs that incorporate ITO coatings, this irreversible reaction may be to blame. Additionally, Macher et al. have shown that irreversible ITO reduction is a limitation in the development of flexible ECDs, specifically, they describe a decrease in cycling stability due to ITO thin film dissolution and metallic indium particle formation.[32] Since this reduction is voltage-induced, their efforts involved adjustment of electrode potentials through narrowing of the voltage window which was ultimately able to prevent ITO reduction and improve cycling stability and light transmittance of the ECD. In a study performed by Shen et al.[30], researchers eloquently state that "…an ECD is only as good as its weakest component and that the counter electrode plays a critical role in virtually every property of an electrochromic device". This is demonstrated in their work where they have shown that electrochromic polymer (ECP) based ECDs incorporating counter-electrodes of varying charge-storage capabilities are able to improve switching stability of the devices without a noticeable decrease in contrast; further suggesting that electrode degradation is the culprit of device instability, rather than ECP degradation.

1.7 Thesis Objectives

As a result of the current challenges faced with ECD performance, the objective of this research is to propose a systematic method towards the rational design of ultra-durable electrochromic devices through optimization of the counter-electrode. In current literature, there is an emphasis on the development of high contrast ECMs with exceptional optical properties, but a lack of research on the synergetic relationship between all components in an ECD. It is clear that device performance and long-term stability remains a challenge and

is a major road-block towards mass scale-up and eventual commercialization. As a result, by creating a systematic approach to improving and understanding ECD architecture, while simultaneously understanding the behaviour behind degradation mechanisms, ECDs with increased cycling lifetimes may be developed. Previously in our group, we have shown that stable octahedral complexes can be made through the use of a 4'-(4-pyridyl)-2,2':6',2"-terpyridine complex (4'T) and transition metals such as Osmium, Cobalt and Iron.[18-20] Furthermore, previous work has shown that a high-surface area ITO nanoparticle support can be used as a templating layer for the monolayer deposition of these transition metal complexes, creating robust ECMs with vivid optical properties. The research presented within this thesis is an extension of this work, focusing on the Fe (II) 4'T ECM for the purpose of understanding the degradation processes previously seen with ECD cycling when using a typical rough ITO substrate at the counter electrode. Furthermore, this research aims to determine whether simple electrochemical testing methods such as CV and EIS can be used to diagnose and prevent ECD degradation, as well as define a relationship between CE properties and their effect on ECD stability through comparison of non-porous and highly porous substrates. Lastly, this work investigates the effect of the abovementioned novel materials on the long-term performance of ECDs.

Chapter 2 will describe in-depth the experimental techniques and methods used to synthesize and prepare the materials investigated in this research. Chapter 3 will describe work where it was determined that ITO substrates with highly porous and capacitive modifications had a significant improvement in performance compared to unmodified ITO glass as a counter electrode, preventing electrode and electrolyte degradation and improving ECD performance. Chapter 4 is an extension of that work, describing how the

modification of solely the counter electrode can allow for a significant increase in the cycling lifetime of the ECDs, from days to weeks. Furthermore, this work indicates that by minimizing degradation of components such as the electrode and the electrolyte, degradation pathways pertaining to the electrochromic material can be observed which could not be seen when alternate degradation mechanisms were dominant. Chapter 5 will summarize the findings of this thesis and describe its importance, while providing future work which may be performed as an extension of this research.

Chapter 2. Experimental Methods

2.1 Materials and Solvents

Chemicals used in this work were purchased from Millipore, Sigma-Adrich, or Alfa Aesar and utilized without any further purification. Solvents were purchased from VWR, ACP and Thermo Fisher Scientific. ITO coated glass slides were purchased 5 × 25 × 1.1 mm, R_s = 5-15 Ω/sq were purchased from Delta Technologies. Reactions requiring an inert N_2 atmosphere were performed in an MBraun glovebox with less than 5 ppm of H_2O and O_2. Glassware used for these reactions were left to dry in an oven overnight at 130° C before use.

X-ray photoelectron spectroscopy (XPS) analysis was performed by Dr. Peter M. Brodersen from the Ontario Centre for the Characterization of Advanced Materials at the University of Toronto using a Thermo Fisher Scientific K-Alpha equipped with a monochromated Al Kα X-ray source. Scanning electron microscopy (SEM) images were obtained by Dr. Iraklii I. Ebralidze using a HitachiFlexSEM 1000. Roughness and profilometry measurements were performed by Dr. Iraklii I. Ebralidze using Profilm3D

Surface Profiler by Filmetrics (Filmetrics) equipped with 20× Nikon CF IC Epi Plan objective.

2.2 Synthesis of Fe (II) 4'-(4-pyridyl)-2,2':6',2"-terpyridine (Fe 4'T) complex

The 4'-(pyridin-4-yl)-2,2':6',2"-terpyridine ligand used for the complex synthesis was synthesized by former Ph.D. candidate Nadia Laschuk and undergraduate student Mackenzie Bell according to a previously published synthetic scheme[33] (Figure 2.1).

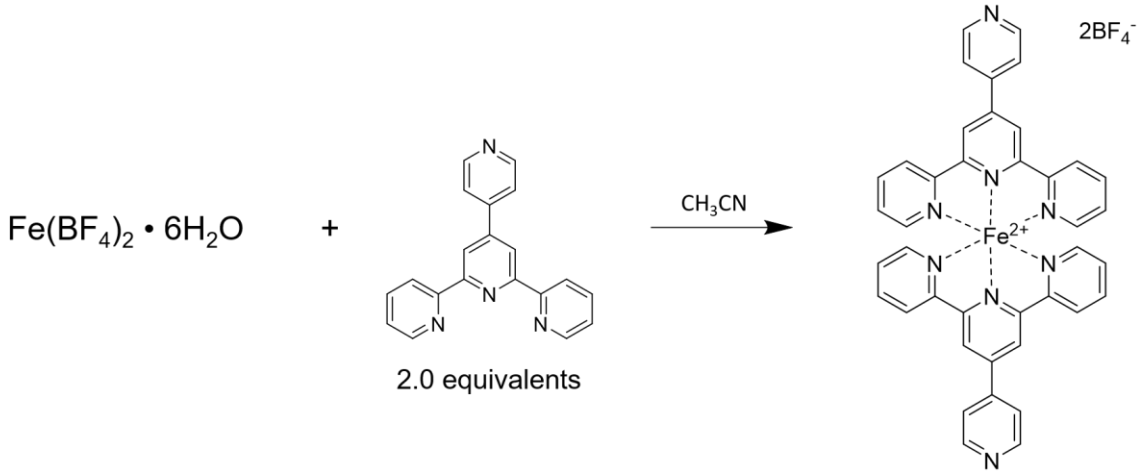

Figure 2.1. Scheme for the synthesis of Fe (II) 4'- Fe (II) 4'-(4-pyridyl)-2,2':6',2"-terpyridine (Fe 4'T) complex

The Fe 4'T complex was synthesized from a previously published procedure[33] and is described in Figure 2.1. In a clean, dry sample vial, 4'-(pyridin-4-yl)-2,2':6',2"-terpyridine ligand and iron (II) tetrafluoroborate hexahydrate were combined in a 2:1 molar ratio, under air, dissolving the compounds in a minimum amount of acetonitrile. Upon dissolution, the solution quickly changes to a dark purple colour. With brief stirring, the solvent was then removed using rotary evaporation and the complex was used without any further purification.

2.3 Pre-treatment of ITO coated glass substrates

Commercially sourced ITO coated glass substrates were pre-treated with a basic piranha solution in order to remove any organic surface contaminants. The basic piranha consists of a 1:5:1 solution NH_4OH:H_2O:H_2O_2. First, a solution of ammonium hydroxide in Type 1 deionized water was made. This solution was heated to 60°C after which it was removed from heat. Hydrogen peroxide was then added and substrates were submerged in the solution for 15 minutes. Afterwards, the substrates were rinsed 3 times with deionized water then 3 times with isopropyl alcohol and stored in an oven at 110 °C until required for use.

2.4 Preparation of ITO-50 NP paste

ITO paste with a nanoparticle size of 50 nm or smaller in diameter was made using a previously published procedure from our group.[18, 34] The paste was prepared by combining 0.375g of commercially available ITO nanoparticle powder, 1.6 g of 7.5% polyvinyl butyral in anhydrous ethanol, 0.375 g of 2% sodium docusate in ethanol, 70 µL of 2,2-methoxyethoxyacetic acid, 15 µL of Disperbyk 111, 1.06g of propylene glycol, 36 µL of 3% glycerol and 30 mL of anhydrous ethanol in 75 mL agate jars containing 6 mm beads. The mixture was combined using a PQ-N04 planetary ball milling system by Across International for 24 hrs at a speed of 200 rpm. Afterwards, the mixture was transferred to vials and dried down using rotary evaporation to obtain a paste.

2.5 Screen-printing of ITO-50 NP paste on pre-treated ITO glass substrates

The above-mentioned ITO-50 NP paste was screen-printed[34] onto ITO coated glass substrates using a 90T 10 × 10 mm polyester mesh obtained from Mismatic, Italy. Each layer was relaxed with anhydrous ethanol for 30 s and then left to heat over a hot plate at medium heat for 5 minutes or until dry. This was repeated to achieve an approximate layer thickness of 7μm (~4 layers of paste screen-printed). After the desired paste thickness was achieved, the films were annealed in a Fisher Scientific programmable muffle furnace at 500 °C for 1 h, then 600 °C for 1 h. Afterwards, the films were left to cool to room temperature. SEM and Optical 3D profilometry of the screen-printed supports are shown in Chapter 3 SI Figure 3.8.

2.6 Surface functionalization of ITO-50 substrates with Fe 4'T complex

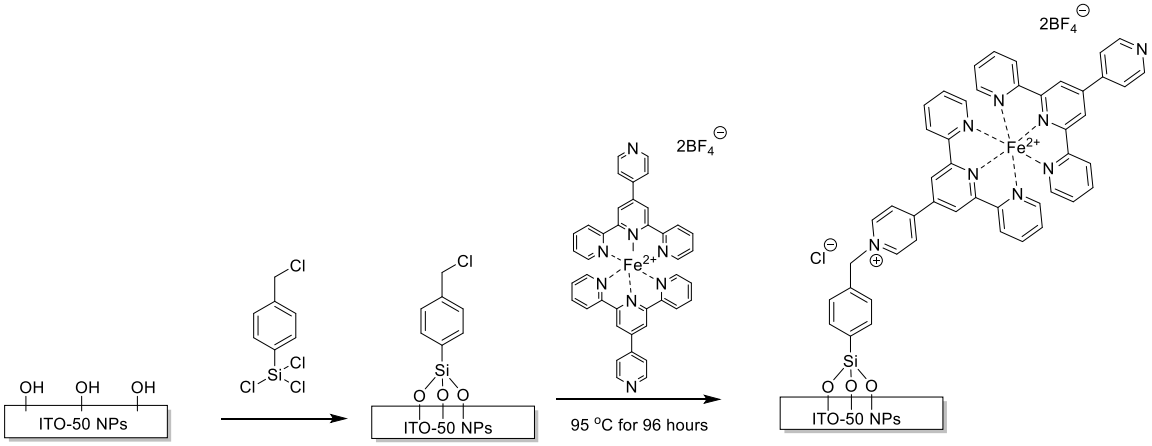

Figure 2. 2. Scheme for the functionalization of ITO-50 NP substrates with Fe 4'T complex

The ITO-50 substrates were functionalized using an adapted literature procedure[35, 36] as described in Figure 2.2. Due to air and moisture sensitivity, the functionalization was performed in a glovebox with a nitrogen atmosphere. Screen-printed ITO-50 substrates

were brought into the glovebox along with clean, dry glassware. In the glovebox, each substrate was placed in a 20 mL sample vial. ~20 mL of dry hexane was added to each vial, along with 0.2 mL of trichloro(4-(chloromethyl)phenyl) silane. The substrates were left to sit in the solution for 20 min, after which they were rinsed 3 times with dry hexane and 3 times with anhydrous acetonitrile. After silane templating, the substrates were distributed each to borosilicate pressure tubes, where 9 mL of a 0.4mM solution of the Fe 4'T complex in anhydrous acetonitrile was added. The pressure tubes were then sealed within the glovebox and brought out to heat for 96 hours at 95°C. After heating, the solution was removed and the slides were rinsed 3 times with acetonitrile, 3 times with hexane and left to air dry.

2.7 Synthesis of lithium gel electrolyte

The lithium gel electrolyte was synthesized based on a procedure published by van der Boom.[37] 700 mg of poly(methyl methacrylate) (PMMA), 300 mg of Lithium trifluoromethane sulfonate, 8.9 mL of anhydrous acetonitrile and 1.7 mL of propylene carbonate were combined in a dry sample vial under a nitrogen atmosphere with stirring. The electrolyte was left to purge overnight under N_2, and stored with stirring.

2.8 Assembly of electrochromic devices

Assembly of all ECD configurations were the same, with the only variance being the substrate used for the counter electrode. ~0.1 mL of the lithium gel electrolyte was dropcast on the active portion of one of the electrodes for the ECD. The film was placed in a 110° C for approximately 5 minutes, at which point it was removed. The active portion of the secondary electrode was then used to sandwich the gel electrolyte and merge the two

electrodes together, which was further held with transparent tape. Copper tape was added to the conductive side of each electrode to allow for easy attachment of electrical leads. Heat shrink or electrical tape was used on the interface of the electrode and copper tape to prevent electrical noise.

2.9 Electrochemical measurements in a 3-electrode cell configuration

All electrochemical measurements (both in the 3 and 2 electrode configuration) were performed using a Solartron Analytical 1470E multi-channel potentiostat with a Solartron 1260 Frequency analyzer. 3-electrode measurements were performed in a Bio logic plate evaluating cell with a platinum (Pt) counter electrode, $Ag/AgNO_3$ (0.01) as the reference electrode and the investigated electrode as the working electrode. The liquid electrolyte used was a 0.1M solution of tetrabutyl ammonium hexafluorophosphate (TBAHFP) in acetonitrile. A 0.1M solution of Ferrocene (Fc) in the previously mentioned electrolyte was used for reference electrode calibration, where all potentials obtained in the electrochemical measurements were adjusted to Fc/Fc^+. CVs were measured from 0 V to 2 V at a 50 mV s^{-1} scan rate.

2.10 Electrochemical measurements in a 2-electrode cell configuration

In the 2-electrode cell configuration (solid-state ECD), the WE was the Fe 4'T functionalized ITO-50 substrate, while the CE used is dependent on the configuration of the system. Systems with unmodified ITO glass, ITO-50 on ITO glass and an Fe 4'T film as the counter electrode were all investigated within this thesis.

EIS was performed from 80,000 Hz to 0.1 Hz with an AC amplitude of 5 mV. The DC biases used for EIS were based on double-layer capacitive regions were no faradaic

processes were observed as well as at the $E_{1/2}$ for the redox process. The uncompensated resistance (also referred to as electrolyte or solution resistance) was subtracted from all EIS plots.

2.10.1 Cyclic Voltammetry

CVs measurements were performed at a scan rate of 50 mV s^{-1}. For the determination of optimal potential windows (as described in Chapter 3), CVs in the solid-state ECD configuration were initially measured at a wide-potential range (-1V to 3V). The upper limit potential was held constant while the lower limit potential was varied by 100 mV steps; this was done to determine the ideal lower limit potential for subsequent measurements. Afterwards, the chosen lower limit potential was held constant while CVs were measured with decreasing upper limit potentials with 100 mV step variations. The potential window chosen was based on a window that allowed for full Fe^{2+}/Fe^{3+} redox conversion while eliminating any peaks correlating to unwanted side reactions.

2.10.2 Chronoamperometry

Chronoamperometry was employed for long-term cycling measurements as well as during Spectroelectrochemical measurements. The optimal potential windows determined were used as upper and lower limit potentials for square-wave cycling, where the ECD was held at the lower limit potential for 60 s followed by the upper limit potential for 60 s (a total of 120 s for 1 full cycle).

2.10.3 Electrochemical Impedance Spectroscopy

EIS was performed from 80,000 Hz to 0.1 Hz with an AC amplitude of 5 mV. The DC biases used for EIS were based on double-layer capacitive regions were no faradaic processes were observed as well as at the $E_{1/2}$ for the redox process. The uncompensated resistance (also referred to as electrolyte or solution resistance) was subtracted from all EIS plots by extracting the x-intercept from the Nyquist plot. EIS was performed periodically during long-term cycling measurements of ECDs.

R_Σ (the sum of ionic and electronic resistance) was determined through intersection of slopes for the Warburg region and the mid-low frequency region of the Nyquist plot (Figure 2.3).

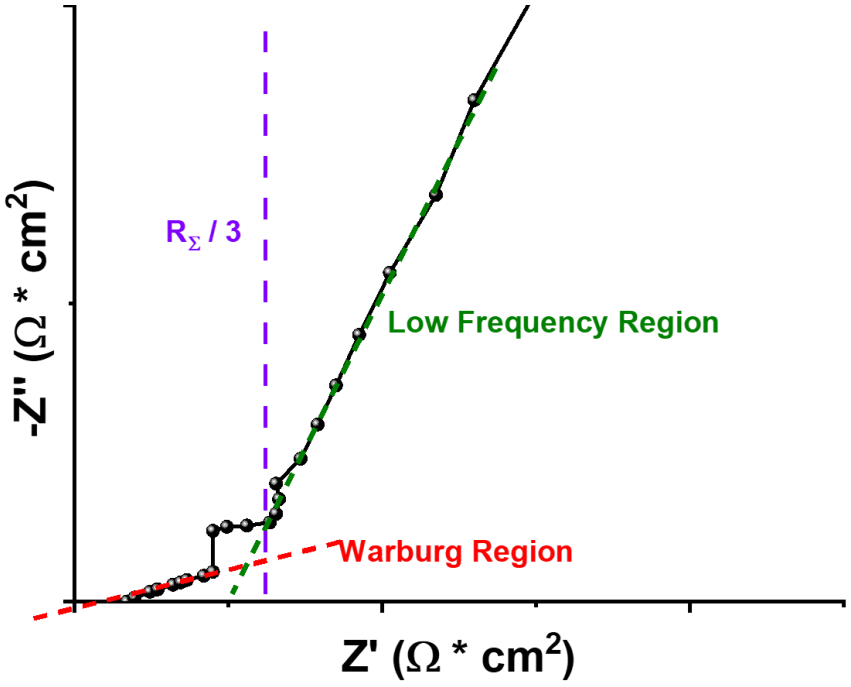

Figure 2. 3. Determination of R_Σ from a Nyquist plot

As described in Chapter 1.5.2, capacitance plots can be obtained from EIS measurements, requiring conversion of data using the following equation where ω refers to the angular frequency (in radians):

$$C = -\frac{1}{\omega Z''} \quad (2.\ 1)$$

Limiting capacitance values were determined from capacitance plots at the lowest frequency data point obtained (0.1 Hz).

2.10.4 Galvanostatic Charge-Discharge

GCD measurements were performed at current densities of 0.06, 0.07, 0.08, 0.09 and 0.1 mA/cm^2. GCD curves were obtained by charging and discharging ECDs from 0 V to 2 V at different applied currents for a total of 10 charge-discharge cycles. GCD capacitance was determined using the following equation:

$$C = \frac{i\Delta t}{VA} \quad (2.\ 2)$$

Where i refers to the applied current, Δt is the time of discharge, V is the charging window and A is the area of the WE surface.

Capacitance retention measurements were performed using a current of 0.06 mA/cm^2 for a balance between charge-discharge time and maximum capacitance. Capacitance retention was performed for a total of 6000 charge-discharge cycles, from 0 V to 2 V.

2.11 Optical measurements

Optical measurements were performed using a PerkinElmer Lambda 750S Diffuse Reflectance UV-Vis Spectrophotometer. Fe 4'T films were characterized post-functionalization using the ScanningQuant program and measuring a spectrum from 320 to 800 nm; the λ_{max} for the Fe 4'T film is 600 nm.

2.11.1 Spectroelectrochemistry

Spectroelectrochemical analysis was performed using the abovementioned spectrophotometer in combination with the Solartron Analytical 1470E potentiostat. To determine the effect of applied potential on solid-state ECD absorbance, UV-Vis spectra were measured from 320 nm to 800 nm while holding the ECD at varying potentials.

To determine the optical switching speed of the ECDs, the wavelength of the spectrophotometer was fixed to 600 nm and absorbance was measured as a function of time using the TimeDrive program. Chronoamperometry was used to hold the device at the upper and lower limit potentials for 60, 30, 15, 7.5, 3.25 and 1.5 s holds. 30 switching cycles were performed for each switching speed. Spectroelectrochemical cycling was determined at 30 s holds for 10 hours, resulting in a total of 600 cycles.

Chapter 3. Probing the influence of counter electrode structure on electrochromic device operating potentials and performance using electrochemical impedance spectroscopy

3.0 Preface

Reproduced with permission from Ahmad, R.; Laschuk, N. O.; Ebralidze, I.I.; Zenkina, O.V.; Easton, E.B., Probing the Influence of Counter Electrode Structure on Electrochromic Device Operating Potentials and Performance Using Electrochemical Impedance Spectroscopy. *ChemElectroChem* **2021,** *8* (12), 2193-2204. Doi: https://doi.org/10.1002/celc.202100195. Copyright 2021 Wiley-VCH GmbH.

3.1 Abstract

The paper reports a general methodology for the rational tuning and optimization of electrochromic devices (ECDs) that are based on a monolayer of Fe (II) (4'-(4-pyridyl)-2,2':6',2"-terpyridine)$_2$ complex (Fe 4'T) covalently embedded onto a screen-printed high-surface area indium tin oxide working electrode. We demonstrate that the nature of the counter electrode and the resulting device configuration could drastically improve the long-term stability of the ECD. We show that the replacement of the flat ITO/glass electrode with a high surface area ITO electrode or the use of symmetrical working and counter electrode architecture leads to a much longer performance of the device. We propose a methodology to determine optimal operating conditions for ECDs by fine-tuning the lower and upper operation potentials. In addition to using traditional cyclic voltammetry (CV), we utilize electrochemical impedance spectroscopy (EIS) to study the intrinsic properties of the devices and understand the factors that define the long-term cycling stability, which

is further described through the use of equivalent circuit models. The main reasoning behind decomposition processes in ECDs and ways to suppress them are discussed.

3.2 Introduction

Electrochromic materials (ECMs) attract the close attention of researchers due to their applications in "smart" windows,[38, 39] antiglare mirrors[40] and other "smart" electrochromic devices (ECDs) such as charge-indicators for batteries[41] and in wearable technologies.[42-44] This is a result of the colour-changing phenomena that occur from redox reactions when a potential is applied. Several parameters must be met for an ECM to be a viable candidate for commercial applications, these include high contrast ratios, coloration efficiency, cyclic durability and short switching times.[10] Currently, ECMs are designed[45] using metal oxide films,[46-48] organic molecules,[44, 49] organic conjugated conductive polymers,[50] and metal-coordination complexes.[51, 52] Among the others, ECDs based on polypyridine metal-coordination complexes demonstrate enhanced cyclic stability, short switching times and exceptional coloration efficiency. Previously, it was demonstrated that the 2,2′:6′,2″-terpyridine (terpy) moiety can form stable complexes with a variety of metals in different oxidation states.[53, 54] This moiety as a part of different ligands can be used to covalently anchor and grow electrochromic (EC) molecular wires on a flat surface[55, 56] or to form EC coatings or separate nanosheets of metallo-supramolecular polymers.[27, 57, 58] Our group has developed ECDs that utilize just a monolayer of EC terpy-based metal complexes deposited on enhanced surface area conductive supports[34] to form the working electrode. Generally, ECDs are designed using at least two electrodes separated by the organic electrolyte. Of the two electrodes, the working electrode (WE) is that which exhibits the electrochromic properties, while the counter electrode (CE) is used for charge-balancing purposes. The CE

is typically made of a transparent conductive material such as indium-doped tin oxide (ITO), fluorine-doped tin oxide (FTO), conductive organic polymers[57, 59] or organic polymer-nanostructural composites[60] and their combinations, which allows for visualization of the colour-to-colour transitions. Sandwiched between these two electrodes, the electrolyte allows for the movement of ions between electrodes during redox reactions, facilitating state transitions. Due to the necessity of these components in a functioning ECD, it is vital to assess and optimize their stability and performance. While the impact of the ligand,[18] metal,[19, 20] and the support[41] of the WE on the properties of ECDs have been previously investigated, the influence of the CE was not explored in detail.

During their use, ECDs are commonly operated under wide potential windows in order to maximize colour-switching speeds.[59] However, wide potential windows can create harsh conditions increasing the rate of degradation. For example, when developing their solid-state polymer electrochromic displays, Remmele et al. observed peaks in cyclic voltammograms (CVs) of their devices when operating at potentials beyond that of their desired EC redox switching.[61] At these wide potential ranges, the material began to degrade under continuous cycling, resulting in the development of new CV peaks unrelated to their material. However, they also observed that at narrow voltage windows, stability was greatly improved at the expense of slightly lower switching speeds. This indicates a need for fine-tuning procedures to determine optimal operating potentials to reach the full cycling ability of an ECD. Ultimately, operating in a narrower potential window could minimize the occurrence of side reactions that degrade the device performance.

In addition to operating voltages, substrates and electrode compatibility must be taken into consideration, as poorly-chosen materials can affect the overall stability of the device.

For instance, Grätzel et al. investigated the interfacial charge-transfer resistance at the CE for their dye-sensitized solar cells.[62] A comparison between a platinized FTO CE and a PEDOT-based CE resulted in the discovery that a major decrease in interfacial charge-transfer resistance occurs when using the polymer-based electrode, attributed to the greater surface area of the PEDOT film. This adjustment in the properties at the CE resulted in an increase in power conversion efficiency to 10.3%, indicating that a full understanding of device architecture is necessary for the rational design of electrochemical devices. Commonly, the focus on individual device components such as chromophore, electrolyte or substrate is emphasized, rather than the synergistic effects of combining components into a device for practical applications. Through the fundamental understanding of processes that occur for each component in an operational device, long-standing obstacles resulting in poor efficiencies may be overcome, allowing for the rational design of ECD architectures with improved properties.

Herein, we propose the determination of optimal operating potential windows through cyclic voltammetry to reduce the likelihood of degradation processes, which may cause a decrease in device operation lifetime. Electrochemical Impedance Spectroscopy (EIS) is then employed during long-term cycling protocols to diagnose the onset of degradation.[63] X-ray photoelectron spectroscopy (XPS) is used to determine the cause of degradation for a typical electrochromic device cycled at a wide potential window. Equivalent circuit models such as the Randles circuit and Transmission-line model are used to further probe and describe the changes occurring within each system. Comprehensive use of these techniques provides insight into degradation mechanisms and how components of the device architecture are affected during operation.

3.3 Results and Discussion

We have previously reported that ECDs based on a monolayer of Fe(II) complex of 4'-(4-pyridyl)-2,2':6',2"-terpyridine (4'T) (Figure 3.1A) covalently embedded onto a surface-enhanced screen-printed indium tin oxide (ITO-50) support in combination with a lithium gel-electrolyte and flat indium tin oxide coated glass (ITO-glass) as the CE (Figure 3.1C, configuration **1**), demonstrate high optical contrast, exceptionally high coloration efficiencies, fast electron transfer and good thermal and long term cycling stability.[18] Interestingly, when the resulting ECDs were subjected to long-term electrochemical cycling (100+ hrs of continuous cycling), overall device performance degradation was attributed mainly to the fouling of the ITO-glass CE as a result of gel electrolyte and ITO reductive decomposition.[34, 64] Notably, upon replacement of the abovementioned CE and electrolyte, almost full performance of the ECD could be repeatedly restored since the WE bearing the hybrid EC/ITO-50 coating was unaffected. Here we report on the rational tuning of device operational conditions and optimization of ECD architecture by modifying the nature of the CE to promote electrochemical stability.

The role of the CE is particularly important due to the lack of a non-polarizable reference electrode in the 2-electrode device. This lack of a true reference electrode means that only the cell potential is controlled and not the potential at the WE. Thus, if the potential at the CE is unstable and drifts over time, so too does the potentials at the WE. However, the CE can serve as a pseudo-reference in a 2-electrode configuration so long as it can efficiently compensate the WE charge with minimal potential drift. For example, in proton exchange membrane fuel cells, the hydrogen oxidation reaction occurs on high surface area Pt

nanoparticles at the anode, which enables it to serve as both a counter and non-polarizable reference electrode for *in-situ* diagnostic of the cathode (i.e. the WE).[65, 66]

In a typical ECD device, the CE compensates (counters) the potential of the WE primarily by double layer formation, through a Faradaic process, or a combination of both capacitance and Faradaic processes. ITO is one of the most popular transparent conductive electrodes due to its optical transparency and high conductivity. However, it is a poor charge-storage material and thus a non-ideal counter-electrode[30] from an electrochemical point of view. We expect that by enhancing the CE through the increased surface area, electrode potentials will be more stable even in the absence of a reference electrode. As a result, we predict that combining voltage window optimization and modifications at the CE will allow for a more efficient design of ECMs.

To understand the role of the CE in solid-state ECD performance, we investigated the stability of the Fe 4'T WE in 3 different counter-electrode configurations (Figure 3.1C). All 3 configurations of ECDs use the Fe 4'T molecular unit (shown in black in Figure 3.1A) covalently embedded through the siloxane-based templating linker (marked in blue in Figure 3.1A) onto a thick (~7 μm) screen-printed ITO-50 support as the WE. Configuration **1**, which was previously used by us for ECDs[18, 34, 41] and should be considered as a starting point, involves the use of flat ITO-glass as a CE. Configuration **2** investigates the CE that consists of an ITO-glass functionalized with a screen-printed ITO-50 layer as used for the WE, without the Fe 4'T EC molecule on the surface. Configuration **3** employs a symmetric device electrode configuration, where both electrodes (WE and CE) are functionalized in the same way by screen-printed high surface area ITO-50 layer with a monolayer of the Fe 4'T covalently embedded onto the support.

Each CE material was characterized using CV in a 3-electrode cell configuration. From the CVs (Figure 3.1B), ITO glass is shown to be the least capacitive material as the flat ITO coating results in minimal porosity/surface area for electrical double layer formation. In contrast, an electrode functionalized with the screen-printed ITO-50 layer demonstrates a significant increase in capacitance due to the high surface area of the nanosupport and therefore an enhanced number of sites participating in the electrical double layer (EDL) formation. Lastly, the Fe 4'T substrate has the greatest double-layer capacitance, and also shows a fast redox process at $E_{1/2}$=0.85V vs Fc/Fc^{+} attributed to the surface-confined $Fe^{2+/}Fe^{3+}$ transitions. 3-electrode cell measurements were also performed on the Fe 4'T complex in solution (Figure 3.1B inset), for the purposes of comparing the Fe 4'T redox potential in solution versus covalently linked to the substrate.

CV measurements in a 2-electrode cell configuration were performed to determine the optimal potential window for operating each device configuration. To improve ECD stability, the optimal potential window should be the smallest range at which the redox potential is included to allow for the colour-changing process to occur while also minimizing possible side reactions. This was done by measuring CVs of the solid-state devices at a wide potential range (-1 V to +3 V) followed by increasing the lower-limit potential by small 100 mV steps and measuring the CVs each time, vice-versa with the upper-limit potential.

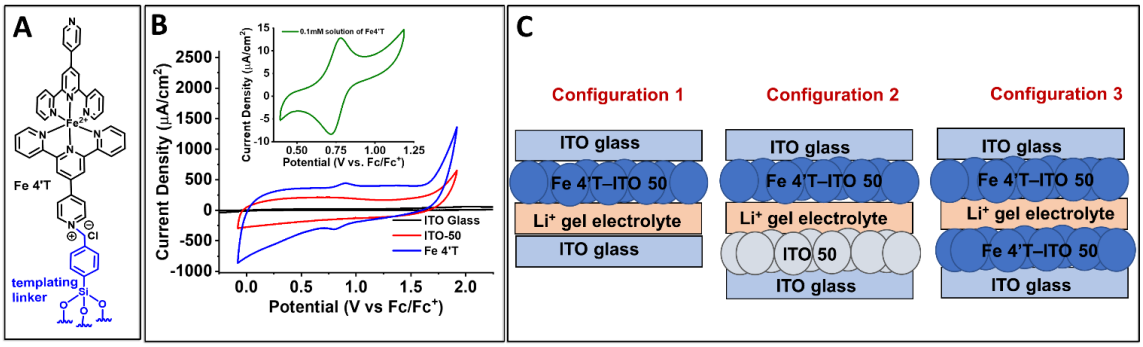

Figure 3.1. A) Structure of the Fe 4'T complex (black) and the linkage (blue) to the substrates **B)** 3-electrode cell CV measurements of the investigated ECMs, 50 mV s^{-1} scan rate; **Inset)** CV of a 0.1 mM solution of Fe 4'T in 0.1M TBAHFP/Acetonitrile electrolyte. **C)** Diagrams of the device configurations

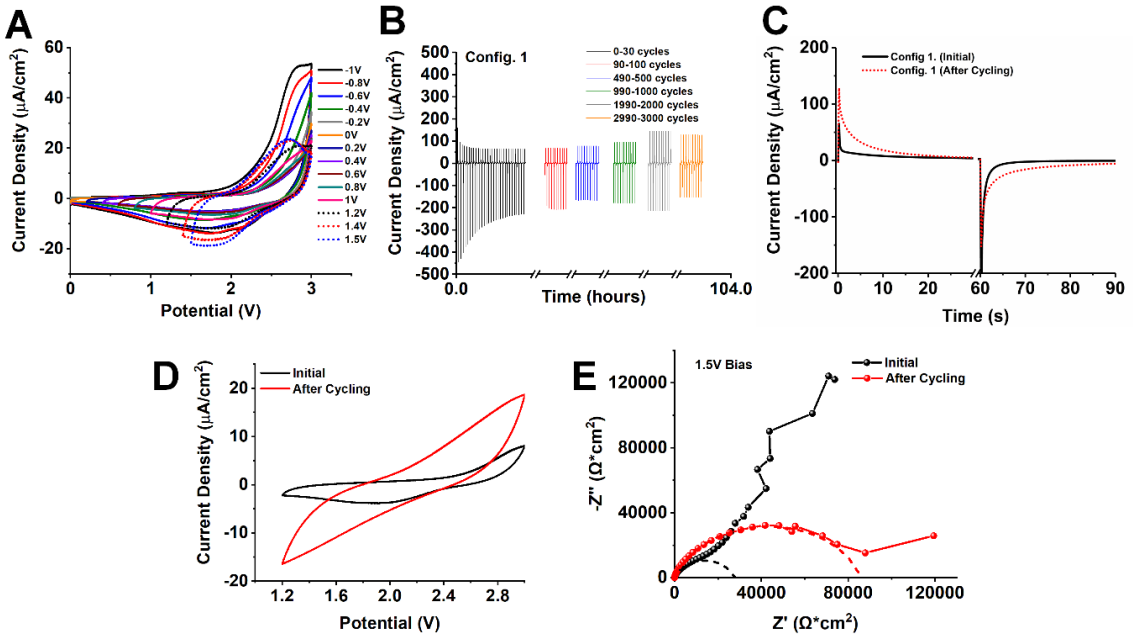

Figure 3.2. 2-electrode electrochemical measurements of config. **1 A)** CV measurements at varying lower potential limits for potential window determination **B)** Current density profile over 3000 cycles, where the device is held at +1.2V for 60s, then +3V for 60s (1 cycle) **C)** Current density profile of one full cycle before and after cycling **D)** CVs of device before and after 3000 hold cycles. **E)** Nyquist plot at a 1.5V bias where the dashed-lines indicate a semi-circle fit to visually compare R_{ct}

In Configuration 1, the Fe^{2+}/Fe^{3+} redox peak becomes better defined once the lower potential limit (LPL) is increased up to ca. 1.2 V (Figure 3.2A). Under these conditions, the electrochemical color switching is still readily observed (SI Figure 3.2). In addition, there is a significant decrease in the oxidative current (at higher potentials) when increasing the LPL. It is likely that at more negative potentials, degradation is occurring at the ITO CE[64]. The products of those degradation processes are then oxidized at higher potentials, which likely explains the increase in current observed in the 2.5 V to 3 V region. In this configuration, we are unable to lower the upper potential limit (UPL) as potentials lower than 3 V are not sufficient to support complete Fe^{2+}/Fe^{3+} oxidation, while potentials greater than 3 V result in the electrolyte-related side reactions.[34, 45] It is important to note that configuration **1** (config. **1**) demonstrates a significant drift of the redox peak potential in comparison to the potential seen for Fe 4'T in the 3-electrode cell (Figure 3.1B). To study long-term performance, the ECD in config. **1** was cycled for a total of 3000 cycles, equivalent to 100 h of square-wave cycles. The process was monitored by EIS and CV to follow and understand the nature of any degradation processes that may occur affecting the overall lifetime of the device. Device switching stability for config. **1** at the wide potential window of -1V to +3V and the modified potential window of +1.2V to +3V are compared in SI Figures 3.3-3.4, where it is evident that the modified potential window allows for stable-current profiles even at very fast switching speeds. In addition, it is evident that the greatest change in optical density (ΔOD) for config. **1** occurs when the potential is stepped at 60s holds (SI Figure 3.3). As a result, 60s potential holds were used when cycling all three configurations.

EIS can be used as a diagnostic tool to detect the presence of degradation processes occurring when operated in an EC device configuration. All EIS measurements were performed at DC bias potentials where redox processes are not expected to occur. If that holds true, the impedance response of the system should be accurately described by the transmission-line model (TLM), which is shown in Fig. 3.3A. The TLM is commonly used to describe the capacitive behaviour of porous electrodes with no redox processes, through parallel resistive rails (R_{ionic} and $R_{electronic}$) representing ion/electron transport, connected by capacitors representing double-layer capacitance. For these systems, the characteristic Nyquist plot shows a short 45-degree Warburg region at mid-to-high frequencies, after which a vertical response typical of capacitive electrodes is observed. Notably absent for the TLM circuit is a charge transfer resistance (R_{ct}). The presence of an R_{ct} is readily detectable by the presence of a semi-circle feature in a Nyquist plot. Thus, the TLM model is only expected to describe an EIS response of a stable EC device at the selected bias potential.

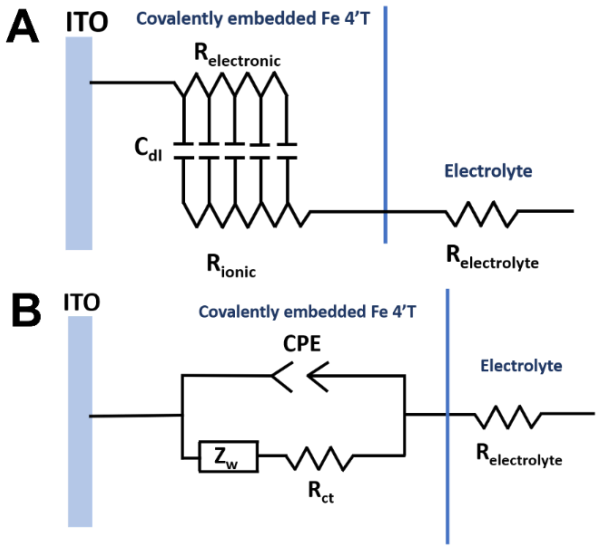

Figure 3.3. A) Transmission-line equivalent circuit model where C_{dl} represents double-layer capacitance **B)** Randles equivalent circuit model

When an R_{ct} is present, the impedance response can be described by a Randles-type equivalent circuit (Fig. 3.3B). In this circuit, a constant phase element (CPE) is in parallel with R_{ct} and a Warburg diffusion element (Z_w). The CPE is used to represent a non-ideal capacitor, while the Warburg element is a general component used to describe diffusion impedance, and can be defined further to identify behaviour at low-frequencies.

Given the different characteristic responses of these 2 circuits, EIS measurements should provide clear diagnostic information about the presence of degradation processes occurring within the ECD. Therefore, we performed periodic EIS measurements throughout the long-term device testing. Specifically, for each device configuration the DC bias employed was set to a cell potential where a faradaic process was not expected. Based on this, the TLM is expected to describe this situation. However, should degradation lead to cell polarization, a faradaic process will be present at that same cell potential, causing the EIS response to change drastically.

Figure 3.2E shows the initial and final EIS response for config. **1** when cycling between LPL=1.2 V and UPL=3 V with 60 s holds at each potential, for 3000 cycles. Prior to cycling, the Nyquist plot displays a small semi-circle arc, indicating a redox process with a measurable charge-transfer resistance being present. After 3000 cycles, the size and length of this arc increase greatly. This likely arises from degradation products that are being formed at the CE. It is important to understand that these measurements are performed at a DC bias potential of 1.5 V. We selected this bias potential since the initial CV experiments showed no redox processes present at this potential. Thus, we expect the ideal impedance response of the electrode to be dominated by the capacitive nature of the porous electrode structures and show no signs of a charge transfer resistance[34, 67]. However,

the presence of this charge transfer resistance indicates that some form of degradation has occurred that leads to an electron transfer process that is now present at this cell potential.

Due to the aforementioned charge-transfer resistance seen in the Nyquist plots for config. **1**, the Randles circuit is an appropriate model to use for this system. Through equivalent circuit simulation, we are able to effectively fit the mid-high frequency region of the Nyquist plots in order to extrapolate charge transfer resistance. By doing so, we determine that the initial charge-transfer resistance seen is approximately 24330 ± 819 $\Omega*cm^2$, which increases substantially to 50150 ± 1682 $\Omega*cm^2$ after 3000 cycles. Through these methods, we can gain both a qualitative and quantitative understanding of processes observed from EIS measurements. It is important to note that prior to cycling, while there is the presence of charge-transfer resistance, the system does trend towards a capacitive process at low frequencies, indicated by the vertical trend in impedance. This does not occur after 3000 cycles, indicating that the substantial charge-transfer resistance produced by degradation is a limiting process preventing diffusion, and ultimately preventing any capacitive behaviour. As a result, we can further simplify and better represent the system post-cycling by removing the Warburg component from the model.

This type of degradation can be further visualized in Figure 3.2D, where degradation is apparent by the tilt in CV shape, and the increase in oxidative and reductive currents are likely due to the formation of decomposition products. We can also observe the effect of degradation on switching capabilities as shown in Fig. 3.2B. Switching the cell potential should lead leads to a sharp increase/decrease in current that is followed by a quick return to baseline, correlating to the ability to fully reduce or oxidize the material. This behavior is observed early in testing, but the size of these peaks increase and broaden

over the course of operation. This is more clearly seen in Figure 3.2C which overlays the current transients measured at the initial part and final part of the test. These broad peaks indicate that some form of degradation has occurred and is inhibiting the performance of the device. In our previous work with structurally related EC layers grafted on screen-printed ITO-50 WE in the same device configuration, we observed that the main decomposition of the device occurs mainly due to degradation of electrolyte at the flat ITO glass CE. The spectroelectrochemical data for config. **1** at a wide potential window (SI Figure 3.3B) displays a decrease in optical density (ΔOD) during cycling, likely due to the same degradation that we observe here electrochemically.

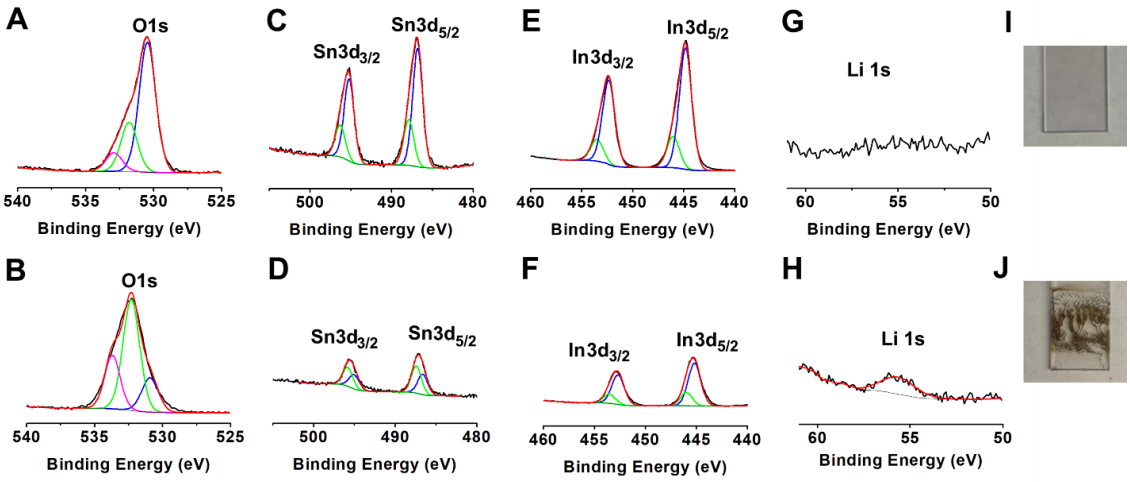

Figure 3.4. X-ray photoelectron spectra of CE assembled in config. **1** after wide potential window cycling from -1V to +3V: O1s **A)** fresh and **B)** after 3000 hold cycles; Sn3d region of **C)** fresh and **D)** after 3000 hold cycles; In3d region of **E)** fresh and **F)** after 3000 hold cycles; and Li1s region of **G)** fresh and **H)** after 3000 hold cycles **I)** ITO counter electrode before assembly and cycling **J)** ITO counter electrode after 3000 hold cycles and disassembly

To further understand this, we examined the surface composition of the ITO CE before and after device operation (-1V to 3V) in config. **1** using X-ray photoelectron spectroscopy (XPS) as shown in Fig 3.4. Deconvolution of the O1s peak for the fresh ITO CE demonstrates the presence of three species. The peak at 530.5 eV is typical for In_2O_3 and SnO_2 oxygen.[68, 69] The peak centred at 531.9 eV was previously assigned to oxygen atoms adjacent to oxygen defects. These oxygen atoms donate some of their electron density toward indium atoms that are no longer fully coordinated.[70] Finally, the peak centred at 533.0 eV can be assigned to oxygen in the hydroxide form.[71] After cycling, the overall shape of the oxygen peak changes. The peak at 532.2 eV becomes dominant. This peak may be attributed to a type of oxygen that bonds two Si atoms together (i.e. Si-O-Si)[72] and is typical for glass. This is in line with the fact that the Si 2p peak with a binding energy of 102.5 eV, which is characteristic to silicon oxide[73], becomes noticeable after cycling (SI Figure. 3.7A). The appearance of the Si 2p peak can be explained by the leaching of ITO. Indeed, after the cycling, the intensities of the Sn 3d and In 3d peaks diminish, moreover, the Li 1s peak at 55.8 eV (Fig 3.4H) becomes noticeable and is typical of LiF and LiBr.[74] The observed positions of the Sn and In peaks are in good accordance with earlier reports on ITO films.[70, 75] In 3d peaks of the fresh ITO and cycled ITO electrodes were deconvoluted to lower ($3d_{5/2}$ = 444.8 eV, $3d_{3/2}$ = 452.4 eV) and higher ($3d_{5/2}$=445.9 eV, $3d_{3/2}$=453.3eV) binding energies areas characteristic to In^{3+} oxide and surface-bound indium hydroxide, respectively.[75] The ratio between indium oxide and indium hydroxide moieties for the fresh ITO (1.0:0.26) remains almost the same (1.0:0.30) in the cycled ITO electrode. Similarly, Sn 3d peaks of the fresh ITO were fitted with two components corresponding to Sn^{4+} oxide ($3d_{5/2}$ = 486.8 eV, $3d_{3/2}$ = 495.3 eV) and surface-bound tin

hydroxide ($3d_{5/2}$ = 487.9 eV, $3d_{3/2}$ = 496.4 eV). Interestingly, the ratio of SnO_2-like and SnOH-like species at the fresh ITO sample is 1:0.4, while after the electrochemical cycling the relative ratio of the Sn^{4+} oxide decreases to become 0.7:1.0. The comparison of In:Sn:O ratios in the new ITO (9.1:1.0:17.8) with the ones of cycled ITO (4.8:1.0:90.5) suggests leaching of the ITO layer and growth of the oxygen peak coming from underlying glass substrate, both of which may increase device resistance.

Furthermore, the deposition of carbon on the electrode surface during electrochemical cycling was also observed. The presence of the C1s peak is typical for the as-received ITO.[76] However, while the C1s peak of the fresh electrode is centred at 285.5 eV, it shifts to lower binding energies with the centre at 284.8 eV after cycling (SI Figure 3.7B). This suggests that the carbon at the used electrode surface has a predominantly sp^2 graphitic nature.[77] Moreover, electrochemical cycling leads to the noticeable increase of the intensity of the C1s peak located at 289.0 eV, typical for carbonyl and carboxyl groups. The C1s spectrum does not contain any peaks in the 291-295 eV area, confirming there are no C-F bonds. The F 1s peak observed at 685.2 eV in the used sample (SI Figure 3.7C) is indicative for LiF[74], which is also consistent with the Li:F(1.3:1.1) stoichiometry. Finally, the cycled specimen demonstrates the presence of chlorine on the surface due to the Cl 2p peak located at 199.3 eV (SI Figure 3.7D) and has Li:Cl stoichiometry of 1.3:0.2.

In addition, it is apparent that ITO degradation is a major factor for the increased device resistance seen, based on the literature. The degradation of ITO in propylene carbonate solutions has been previously reported by Bressers et al[64], where they observed irreversible formation of metallic indium at highly anodic potentials. Alternatively, it was discovered that lithium-based electrolytes may degrade at high potentials, resulting in the formation

of lithium-rich surface films.[64] These degradation products can also be observed by visual assessment of the counter electrode after cycling from wide potential ranges, shown in Figure 3.4 I-J. The formation of surface films creates a dark brown "burned" appearance, similar to what is reported in the literature when ITO undergoes reductive decomposition.[32] In addition, our previous studies have clearly shown that degradation within config. **1** occurs is primarily due to the degradation of the ITO CE and Li-based gel electrolyte, while the electrochromic working electrode remains virtually unchanged. Through simple replacement of the burned ITO CE and electrolyte, we were able to effectively re-set operation of the ECD.[18, 41] Interestingly, Liu et al.[31] have previously shown that the electrochemical reduction of ITO in aqueous electrolyte systems under extreme polarization conditions significantly decreases the conductivity and transparency of the device. Authors attribute this to the formation of metallic In-Sn particles and open pores as a result of ITO dissolution from the CE. As the dissolution process progresses more metallic particles and open pores are formed that leads to significant decay in film conductivity due to non-homogeneity of the film. Since our system employs an organic electrolyte rather than aqueous, we do not observe the formation of metallic particles and open pores. However, the abovementioned XPS supports the idea that ITO leaching and electrolyte degradation products have deposited on the electrode surface, resulting in the observed device degradation. In the case of config. **1**, by tuning the potential window to a narrower range, we were effectively able to reduce the extent of degradation, however potential drift associated with the device architecture may still result in extreme negative or positive electrode potentials being reached, ultimately driving these degradation processes.

In order to address the stability issues seen with config. **1**, we have designed ECDs with CEs bearing the surface-enhanced ITO-50 layer without and with the EC molecular layer: configuration **2** and **3**, respectively. Potential window measurements for configurations **2** and **3** (Figure 3.5) display a different trend in comparison to configuration **1**. For config. **2**, the UPL and LPL could be readily adjusted to find the optimal potential window. It is evident that cycling this device to negative potentials is detrimental to the overall stability. Peaks corresponding to side-reactions (Figure 3.5A), simultaneously shift the Fe^{2+}/Fe^{3+} oxidation peak to higher potentials, resulting in higher energy input to drive the colour-changing reaction. Likely, these side-reactions are a result of the degradation products formed due to ITO reduction and electrolyte oxidation. Interestingly, a lower-limit potential of 1.2 V prevents the unwanted side-reactions from occurring, i.e. the drift to higher cell potentials is no longer observed. In this case, the Fe^{2+}/Fe^{3+} reaction now requires a lower cell voltage to drive the reaction. As a result, we selected 1.2 V as the optimal LPL for this device configuration. By maintaining the lower limit at 1.2 V, the UPL could then be tuned accordingly. As shown in Figure 3.5B, electrolyte decomposition is also observable at a cell potential of 2.5 V and higher, further contributing to the overall degradation of the device. However, this was circumvented by maintaining the UPL at voltages no higher than 2.5 V. At this UPL, the colour-changing redox reaction can still occur while preventing further decomposition processes that occur at increasingly negative and positive potentials.

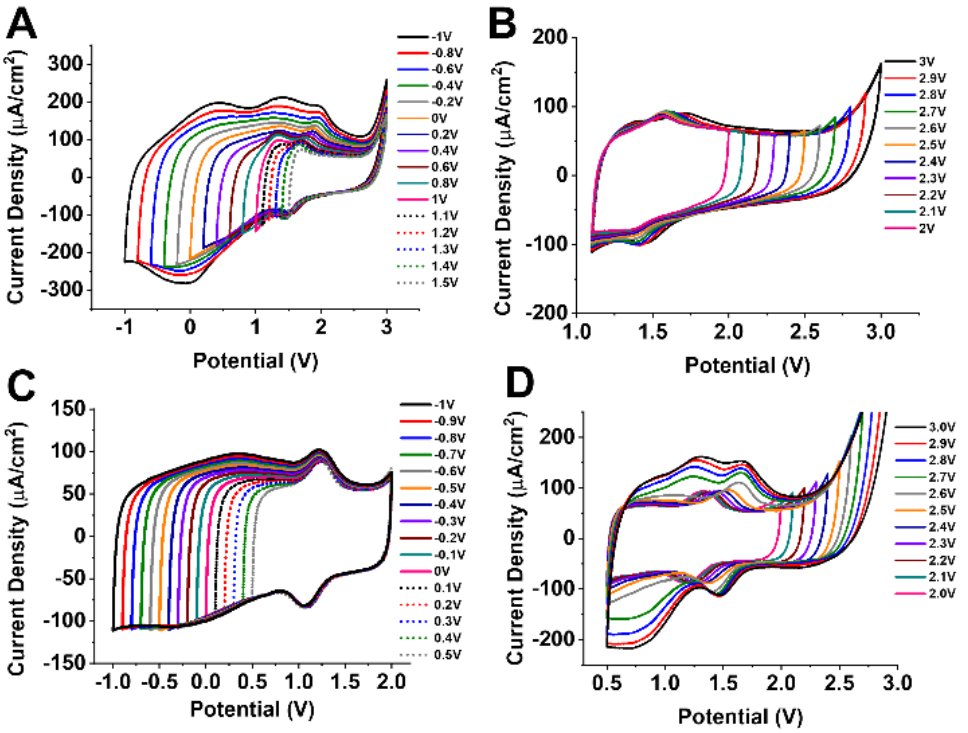

Figure 3.5. 2-electrode CV measurements of each configuration at varying lower and upper potential limits for potential window determination, obtained at 50 mV s^{-1} **A-B)** Config. **2**, **C-D)** Config. 3

This can be further visualized in Figure 3.6, where it is more apparent what the ideal UPL and LPL for the configuration should be, in order to prevent high potential shifts of the Faradaic process. After both the LPL and UPL were fine-tuned, the exclusion of the decomposition processes from the potential window allowed us to cycle ECD at config. **2** at a more negative LPL of 0.7V that lead to better colour transitions without affecting stability. Any adjustments to the potential window can be made as long as it is large enough to allow for full redox conversion, and narrow enough to prevent any unwanted side-reactions from occurring. As a result, the best optimized conditions for this configuration were set at the range of 0.7 to 2.0 V and this potential window was used for further long-term performance testing.

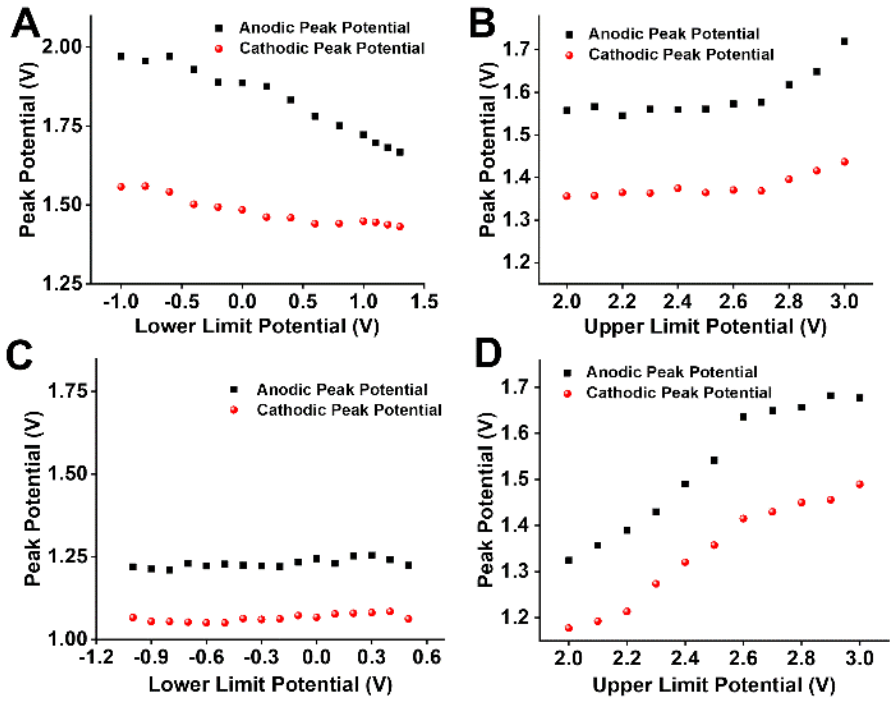

Figure 3.6. Dependence of the redox peak potential on upper and lower potential limits **A-B)** lower and upper limit potential dependence for Configuration **2**, **C-D)** lower and upper limit potential dependence for Configuration **3**.

The analysis of CVs of config. **3** (Figure 3.5C-D) shows similarities to that of the config. **2** with a few key features. The LPL of config. **3** (Figure 3.5C) has less impact on the Fe redox process. Although there is a capacitive increase at negative potentials, the redox potential does not shift to higher potentials and remains constant regardless of the lower limit potential, an opposite trend as what is seen when tuning the upper limit (Figure 3.5D). In this case, fixing the LPL at 0.5V while varying the UPL of config. **3**, the CV shows a significant variance in the redox peak potentials as the UPL increases. These variances can be seen specifically in Figure 3.6D. Along with peak potential shifts, there is also the presence of peaks associated with side-processes as well as high currents resulting from electrolyte decomposition.[34] In order to prevent degradation processes occurring when operating config. **3**, a potential window of 0.5 to 2.0 V was used for long-term measurements.

Interestingly, configurations **2** and **3** both display evidence of pseudo-reference behaviour of the counter-electrode, allowing for better *in situ* diagnostics of degradation mechanisms.[78] Reference electrodes have a stable electrode potential, which allows for the accurate measurement of the potential at the working electrode. However, the incorporation of separate reference electrode into the design of a solid-state ECD is problematic. This, in turn, results in a situation where there is potential drift in the 2-electrode device when compared with the 3-cell configuration that includes a reference. Thus, the potential drift at the CE in config. **1** causes an increase in unwanted side reactions leading to severe performance degradation. In contrast, the enhanced surface area of the CE employed in configurations **2** and **3**, makes these devices less polarizable and therefore the potential drift is less significant. This is likely a result of the electrode potentials being more stable with charging/discharging due to the properties of the CE materials themselves, as well as due to modification of the potential windows as the voltage difference between the working electrode and counter-electrode at any given moment is reduced with this technique.[79]

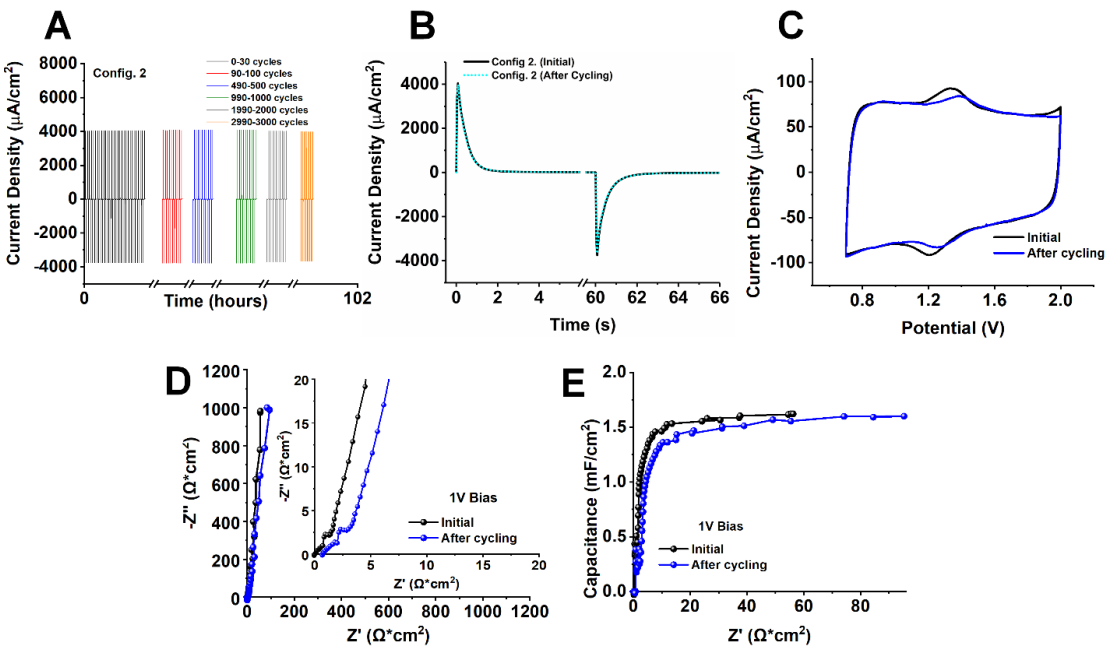

Figure 3.7. 2-electrode electrochemical measurements of config. 2 before, during and after cycling. The device was held at 0.7V for 60s then 2V for 60s (1 cycle) **A)** Current density profiles over 3000 hold cycles **B)** Current density profile of 1 full cycle before and after cycling **C)** CV after 3000 hold cycles, 50 mV s^{-1} scan rate. **D)** Nyquist plot **Inset)** Expansion of the mid-frequency region of the Nyquist plots **E)** Capacitance plot at a 1V bias.

Using the optimized potential windows, devices in all three configurations were subjected to long-term stability tests, which were monitored using both EIS and CV. Configurations **2** and **3** were cycled for a total of 3000 cycles, equivalent to 100 hr of square-wave cycling and results were compared to config. **1** as a reference. The latter was previously shown to perform 3000 cycles at non-optimal (-1 to 3V) conditions.[18] Using an optimized potential window, config. **1** can surpass 3000 cycles but displays significant degradation (Figure 3.2B, C). In contrast, much less degradation was observed for both configurations **2** and **3**. The current profiles for config. **2** and **3** (Fig. 3.7A and 3.8A) indicate extremely stable oxidative and reductive currents throughout cycling. This is in stark contrast to the performance in config. 1. Fig. 3.7B and 3.8B compare the current transients measured at the initial part and final part of the test for Configs. 2 and 3,

respectively. Prior to cycling, we observe that the current density returns to baseline very quickly after the initial increase/decrease for the modified configurations. However, unlike configuration **1**, configurations **2** and **3** have virtually identical i-t profiles even after 3000 cycles. This demonstrates a lack of degradation, which would otherwise hinder the ability for the materials to fully undergo their redox reactions. To further support this we compared the initial and final CVs of configurations **2** and **3** (Figure 3.7-3.8C). The CVs demonstrate much higher stability within the double-layer region, with only minor losses in the redox peak currents. In addition, for these configurations there are no signs of significant electrolyte oxidation or side-processes occurring during long-term cycling.

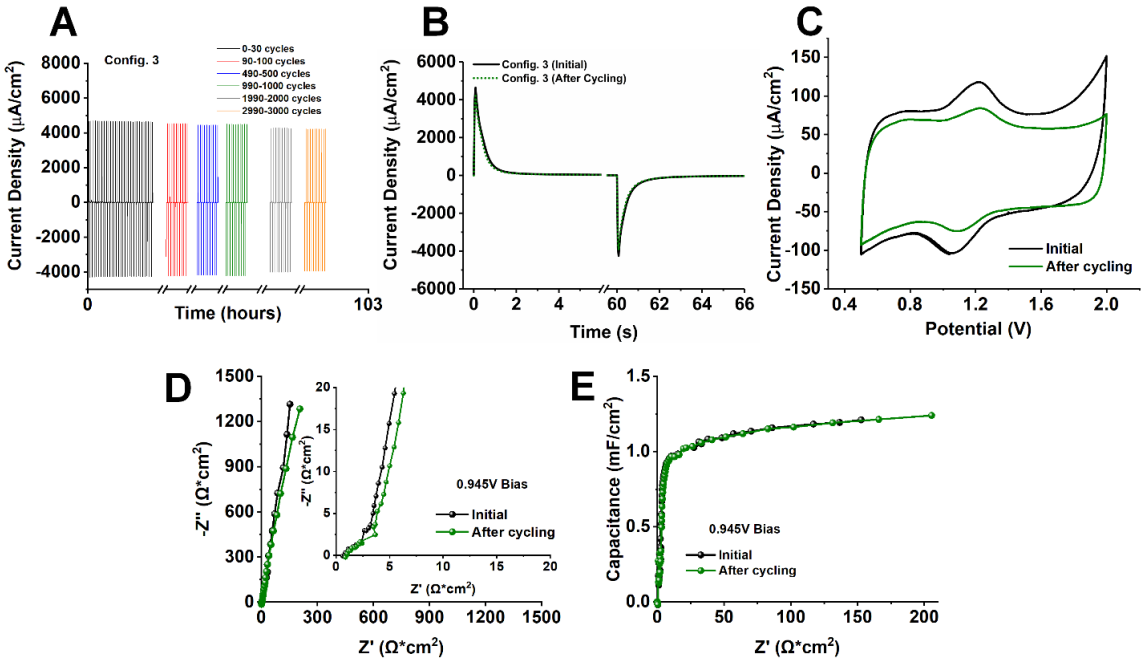

Figure 3.8. 2-electrode electrochemical measurements of config. **3** before, during and after cycling. The device was held at 0.5V for 60s then 2V for 60s (1 cycle) **A)** Current density profiles over 3000 hold cycles **B)** Current density profile of 1 full cycle before and after cycling **C)** CV after 3000 hold cycles, 50 mV s^{-1} scan rate. **D)** Nyquist plot **Inset)** Expansion of the mid-frequency region of the Nyquist plots **E)** Capacitance plot at 0.945V bias

The Nyquist plot measured in config. **2** (Figure 3.7D) does not have a semi-circle feature, rather a short 45-degree Warburg region in the high-to-mid frequency region, after which Z" increases sharply with decreasing frequency. This trend is also seen for config. **3** (Figure 3.8D). Thus, both configurations **2** and **3** demonstrate capacitive-like behaviour at low frequencies that is characteristic to finite space (aka open) Warburg diffusion. Open Warburg diffusion is a typical feature for porous electrodes without redox process, and is often analyzed in terms of a transmission-line model (Fig 3.3A).[80] As a result, the transmission-line model is appropriate to describe both config. **2** and **3** as they both demonstrate capacitive behaviour as expected within the potential region, and do not display any charge-transfer resistance. Rather, the main form of resistance in this model stems from the sum of ionic and electronic resistance, denoted by R_{Σ}. The values for R_{Σ} were determined and summarized in Table 1. Only minor increases in resistance after 3000 cycles were observed, further demonstrating the stability of these systems over config. **1**. As neither config. **2** or **3** undergoes the same degradation processes seen in config. **1**, this indicates that the systems do not stray from the proposed model.

The data can be also visualized as a capacitance plot (Figure 3.7-3.8E).[63] Prior to cycling, the capacitance plots for configurations **2** and **3** display a steep slope in the high-frequency region, indicating high conductivity and electron mobility, properties that are necessary for fast charge-storage mechanisms. The change in the low-frequency limiting capacitance (measured at 0.1 Hz) and total layer resistance (R_{Σ}) during the cycling are important indicators of material degradation[81-83], the values of which are summarized in Table 1. After 3000 cycles, config. **2** displays a slight decrease in the steepness of the capacitance slope and an insignificant decrease in limiting capacitance which is determined

at the lowest frequency point obtained, in this case at 0.1Hz. In comparison, config. **3** displays no change in conductivity or the mobility of electrons, and the limiting capacitance of the device remains almost unchanged. To further compare the configurations, values of R_Σ were determined and tabulated in Table 1. The values of R_Σ were obtained by the projection of the Warburg-length onto the x-axis to get $R_\Sigma/3$.[81] This can also be visualized in the inset plots of Fig 3.7-3.8D for configurations **2** and **3**, respectively. Config. **2** and **3** both display slight increases in the Warburg length after 3000 cycles. Overall, these devices displayed enhanced stability with minor fluctuations in resistance, likely a result of device to device assembly variability. Despite a larger initial R_Σ, config. **3** demonstrates a smaller increase in R_Σ compared to that of config. **2**. This ultimately indicates that the symmetric device architecture (config. **3**) is the most advantageous due to minor changes in conductivity, electron mobility and electrode resistance occurring even after extensive cycling. Although the optical properties of configurations **2** and **3** cannot be directly studied due to the associated colour and lack of transparency of these CEs, they greatly enhance the electrochemical stability of the ECD device. This enables more precise studies of novel WE electrode, enabling studies of their electrochemical stability through the use of additional diagnostic measurements. The CE used in Config. **2** has some potential for use in to be incorporated in one-sided stable ECDs since the porous modified CE offers partial transparency. As presented, config. **3** serves as the most promising device architecture to explore in the future development of ultra-durable dual-sided ECDs, that incorporate different electrochromic layers and offer a wide range of colour-changing transitions. It is important to note that the presence of other, slower degradation processes at the WE cannot be ruled out by these EIS measurements. However, by mitigating the degradation processes

at the CE and stabilizing its potential, one can more effectively probe WE stability through longer electrochemical measurements. As such, this methodology is expected to be highly useful for *in situ* stability monitoring of promising ECD materials over operational lifetimes that more closely resemble real-world deployment conditions.

Table 3.1. Summary of EIS parameters for all 3 configurations, before and after 3000 cycles

System	R_{ct} (Ω*cm^2)	R_{Σ} (Ω*cm^2)	C_{dl} (mF/cm^2)
Config. **1**[a]	24330 ± 819	N/A	N/A
Config. **2**[a]	N/A	5.72 ± 0.06	1.62
Config. **3**[a]	N/A	7.67 ± 0.38	1.21
Config. **1**[b]	50150 ± 1682	N/A	N/A
Config. **2**[b]	N/A	9.20 ± 0.1	1.59
Config. **3**[b]	N/A	8.83 ± 0.9	1.24

[a] Initial EIS parameters
[b] EIS parameters after 3000 cycles

3.4 Conclusions

This work contributes to the field of electrochromic devices and helps to solve long-standing problems in the area by rational design of the device architecture. It introduces the methodology for testing, comparison and improvement of electrochromic devices through CV and EIS experimentation that provides a better understanding of processes behind device operation. Here we propose different architectures of counter electrodes and fine-tune the cell potential windows for each electrochromic device configuration, as well as demonstrate the potential of EIS as an *in situ* diagnostic tool to monitor degradation within the device. Optimization of the potential window allows us to minimize the occurrence of side-reactions while ensuring a complete colour-changing redox process to occur. This, in turn, allows us to effectively prevent decomposition processes and therefore

significantly increase device lifetime. Through the use of XPS, we are able to detect the method of degradation that occurs with a typical electrochromic device architecture (config. **1**) coupled with wide potential window cycling. From this, we discovered that ITO leeching as well as carbon and LiF/LiCl deposition at the CE due to electrolyte degradation is the cause for device instability. As a result, we demonstrate that the most efficient devices incorporate high-surface-area counter electrodes with an extended number of electric double layer sites, as opposed to the standard ITO-coated glass electrode. These electrodes could be further functionalized with Fe 4'T complex, which due to Fe^{2+}/Fe^{3+} Faradaic processes result in higher-capacitive properties. The high-surface area counter electrodes allow for better probing of the 2-electrode solid-state device, without significant potential drift, which is commonly observed in these systems. Additionally, the incorporation of porous counter-electrodes allows the use of the transmission-line model to describe device behaviour. When operating in optimal potential windows, devices employing bare high-surface-area counter electrodes fabricated by screen printing of ITO-50 nanoparticles on ITO/glass (configuration **2**) and ITO-50-based counter electrode functionalized with Fe 4'T complex (configuration **3**) were able to overcome 3000 cycles with exceptional stability and minimal decomposition. By comparing the EIS data for all 3 configurations, we demonstrated that configuration 1 develops a significant charge-transfer resistance during early-cycling, indicating that rapid degradation is occurring at the ITO CE/gel electrolyte interface and must be analyzed using a Randles circuit. However, charge transfer resistance is notably absent in configurations **2** and **3**, even after extended cycling. This enables analysis of the WE by the TLM model which showed minimal changes in total layer resistance and limiting capacitance in both configurations. Despite

providing less desirable optical properties, the modified device architecture of config. **2** and **3** allows for a drastic extension of the cycling lifetime as well as enables a new set of electroanalytical diagnostics to better investigate novel EC materials and the stability of ECDs for significantly longer periods of time. This work demonstrates that future development of long-lasting ECDs will require the development counter-electrode materials that provide both ideal optical properties such as transparency, as well as pseudo reference capabilities that allow for a stable potential to be maintained during cycling. Advances in electrolytes and separators that prevent color-bleed between CE and WE and enhance contrast could also enable the use of electrochemically stable CE materials with less than ideal optical properties. This could potentially allow for the study of slower degradation processes occurring in the ECD that have been masked by the much more rapid degradation process at ITO CE/gel electrolyte interface.

3.5 Experimental Section

Solvents were purchased from VWR, ACP and Thermo Fisher Scientific. Chemicals were purchased from Millipore, Sigma and Alfa Aesar and were used without any further purification. Indium tin oxide glass slides (ITO glass) 15 × 25 × 1.1 mm, R_s = 5-15 Ω/sq were purchased from Delta Technologies. The slides were pre-treated using a solution of basic piranha for the removal of organic residues, without removing the ITO coating prior to the screen-printing process. A 1:5:1 solution of NH_4OH:H_2O:H_2O_2 water was used. The solution was heated to 60° prior to the addition of peroxide. After removal from heat, substrates were immersed in the solution for 15 minutes, washed 3 times with water, 3 times with isopropanol and dried with a stream of N_2. The slides were then stored in an oven at 110 °C. Any reactions that required an inert atmosphere were performed in the

MBraun glovebox with less than 2ppm of H_2O and O_2 using glassware that was dried overnight in an oven at 130 °C and cooled down in the antechamber of the glovebox prior to usage.

X-ray photoelectron spectroscopy (XPS) analysis was performed using a Thermo Fisher Scientific K-Alpha equipped with a monochromated Al Kα X-ray source. Scanning electron microscopy (SEM) images were obtained using a HitachiFlexSEM 1000. Roughness and profilometry measurements were performed using a Profilm3D Surface Profiler by Filmetrics (Filmetrics) equipped with 20× Nikon CF IC Epi Plan objective.

3.5.1 Preparation of screen-printed surfaces

Indium tin oxide nanoparticles (NPs) with a diameter of ≤ 50 nm (ITO-50) were purchased from MilliporeSigma. An ITO-50 NPs paste and screen-printed surfaces were prepared using a previously published synthetic procedure, where the specific surface area (SSA) of the ITO-50 NPs was reported as 30 ± 1 m^2/g (SI Figure. 3.6) and displayed a near reversible Type II (IUPAC classification) adsorption isotherm characteristic of adsorption on non-porous or microporous materials.[34] The ITO-50 NP paste was screen-printed onto ITO covered glass slides using a 90T 10 × 10 mm polyester mesh screen purchased from Mismatic. Each layer was left to relax in anhydrous ethanol for 30 s and heated over a hot plate at medium heat for 5 minutes. The process was repeated until a thickness of 7 μm was obtained. The slides were then annealed in a Fisher Scientific programmable muffle furnace for 1 h at 500 °C, 1 h at 600 °C and then left to cool to room temperature. SEM and Optical 3D profilometry of the ITO-50 support is shown in SI Figure 3.8 Further physical characterization of the ITO-50 support can be found in our previously published work. [19]

3.5.2 Screen-printed surfaces functionalization by Fe (II) 4'-(4-pyridyl)-2,2':6',2"-terpyridine

Fe (II) 4'-(4-pyridyl)-2,2':6',2"-terpyridine (Fe 4'T) complex (shown in black in Figure 3.1A) was synthesized according to a previously published literature procedure.[33] First, ITO-50 screen printed substrate functionalization by the templating layer (shown in blue in Figure 3.1A) was performed under N_2 atmosphere **in** an MBraun LABstar Pro Glovebox. For this, the substrates were submerged in a solution of dry hexane and trichloro(4-(chloromethyl)phenyl) silane (100:1 v/v) for 20 minutes and rinsed 3 x 15 mL with dry hexanes followed by 3 x 15 mL with dry acetonitrile. Then, the covalent attachment of Fe 4'T to the surface-anchored templating layer was performed. Substrates bearing the templating layer were transferred to borosilicate glass pressure tubes and a 0.4 mM solution of Fe 4'T in anhydrous acetonitrile was added. Pressure tubes were sealed and heated at 95 °C for 96 h in the absence of light, after which they were brought to room temperature and rinsed 3x with acetonitrile, 3x with hexanes, sonicating for 5 min, once per solvent.

3.5.3 Lithium gel electrolyte synthesis

A lithium gel electrolyte was synthesized for use in the 2-electrode ECD, based on a procedure by van der Boom.[37] Briefly, 700 mg of poly (methylmethacrylate) (PMMA), 300 mg of lithium trifluoromethane sulfonate salt, 8.9 mL of anhydrous acetonitrile and 1.7 mL of propylene carbonate were combined in an oven-dried glass vessel, under N_2 atmosphere with vigorous stirring.

3.5.4 Electrochemical Characterization

All electrochemical measurements were performed using a Solartron Analytical 1470E multi-channel potentiostat paired with a Solartron 1260 Frequency analyzer. Cyclic

Voltammetry (CV) was performed in both a 3-electrode and 2-electrode cell configuration. In the 3-electrode cell, CVs were measured from 0 to 2.0V at a 50 mV s^{-1} sweep rate. 3-electrode cell CV measurements of the substrates were performed using a Bio Logic plate-evaluating cell. A platinum wire was used as the counter-electrode (CE), $Ag/AgNO_3$ (0.01M) as the reference electrode and the screen-printed surfaces functionalized by Fe (II) 4'T as the working electrode (WE). The electrolyte used was a 0.1M solution of tetrabutylammonium hexafluorophosphate (NBu_4PF_6 aka TBAHFP) in acetonitrile. The reference electrode was calibrated using a standard solution of ferrocene (Fc) in the same electrolyte. For 3-electrode measurements, the potentials have been corrected to the Fc/Fc^+ scale.

Solid-state, 2-electrode measurements were performed using a WE that was the screen-printed ITO-50 surface functionalized by Fe (II) 4'T, and one of the investigated substrates as the CE. The device was assembled by coating the surface of the WE with ca. 0.1 mL of Li^+ gel electrolyte[37] and brought together with the active portion of the counter-electrode. The electrodes were held together using transparent tape. Electrochemical Impedance Spectroscopy (EIS) was performed over a frequency range of 80,000 Hz to 0.1Hz with an AC signal amplitude of 5 mV. EIS measurements were performed at DC biases below that where redox potentials are observed in the initial assembly of the device (1.5V, 1V and 0.945V for configurations 1, 2, and 3, respectively). For these systems, the initial uncompensated (electrolyte) resistance ranged from 220-270 Ω cm^2. The uncompensated resistance has been subtracted from the EIS plots for configurations 2 and 3 in order to compare changes in electrode impedances.

Long-term measurements were obtained through the application of 60 s square-wave potential holds at the determined lower and upper potential limits (abbreviated as LPL and UPL, respectively), resulting in 1 full cycle. Device health was monitored using periodic CV measurements within the same potential window as well as EIS measurements.

3.5.5 Spectroelectrochemical Characterization

UV-Visible diffuse reflectance spectra were obtained using a PerkinElmer 750S UV-vis spectrophotometer with a 60mm integrating sphere. UV-Vis spectra were recorded using the Lambda 750s Scanning Quant software. Using the Timedrive software, colour-switching stability was determined by setting the wavelength to the Fe 4'T metal to ligand charge transfer wavelength of 600 nm and holding the potential at -1V and +3V for variable amounts of time. Short-term stability was determined at a wavelength of 600 nm by holding the potential at -1V for 60s, followed by +3V for 60s and alternating for a total of 10 hours.

3.6 Acknowledgements

Financial support was provided by the National Sciences and Engineering Research Council of Canada through the Discovery Grants program (NSERC, RGPIN-2020-003652, RGPIN-2016-05823) as well as Ontario Tech University**.** The authors thank Dr. Peter M. Brodersen, Ontario Centre for the Characterisation of Advanced Materials (OCCAM) at the University of Toronto (Toronto, ON, Canada) for performing XPS measurements.

3.7 Supplementary Information

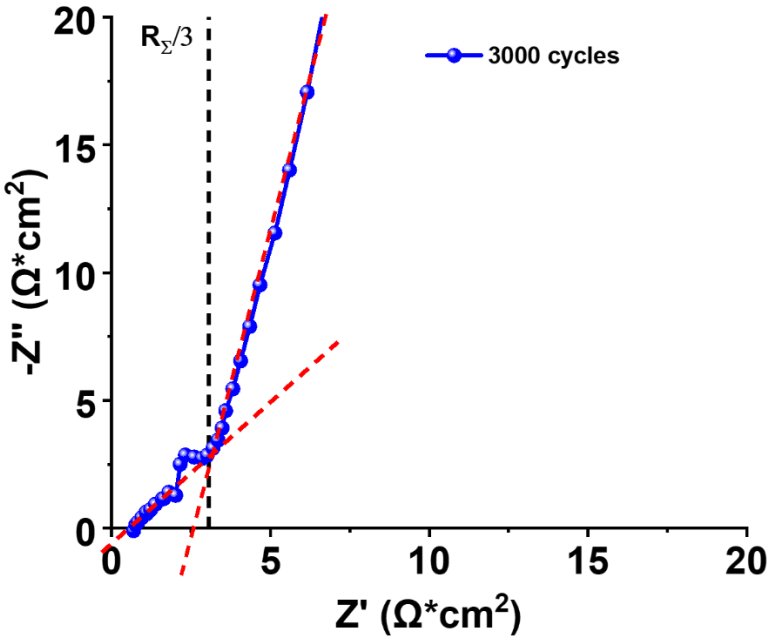

SI Figure 3.1. Example of R_Σ determined for configuration **2** after cycling, through intersection of linear high and low frequency regions in the Nyquist plot.

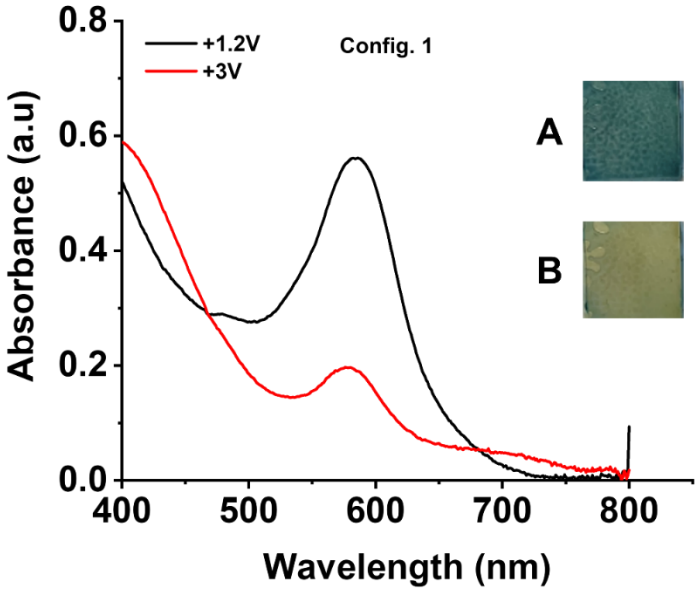

SI Figure 3.2. UV-Visible Diffuse Reflectance Spectrum of config. **1** in the coloured **(A)** and bleached **(B)** states using the modified potential window of +1.2V to +3V

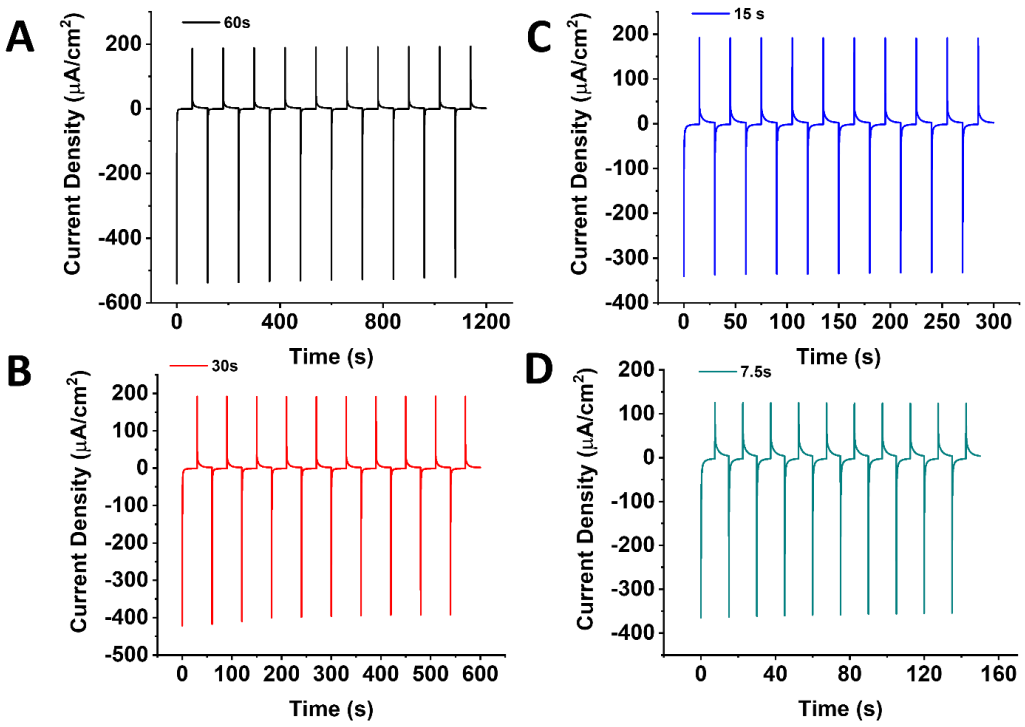

SI Figure 3.3. Current profiles for config. 1 when switching between the modified potential window of +1.2V to +3V with A) 60s holds B) 30s holds C) 15s holds and D) 7.5s holds

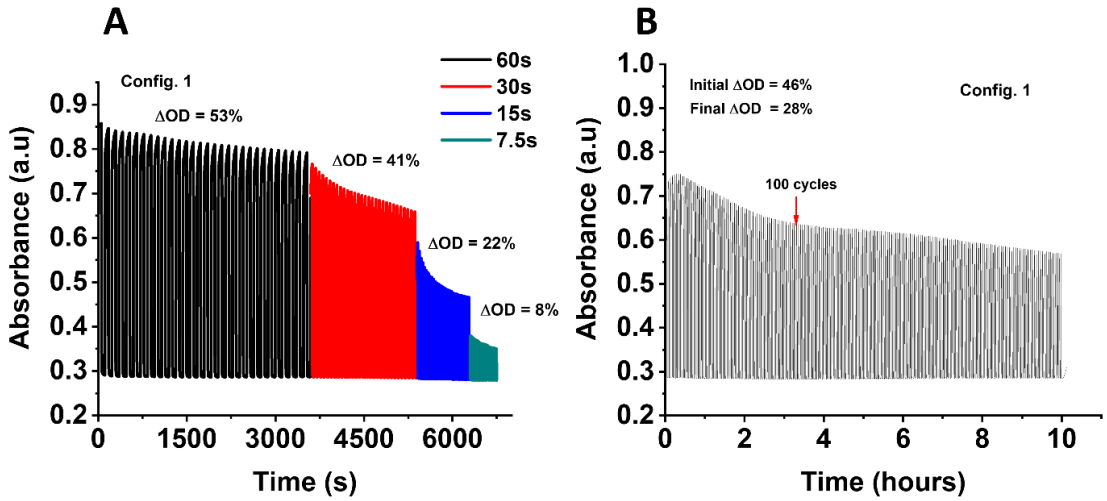

SI Figure 3.4. Spectroelectrochemical performance and stability of config. **1** at a wide-potential window of -1V to +3V **A)** Change in optical density (ΔOD) at varying potential hold times **B)** Potential holds of 60s over 10 hours of cycling

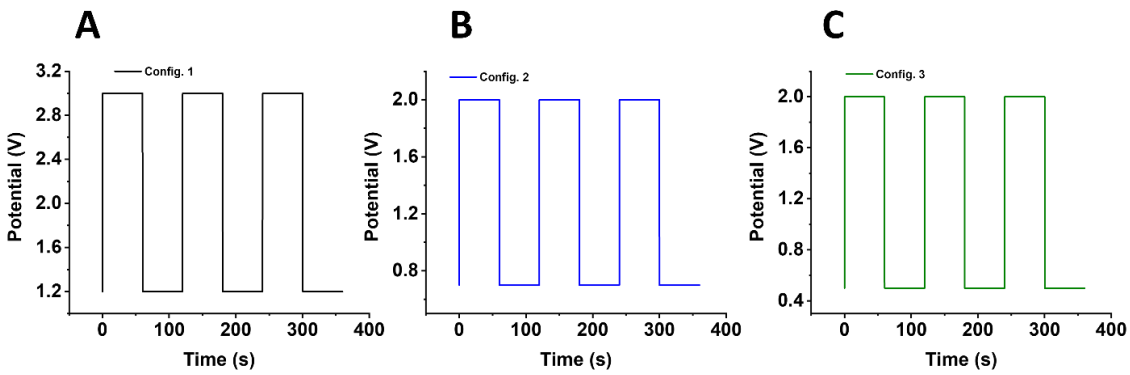

SI Figure 3.5. Square-wave profiles for **A)** Config. 1 **B)** Config. 2 and **C)** Config. 3

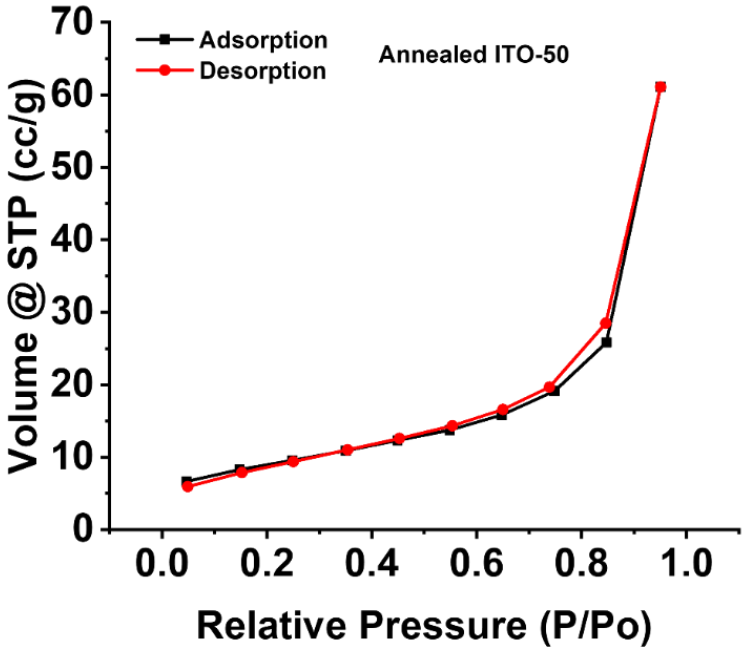

SI Figure 3.6. BET analysis of the annealed ITO-50 nanoparticles with a BET Specific Surface Area of 30 ± 1 m^2/g

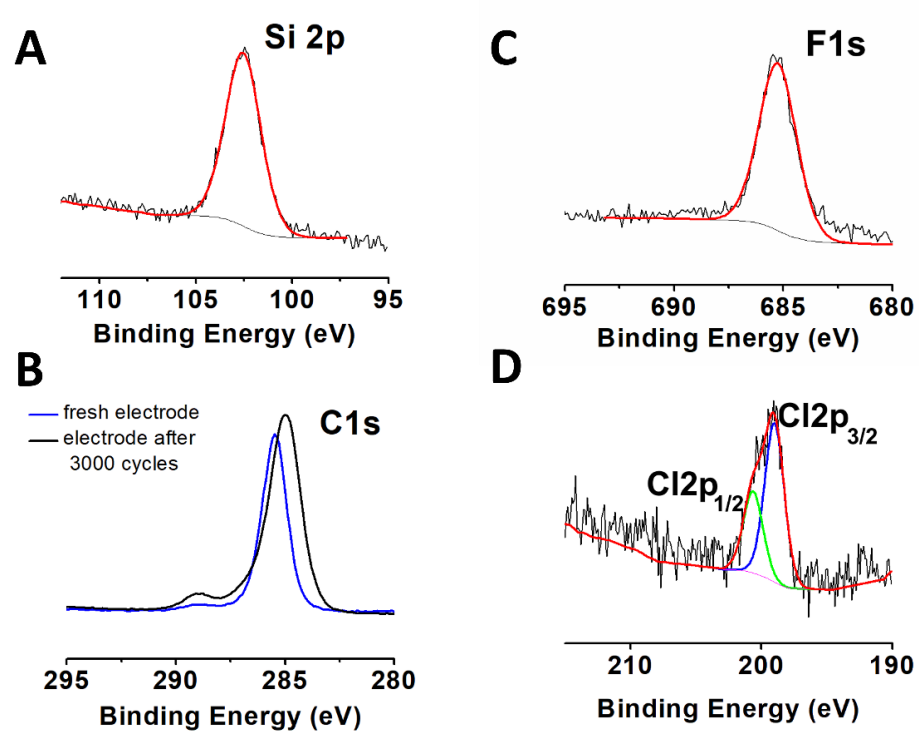

SI Figure 3.7. X-ray photoelectron spectra of CE assembled in config. 1 after wide-potential window cycling from -1V to +3V **A)** Appearance of Si 2p peak for the CE assembled in config. 1 after 3000 hold cycles **C)** C1s area of the fresh ITO electrode (blue) and ITO electrode after 3000 cycles (black) **C)** F1s region of the ITO electrode after 3000 cycles **D)** Cl2p region of the ITO electrode after 3000 cycles

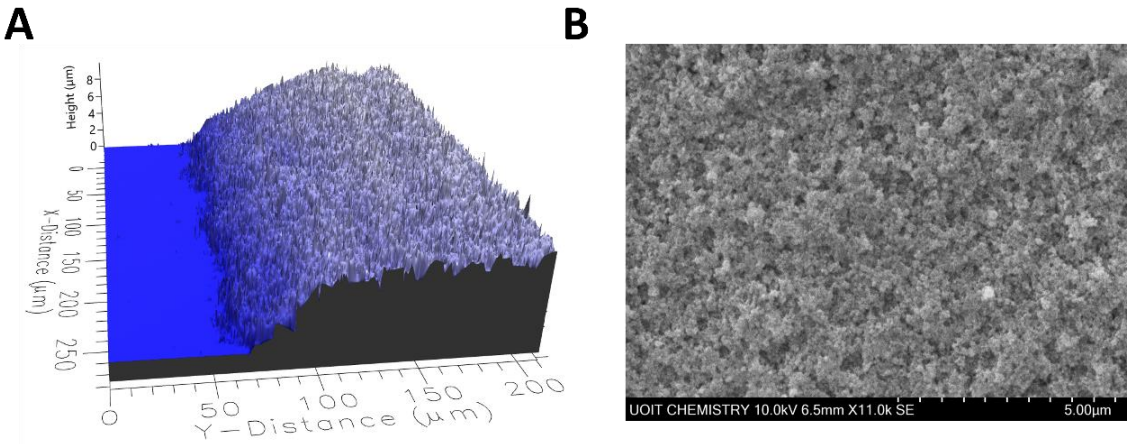

SI Figure 3.8. A) Optical profile of the ITO-50 support **B)** Scanning electron microscope (SEM) image of the ITO-50 support

Chapter 4. Surface-Enhanced Counter Electrode Materials for the Fabrication of Ultradurable Electrochromic Devices

4.0 Preface

Reprinted with permission from Ahmad, R; DiPalo, V.; Bell, M.; Ebralidze, I.I.; Zenkina, O.V.; Easton, E.B., Surface-Enhanced Counter Electrode Materials for the Fabrication of Ultradurable Electrochromic Devices. *ACS Applied Energy Materials* **2022**. Doi: https://doi.org/10.1021/acsaem.1c03480.

4.1 Abstract

Electrochromic devices (ECDs) and especially electrochromic supercapacitors, where the real-time state of charge is indicated by the color, have a wide range of applications. However, to meet modern challenges, these devices should demonstrate exceptional charge-discharge durability. In this work, we demonstrate that electrochemical cycling stability of ECDs based on a monolayer of 4'-(4-pyridyl)-2,2':6',2"-terpyridine-iron(II) complex that was covalently linked to the working electrode (WE), can be drastically enhanced by a proper design of the counter electrode (CE). Enhancing the surface area of the flat indium tin oxide (ITO) CE by a layer of screen-printed ITO nanoparticles results in an ECD that upon continuous spectroelectrochemical switching for 600 cycles demonstrates negligible deterioration of the change in optical density. The enhanced surface area of the CE significantly diminishes the electrode and gel electrolyte degradation, and allows us to gain fundamental insight into the pathway of degradation of the electrochromic molecules at the WE. During prolonged cycling (20,000 cycles and

50,000 cycles), the overall total resistance of ECDs remains fairly unchanged, while the capacitance decreases due to a loss of the pseudocapacitive component associated with electrochromic molecules. X-ray photoelectron spectroscopy (XPS) suggests that this loss is likely due to the cleavage of the linkage C-N^+ bond followed by the dissolution of the entire metal complex molecule into the electrolyte

4.2 Introduction

In modern literature, we see a dramatic growth of interest in the development of effective energy-efficient electrochromic devices (ECDs). This fundamental research has immediate applications in a wide variety of fields such as “smart" windows, anti-glare glass, signage, wearable technology, as well as for energy storage applications.[25, 84, 85] Consequently, this has resulted in significant improvements in the performance and stability of the electrochromic materials (ECMs) based on organic molecules[86], conjugated conductive polymers[49, 87, 88], metal oxides[89] and metal-coordination complexes.[20, 37, 90] Novel hybrid ECMs are developed and systematically optimized[91] to obtain desired optical properties such as: high optical density and coloration efficiency, fast bleaching and coloration speeds, and optical durability. In addition, there has been stemmed interest into the improvement of electrolytes used for solid-state ECDs in order to maximize the ionic conductivity and long-term stability.[92-94]

While the target of the majority of published works is the immediate improvement of one component of the ECD, (often EC material, electrolyte, or ion storage layer), literature examples that focus on the comprehensive analysis and optimization of the entire ECD cell to ensure its best synergetic performance and durability, remain rare. The inherent

challenge with the development of practical solid-state ECDs is improving their cyclic stability.[95, 96] It is commonly seen that ECDs of various types are unable to operate for extended periods of time without suffering from degradation, ultimately resulting in a decay of the optical response and longer switching times. This can be attributed to the basic architecture of an ECD, which normally consists of 1) an ECM, 2) an electrolyte layer and 3) transparent conductive electrodes. A common drawback in the design of these devices is the inability to predict all possible interactions between the above-mentioned components and the compatibility of operating potentials within the ECD.

Previously, we have shown that the nature of the counter electrode (CE) and applied operating potentials have a significant impact on the stability of ECDs fabricated using an electrochromic working electrode (Fe 4'T ECM) based on a monolayer of 4'-(4-pyridyl)-2,2':6',2"-terpyridine-iron(II) complex, covalently embedded onto high surface area screen printed layer of indium tin oxide nanoparticles (ITO-50 NPs). Specifically, we have shown that the use of flat indium tin oxide (ITO)/ glass as a CE, despite its popularity, is inadequate for ECD design due to its poor charge-storage properties leading to CE polarization and increased rates of cell degradation due to CE and electrolyte decomposition pathways.[97] In more detail, we have demonstrated that ECDs that employ flat ITO/glass CE and ECMs based on monolayers of structurally related metal complexes covalently embedded onto surface-enhanced conductive supports (ITO or fluorine-doped tin oxide (FTO) screen-printed films) as working electrodes (WE), show significant degradation of the CE after 3,000 cycles (100 hrs).[41] However, after 3,000 cycles the WE can be re-used, confirming high stability of the Fe 4'T ECM. Re-assembly of the ECD by combining the used WE with a new flat CE and fresh gel electrolyte effectively resets the performance of the device,

allowing it to operate for another 3,000 cycles or more. In this case, ECD degradation is mainly due to Li electrolyte decomposition that results in the precipitation of Li salts on the CE surfaces and leaching of the ITO layer, which in turn leads to detrimental conductivity and performance decreases.[97] Notably, ECDs comprised with a surface-enhanced CE demonstrate very minor decomposition since the increase in surface area expands the electrical double-layer and thus capacitance, promoting increased charge storage[25] while preventing cell polarization and degradation. The method of incorporating ion-storage layers into ECD architecture has become increasingly popular, with storage layers developed using suitable metal oxide materials such as TiO_2 and NiO.[24, 25] These ion-storage layers prevent cell polarization by efficiently compensating for the charge at the WE. Despite these modifications aimed at improving device performance, the durability limits of the resulting ECDs were rarely defined. Typically, ECD cycling is halted at the first sign of degradation, rather than continuing operation until system failure; as a result, the lifetime and degradation pathways of many systems remain unknown.

Herein, we provide an in–depth investigation of the performance and decomposition pathways of the most promising architectures of ECDs based on Fe 4'T ECM for much longer periods of 20,000 and 50,000 cycles; corresponding to 28 and 69 days of non-stop cycling, respectively. We compared ultra-long-term performance of our two most robust ECD architectures: ***non-symmetric*** that employs the surface-enhanced ITO NPs support as the CE (Fe 4'T/ITO NPs), and ***symmetric*** that comprises two identical electrochromic films used as a WE and CE of the cell (Fe 4'T Symmetric), Figure 4.1. The cycling lifetimes of these devices are determined through a full suite of electrochemical techniques such as cyclic voltammetry (CV), electrochemical impedance spectroscopy (EIS) and

galvanostatic charge-discharge (GCD) cycling as well as comprehensive XPS analysis of CE and WE electrodes before and after testing. Lastly, we explore the optical properties of the Fe 4'T/ITO NPs system to determine whether the charge-storage properties of the CE influence electrochromic properties such as coloration efficiency, switching speeds and optical durability.

4.3 Experimental

Solvents used were purchased from VWR, Thermo Fisher Scientific and ACP. Chemicals were purchased from Millipore Sigma or Alfa Aesar and used without any further purification. ITO glass slides were purchased from Delta Technologies and pre-treated with a solution of basic piranha to remove surface organic contaminants. The pre-treatment of the slides was done through the use of a 1:5:1 solution of NH_4OH:H_2O:H_2O_2. The solution was heated to 60°C prior to the addition of peroxide. After removal from heat, peroxide was added to the solution and substrates were immersed for 15 minutes. After 15 minutes, substrates were rinsed 3 times with deionized water, 3 times with isopropanol, and then stored in an oven at 110°C.

4.3.1 Preparation of ITO nanoparticle substrate

Using a previously published synthetic procedure,[34] an ITO nanoparticle (NP) paste was prepared and screen-printed onto the previously mentioned pre-treated ITO glass slides. The ITO-50 paste was prepared using ITO NPs with a diameter of ≤ 50 nm, purchased from Millipore Sigma.

4.3.2 Surface functionalization of ITO NP substrate with Iron (II) 4'-(4-pyridyl)-2,2':6',2"-terpyridine (Fe 4'T)

Iron (II) 4'-(4-pyridyl)-2,2':6',2"-terpyridine complex (Fe 4'T) was synthesized according to a published procedure.[18, 33] In brief, 4'-(4-pyridyl)-2,2':6',2"-terpyridine and iron (II) tetrafluoroborate hexahydrate were dissolved in a minimal amount of acetonitrile and mixed in a 2:1 molar ratio. Upon mixing, a dark purple color is immediately observed. After brief stirring, the solvent was evaporated under vacuum.

Functionalization of the previously mentioned ITO NP substrate was performed using an MBraun LABstar Pro Glovebox with a nitrogenous atmosphere. Within the glovebox, ITO NP substrates were placed in a solution of anhydrous hexane and trichloro(4-(chloromethyl)phenyl) silane (100:1 v/v) for 20 minutes, rinsed 3 times with 15 mL aliquots of anhydrous hexane then rinsed 3 times with 15 mL aliquots of dry acetonitrile to prepare the silane-templated ITO NP substrate. The templated substrates were then transferred to borosilicate pressure tubes and a 0.4 mM solution of Fe 4'T complex in anhydrous acetonitrile was added. Pressure tubes were then sealed and heated at 95°C for 96 hours in darkness. After heating, pressure tubes were cooled to room temperature and the substrates were rinsed 3 times with acetonitrile and 3 times with hexanes, sonicating for 5 minutes in each solvent.

4.3.3 Synthesis of lithium gel electrolyte

A lithium gel electrolyte was synthesized for use with the solid-state devices, based on a procedure previously published by van der Boom.[37] This was done by combining 700 mg of poly (methylmethacrylate) (PMMA), 300 mg of lithium trifluoro methanesulfonate

salt, 8.9 mL of anhydrous acetonitrile and 1.7 mL of propylene carbonate. Synthesis was performed using oven-dried glass under a nitrogen atmosphere, with vigorous stirring.

4.3.4 Electrochromic device assembly

To assemble the solid-state electrochromic device, the working and counter electrodes were sealed together using the gel electrolyte, where the conductive and active portions of the electrodes face each other. For each device, ~ 0.1 mL of the lithium electrolyte was used, and the electrodes were held together using transparent tape. ECDs were left for 24 hours prior to use to allow for electrolyte penetration into the porous substrates.

4.3.5 Electrochemical characterization

All electrochemical measurements were performed in a 2-electrode solid-state configuration, where only a working and counter electrode are present. All measurements were performed using a Solartron Analytical 1470E multi-channel potentiostat, coupled with a Solartron 1260 frequency analyzer. Long-term durability cycles are defined as: 1 cycle = 60 s potential hold at 0V, followed by a 60 s potential hold at 2 V.

Cyclic Voltammograms were obtained from 0 V to 2 V for both device configurations, at a sweep rate of 50 mV/s. These measurements were performed periodically during long-term durability cycling.

Electrochemical Impedance Spectroscopy was performed from a frequency range of 80,000 to 0.1 Hz, at DC biases characteristic of double-layer and pseudocapacitive regions, determined from CV.

Galvanostatic Charge-discharge curves were obtained at a variety of current densities for both systems. Capacitance retention, determined from GCD cycling, was obtained using a current density of 0.06 mA/cm^2.

4.3.6 Spectroelectrochemical characterization

Chronoabsorptometry measurements were performed using a Solartron Analytical 1470E potentiostat in combination with a PerkinElmber Lambda 750S UV-Vis Spectrophotometer operating in diffuse-reflectance mode.

UV-vis spectra were obtained by holding the ECD at a reductive potential of 0 V and oxidative potential of 2 V while simultaneously measuring the spectra from 320 to 800 nm. Switching speeds and long-term chronoabsorptometry measurements were performed by fixing the wavelength to λ_{MLCT} and recording absorbance as a function of time. ECDs were cycled by applying 0 V and 2 V to the WE with 60 s, 30 s, 15 s, 7.5 s, 3.25 s, 1.5 s and 1 s holds. Spectroelectrochemical cycling was performed at 30 s holds for 10 hours to reach 600 cycles The Fe 4'T/ITO NPs ECD was stored for 3 months at ambient conditions then cycled for an additional 6000 cycles, for a total of 6600 spectroelectrochemical switching cycles. Spectroelectrochemical data of Fe 4'T/ITO NPs ECD after 20,000 cycles is displayed in the supplementary information (SI Figure 4.3, 4.4)

4.4 Results and Discussion

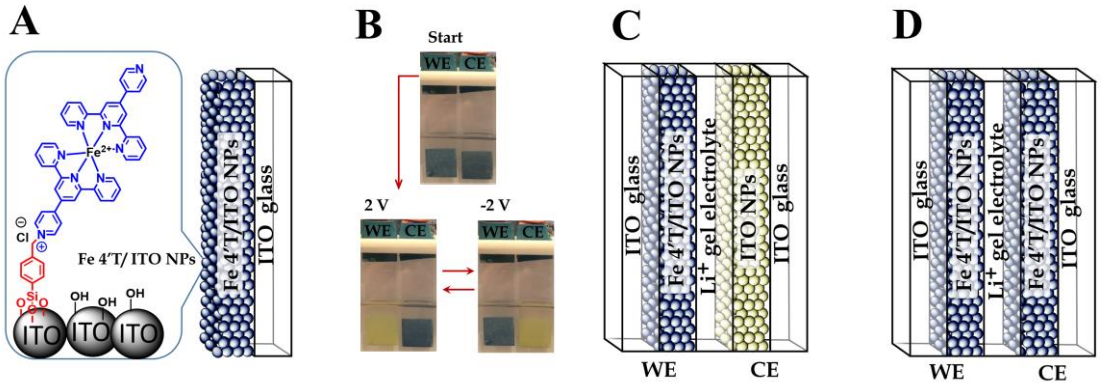

Figure 4.1. A) Structure of the Fe 4'T/ITO NPs ECM producing monolayer deposition of complex onto the high surface area ITO NPs substrate. The structure of Fe (II) 4'-(4-pyridyl)-2,2':6',2"-terpyridine (4'T) complex is highlighted in blue. **B)** Photographs of Fe 4'T/ITO NPs ECM used as both WE and CE in 2-electrode cell filled with 0.1M TBAHFP/Acetonitrile electrolyte show the possibility of sequentially change the colors of WE and CE by application of different voltages. The color difference (CD) when comparing the colored and bleached electrodes recorded through the liquid electrolyte is 53%. **C)** Solid-state ECD configuration Fe 4'T/ITO NPs ECD that utilizes Fe 4'T/ITO NPs ECM as WE and surface-enhanced ITO NPs material as CE. **D)** Solid-state ECD configuration: Fe 4'T Symmetric ECD that utilizes Fe 4'T/ITO NPs ECM as WE and CE.

A monolayer deposition of Fe (II) 4'-(4-pyridyl)-2,2':6',2"-terpyridine (4'T) complex onto enhanced surface area ITO screen-printed supports (Figure 4.1A) results in the Fe 4'T/ITO NPs ECM. When assembled into a 2-electrode cell using this ECM as both the working and counter electrodes (WE and CE), the color of the electrodes can be changed by alternating the applied voltage (Figure 4.1B).

We have previously reported that this ECM can be assembled as a WE into a solid state device using a lithium gel electrolyte and flat ITO glass as a CE, however, this architecture is not beneficial to the cycling durability of the ECDs, and rather contributes to early-onset degradation.[97] In contrast, the use of surface-enhanced counter electrodes

with improved charge-storage properties prevent counter-electrode and electrolyte degradation, resulting in a significant improvement to the cycling stability of the ECDs.

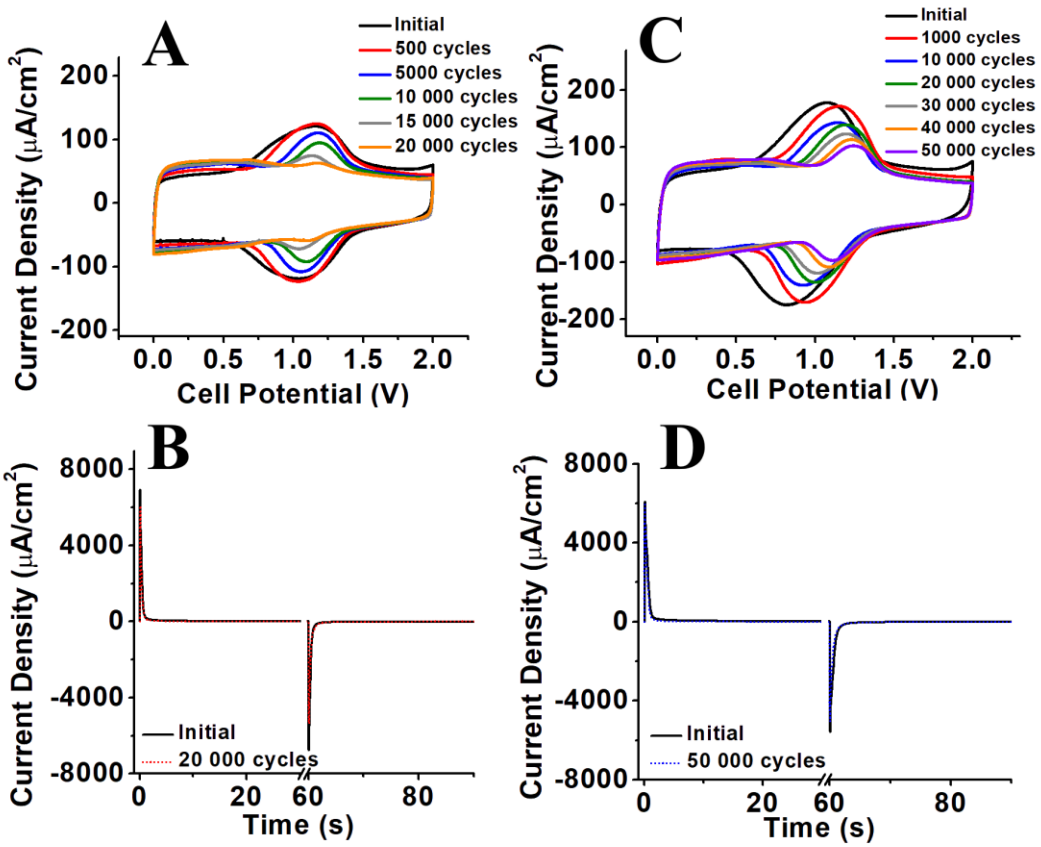

Figure 4.2. Electrochemical durability of ECDs after long-term cycling where 1 cycle consist of 0 V potential hold for 60s following by 2 V potential hold for 60s. **A)** CVs of Fe 4'T/ITO NPs ECD over 20,000 hold cycles (28 days). **B)** Current profiles of Fe 4'T/ITO NPs ECD before and after 20,000 hold cycles (28 days) **C)** CVs of Fe 4'T Symmetric ECD over 50,000 hold cycles (69 days). **D)** Current profiles of Fe 4'T Symmetric before and after 50,000 hold cycles (69 days).

Additionally, degradation was shown to be prevented by narrowing the potential window to exclude polarizing potentials that may degrade device components. Hence, by preventing counter-electrode and electrolyte degradation, other pathways for degradation may be observed, such as ECM degradation. In this study, we report on the ultra-durable

ECD capabilities obtained by employing these high surface area counter electrodes, through electrochemical and optical means.

We have assembled two types of solid state devices: 1) Fe 4'T/ITO NPs, where we employ the Fe 4'T/ITO NPs ECM as the WE and surface-enhanced screen printed ITO NPs support at the CE (Figure 4.1C), and 2) Fe 4'T Symmetric ECD (Figure 4.1D) that contains two identical Fe 4'T/ITO NPs ECMs working as WE and EC. Previously,[97] the stability of these ECDs were analyzed by the means of CV and EIS, demonstrating minimal degradation of the devices up to 3,000 cycles.

Both device configurations were cycled at their optimal potential windows of 0 V to 2 V, using the method of 60 s potentiostatic holds at each potential to define 1 cycle (120 s total). For the Fe 4'T/ITO NPs device configuration, we observe a well-defined CV (Figure 4.2A), which undergoes changes over 20,000 cycles, equivalent to 28 days of operation. Specifically, the CV indicates a decrease in redox-peak current as cycling continues, likely due to dissolution of the metal complex into the electrolyte as the linkage bond (N-quaternization of the outer pyridine ring in the molecular layer) is broken. The onset of this degradation can be seen to occur at approximately 5,000 cycles, which increases with further cycling. In this work, we have diminished the significance of the electrolyte and CE degradation pathways by incorporating high surface area CEs, and are now able to observe the ECM degradation occurring at a drastically slower rate and after the greater number of cycles. Despite this, the current transients shown in Figure 4.2B indicate that post-cycling, the time required for the ECD to switch between states is unchanged. Rather, there is a decrease in the overall current density of the system due to

the loss of electrochromic molecules from the surface of the WE, but the rate of redox transition for the remaining covalently-linked complex is unchanged.

A similar trend is seen for the Fe 4'T Symmetric ECD, although with a significant increase in overall performance. In particular, the symmetric configuration was able to undergo cycling for 50,000 cycles or the equivalent of 69 days of non-stop operation. In this case, the symmetric architecture boasts an increase in electrochemical stability over the Fe 4'T/ITO NPs ECD; even after 50,000 cycles the presence of the Fe^{2+}/Fe^{3+} redox peaks were distinctly observable in CVs. This is a clear indication of the slower rate of ECM degradation due to the symmetric architecture of the device. Since the WE and CE both employ a combination of double-layer and faradaic charge storage with identical magnitudes, the extent of polarization occurring is significantly decreased, further slowing down the rate of degradation for this system. Similar to the previous ECD, the time required for full redox transition is unchanged even after ultra-long durability cycling.

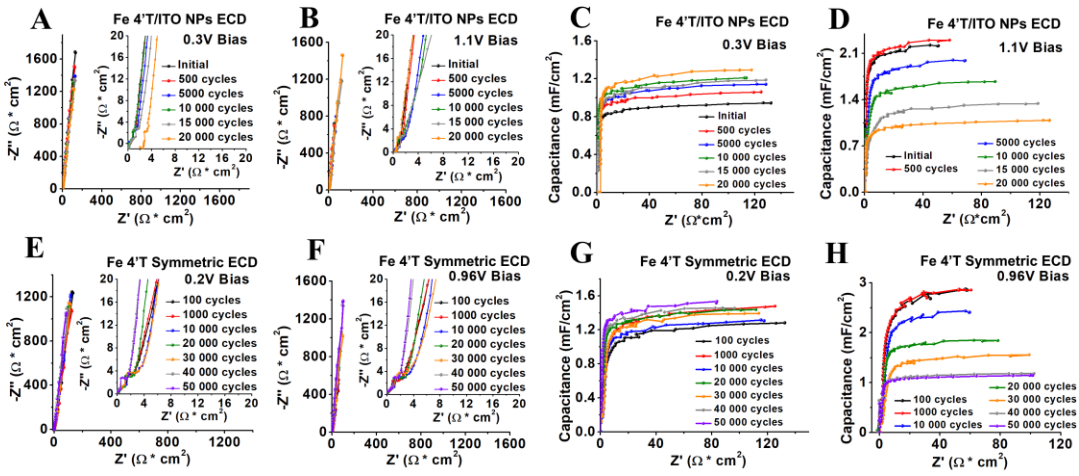

Figure 4.3. Electrochemical Impedance Spectroscopy (EIS) measurements at DC biases of the double-layer (0.3 V for Fe 4'T/ITO NPs ECD and 0.2 V for Fe 4'T Symmetric ECD) and faradaic regions (1.1 V for Fe 4'T/ITO NPs ECD and 0.96 V for Fe 4'T Symmetric ECD). **A-B)** Nyquist plots of Fe 4'T/ITO NPs ECD. **C-D)** Capacitance plots of Fe 4'T/ITO NPs ECD. **E-F)** Nyquist plots of Fe 4'T Symmetric ECD. **G-H)** Capacitance plots of Fe 4'T Symmetric ECD.

Electrochemical impedance spectroscopy (EIS) measurements allow for the detection and understanding of degradation within an electrochemical system. Here, we have performed EIS measurements at DC biases correlating to double-layer (0.2 – 0.3 V bias) and faradaic regions (0.96 – 1.1 V bias) as determined by CV. By incorporating surface-enhanced electrodes into the ECDs, we expect that the impedance response can be described using the transmission-line model, which is often used to describe the capacitive behaviour of porous electrodes. Features that support this model in a Nyquist plot include a short 45-degree Warburg region followed by a steep vertical response indicative of capacitive processes.[29, 63, 98] Indeed, EIS results (Figure 4.3) show that despite a loss of complex over cycling, the overall total resistance of both systems remains fairly unchanged as seen in the Nyquist plots. This indicates that the systems maintain excellent conductivity and electron mobility even after extensive cycling. The shape of the Nyquist plots at lower frequencies succeeding the Warburg region is typical for the finite space diffusion behavior. This response is normally associated with the diffusion of ions within a blocking boundary, such as in a porous storage electrode.

Furthermore, the capacitance plot of Fe 4'T/ITO NPs ECD at the double-layer region (0.3 V bias) remains stable albeit with a slight increase in overall capacitance (Figure 4.3C). As expected, the capacitance plot at the redox peak potential of this ECD (1.1 V bias) displays an overall decrease in capacitance due to a loss of the pseudocapacitive component (Figure 4.3D). Fe 4'T Symmetric ECD demonstrates similar behavior (Figure 4.3E-H), where it is evident that the total resistance of the system remains unchanged, and the major form of degradation seen should be attributed to the loss of the electrochromic

molecule (Fe 4'T metal complex) from the surface denoted by a decrease in faradaic capacitance.

Specifically, the Fe 4'T/ITO NPs ECD demonstrates a 51% decrease in total capacitance (after 20,000 cycles) while the Fe 4'T Symmetric ECD demonstrates a 60% decrease in total capacitance (after 50,000 cycles) due to loss of the pseudocapacitive component and redox activity shifting to more positive potentials .

To quantify the discoloration of the material upon cycling, the colors of electrodes were compared to the initial color of the high surface area ITO NPs electrode before functionalization with the metal complex (aka surface-enhanced ITO NPs material). A CIELAB colour space system was applied for the analysis of colours. CIELAB is based on the luminance, L*, and colour channels a^* and b^*. Luminance may change between 0 (black) and 100 (brightest level of white). Color channels at zero ($a^* = 0$ and $b^* = 0$) correspond to the grey colour state. Channel a^* may be varied from green (negative values of a^*) to red (positive values a^*), while channel b^* may change from yellow (positive values of b^*) to blue (negative values of b^*). The colour difference (CD) of electrodes were calculated using the following equation:

$$CD = \sqrt{(\Delta L^*)^2 + (\Delta a^*)^2 + (\Delta b^*)^2}$$

The pristine Fe 4'T/ITO NPs ECM before assembly into the device is featuring a *Regal Blue/Blue* colour/hue (Figure 4.4A insert) and demonstrates a significant CD of 72.5 if compared to the blank ITO NPs electrode (SI Table 4.1). After 20,000 electrochemical cycles in Fe 4'T/ITO NPs ECD configuration, the device was disassembled and the gel electrolyte was washed out. The color of the resulting Fe 4'T/ITO NPs WE significantly fainted to *Dingley/Green* (Figure 4.4B insert) and a much lower CD of 33.2 was observed.

Interestingly, during long-term cycling in this configuration, the color of blank ITO NPs CE changes from initial *Pavlova/Yellow* to become *Chalet Green*/*Green* with a substantial CD of 34.3 (Figure 4.4C).

When assembled into Fe 4'T Symmetric device configuration, the electrochromic material shows much less extent of the degradation. After 50,000 electrochemical cycles in Fe 4'T Symmetric configuration, when the same ECM was used as both WE and CE, the color of the WE has changed to *Chalet/Green* with CD of 37.7 (Figure 4.4D), while the color of the CE became *Goblin/Green* with a CD of 52.8 (Figure 4.4E). It is clear that ECM used as CE in symmetric device configuration demonstrated the best color retention.

Separate color analysis was performed for assembled devices, where the CD represented colour changes of the device between colored and bleached states of the WE. (SI Table 4.2). Thus fresh Fe 4'T/ITO NPs ECD features *Blue Whale/Blue* in the colored state and *Himalaya/Yellow* in the bleached state with CD of 43, while the same device after 20,000 cycles demonstrated only CD of 10.7 upon changing from *Green Smoke/Green* and *Gimblet/Green* colours for colored and bleached states, respectively.

Importantly, fresh Fe 4'T Symmetric ECD demonstrates *Deep Fir*/*Green* colour/hue in the colored state of the WE and *Saratoga/Green* in the WE bleached state (SI Figure 4.5 A, B) with CD' of 21.7. Note that lower CD' values for Fe 4'T Symmetric ECD in comparison to Fe 4'T/ITO NPs ECD is due to some colour bleed from electrochromic CE due to semitransparent nature of the device. After 20,000 cycles, the Fe 4'T Symmetric ECD featuring *Timber Green/Green* and *Tom Thumb /Green* for coloured and bleached states and CD' of 16.5. After 50,000 cycles, the Fe 4'T Symmetric ECD appears in *Timber Green/Green* and *Lunar Green/Green* for colored and bleached states, respectively (SI

Figure 4.5 C, D) with CD' of 15.7. Note that even with initially lower CD for this configuration, we see a better residual CD for the device after 50,000 that supports our electrochemical and EIS data for the long-term experiments.

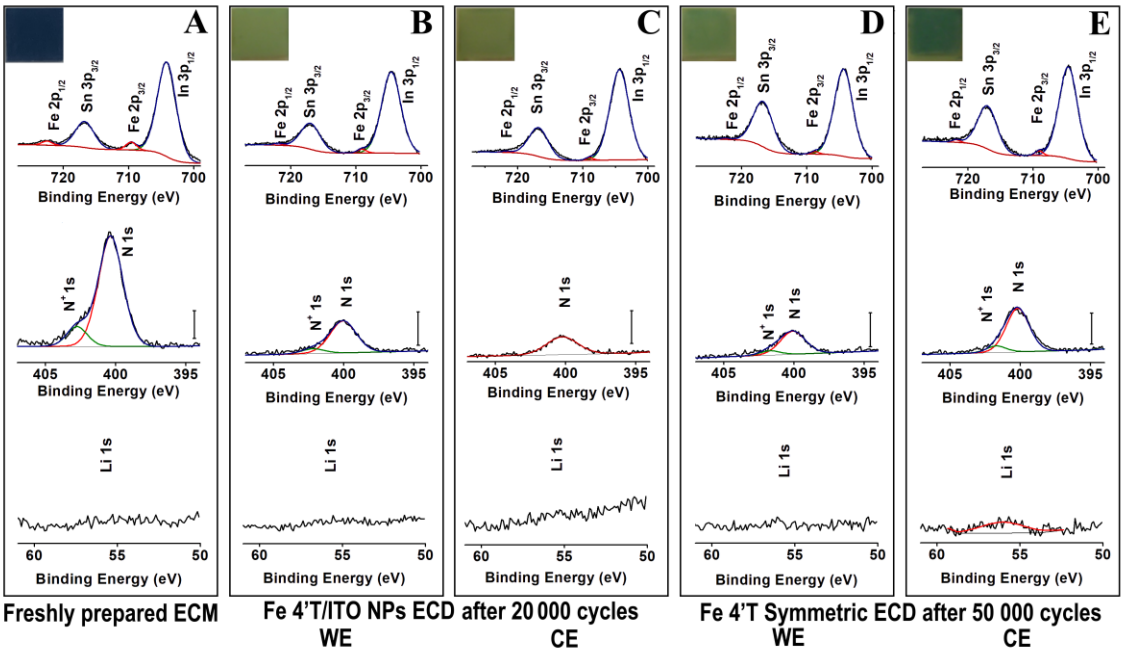

Figure 4.4. X-ray photoelectron spectra: characteristic binding energy areas of Fe 2p, N 1s, and Li 1s of **A)** ECM as prepared, **B)** ECM served as WE in Fe 4'T/ITO NPs ECD (non-symmetric solid-state ECD) after 20,000 cycles, **C)** non-functionalized ITO-50 support served as CE in Fe 4'T/ITO NPs ECD after 20,000 cycles, **D)** ECM served as WE in Fe 4'T Symmetric ECD after 50,000 cycles, and **E)** ECM served as CE in Fe 4'T Symmetric ECD after 50,000 cycles. Inserts show photographs of the corresponding electrodes. A scale bar in N1s spectra corresponds to 2,000 counts / s.

To get a better idea about Fe 4'T stability within the ECM, X-ray photoelectron spectroscopy (XPS) surface analysis was used. As prepared, the ECM clearly demonstrates an Fe $2p_{3/2}$ peak centered at 709.3 eV and Fe $2p_{1/2}$ peak at 722.2 eV (Figure 4.4 A). The analysis of the WE for the Fe 4'T/ITO NPs ECD after 20,000 cycles as well as the WE and CE for the Fe 4'T Symmetric ECD after 50,000 cycles shows a significant loss of intensity of the Fe 2p doublet. The loss of electrochemically addressable iron species is consistent with film discoloration (Figure 4.4 inserts) and decreases in redox-peak current upon

electrochemical cycling (Figure 4.2 A, C). Since strong In $3p_{1/2}$ and Sn $3p_{3/2}$ peaks coming from the ITO screen printed support interfere with the weak Fe 2p doublet, it is hard to precisely quantify the iron loss during cycling. Moreover, after cycling, traces of iron are detectable on the CE of the non-symmetric ECD, which initially was not functionalized with the Fe 4'T complex.

The N 1s spectra of the as-prepared ECM can be deconvoluted resulting in two peaks at 400.3 and 402.5 eV corresponding to nitrogen atoms in aromatic rings[99] (N) and quaternized aromatic nitrogen[100] (aka pyridinium nitrogen) atoms (N^+), respectively. The atomic ratio of $N:N^+$ is 6.8:1, close to the expected 7:1 stoichiometric ratio. Analyzing N 1s peak areas of the freshly-prepared ECM and ECMs served as electrodes in ECDs, we can estimate the nitrogen loss after the cycling. Thus, after 20,000 cycles, the WE in non-symmetric (Fe 4'T/ITO NPs) device retains 26% of nitrogen.

After 50,000 cycles, the WE and CE of Fe 4'T Symmetric ECD maintain 18% and 33% of nitrogen load, respectively. Notably, after 20,000 cycles, the CE of non-symmetric device demonstrates the presence of aromatic nitrogen atoms (the peak centered at 400.2 eV) on the surface, but no quaternized nitrogen atoms. This fact together with the presence of iron(II) ions on the CE of non-symmetric ECD after cycling suggests that Fe 4'T complex detaches from the WE surface, migrates through the electrolyte layer, and physisorbs onto the surface of CE. This can explain the color change of the material observed after the cycling (*vide supra*).

Applying the Wagner sensitivity factors[101] to the peak areas of the CE of Fe 4'T/ITO NPs ECD after 20,000 cycles gives an Fe:N atomic ratio of 1:7.7. This suggests that iron leaching from the WE is the result of $C\text{-}N^+$ bond cleavage and further dissociation of the

entire molecule of the complex from WE surface. This can further be demonstrated by integrating the area underneath the anodic and cathodic peaks of the cycling CVs to track changes in charge over time. Since the covalent linkage of the ECM has a direct effect on the charge of the systems, it is expected to see a decrease in charge over time as the pseudocapacitive component is lost (SI Figure 4.2).

Since lithium-based electrolytes in ECDs are known to degrade upon electrochemical cycling leading to the formation of lithium-containing films on flat CEs[97], the area of binding energy characteristic to Li 1s electrons was recorded for each ECM. While 20,000 cycles of the non-symmetric ECD did not result in lithium deposition on the electrodes, traces of lithium were detected on CE of the symmetric ECD after 50,000 cycles (Figure 4.4 E).

To further understand the cycling capabilities of these ECDs, galvanostatic charge-discharge measurements were performed using a potential window of 0 to 2 V at varying current densities (Figure 4.5). For both systems, symmetric/triangular shape is seen in the curves (Figure 4.5 A, D), indicating excellent reversibility. For both ECDs, a shoulder is seen in the curves at ~1 V as a result of faradaic charge storage. From these curves, the specific areal capacitance of the devices was determined using the following equation:

$$C = \frac{it}{VS}$$

Where *i* represents the current (mA), *t* is the time of discharge (s), *V* is the voltage window (V), and *S* is the geometric surface area of the electrode (cm^2). The Fe 4'T/ITO NPs ECD displays its greatest capacitance of 1.16 mF/cm^2 with an applied current density of 0.06 mA/cm^2, while the Fe 4'T Symmetric ECD displays a capacitance of 1.52 mF/cm^2 at the same current density (Figure 4.5 B, E). To observe charge-discharge performance, 10,000

charge-discharge cycles were performed with a current density of 0.06 mA/cm^2, from 0 to 2V (Figure 4.5 C, F). After cycling, we observed that the Fe 4'T/ITO NPs ECD was able to retain about 72% of the initial capacitance while the symmetric ECD retains close to 82% as a result of the advantageous device architecture, which limits the rate of cell degradation.

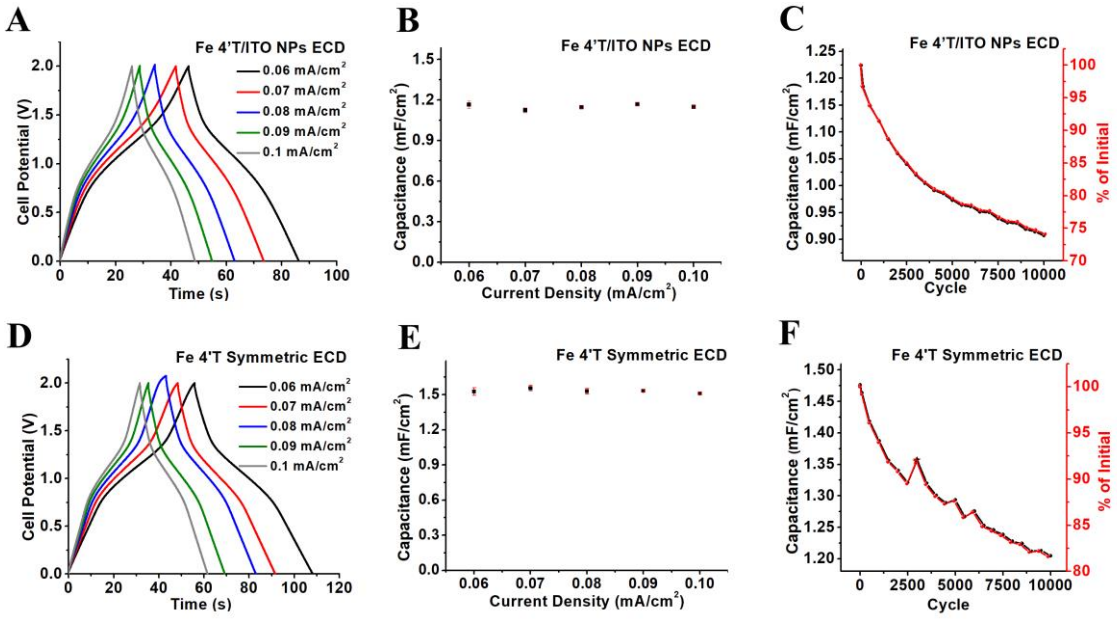

Figure 4.5. Galvanostatic charge-discharge (GCD) of Fe 4'T/ITO NPs **(A-C)** and Fe 4'T Symmetric **(D-F)**. **A, D)** GCD curves at different current densities. **B, E)** Capacitance dependence on applied current density as an average of 10 cycles. **C, F)** Capacitance retention of ECDs with an applied current density of 0.06 mA/cm^2 for 10,000 charge-discharge cycles. Note: The observable small kink in Figure 5F pointed with a star is due to a pause in the measurements due to a computer reset. As the device was not being cycled for a short period of time, there is a slight increase in the capacitance once the tests were restarted, which eventually settles out and continues to follow the previous trend.

After observing the improved stability and cycling lifetime of the above-mentioned ECDs through electrochemical measurements, we then investigated the optical properties of the Fe 4'T/ITO NPs ECD to compare to systems where a non-porous CE was employed. For this, a spectroelectrochemical analysis was performed, in which the device was

investigated using diffuse reflectance UV-vis spectroscopy while simultaneously changing the applied potentials.

UV-vis spectra were measured for the ECD at both the reduced (colored) and oxidized (bleached) states (Figure 4.6A). With an applied potential of 0 V, the WE of the ECD remains in its Fe^{2+} state, displaying a strong absorption peak at 600 nm caused by metal-to-ligand charge transfer (MLCT), i.e. a shift in electron charge-density from the metal's molecular orbital to that of the ligand.[18] With the application of 2 V, Fe^{2+} is oxidized to Fe^{3+} resulting in bleaching of the WE and disappearance of the MLCT absorption peak.

The change in optical density (ΔOD) of this system can be determined using the following equation:

$$\Delta OD = \log\left(\frac{T_b}{T_c}\right)$$

Where *T* is the transmittance of the ECD determined through conversion of the maximum and minimum absorbance values. An ideal ECD should have large ΔOD values indicating that there is significant contrast between the colored and bleached states. The color change of the device upon cycling can be easily seen with the naked eye (Figure 4.6A insert) and the Fe 4'T/ITO NPs ECD demonstrates significant (up to 40%) change in optical density. Spectroelectrochemical measurements for the Fe 4'T symmetric ECD were not performed due to color-bleed from the identically colored counter-electrode, limiting the change in optical density that can be obtained with the device.

Another important parameter of ECDs is the coloration efficiency, which represents the ratio between optical density and the injected charge. Ideally, a greater value for coloration efficiency is desired, as it indicates that a lower amount of charge is required to

create greater optical contrast. In contrast to metal-oxide-based ECDs[102], as well as ECDs based on triphenylamine polymers[88] and viologen derivative gels[103] with coloration efficiency values that rarely exceed 200 cm^2/C, ECDs based on metalorganic molecules[20, 37, 90] and polymers[37] often demonstrate higher values. The coloration efficiency of the device was determined from charge-optical density plot (Figure 4.6B) to be 210 cm^2/C. Although this value is lower than that reported for ECD systems with flat ITO CE or ECD with porous electron storage layer of TiO_2 on CE, the decrease in coloration efficiency for this system should be associated with the implementation of the ITO NPs layer on the CE.

Upon spectroelectrochemical cycling, the change in optical density remains identical when holding the device at each potential (0 and 2V) for 60 s and reducing the hold time up to 3.25 s. A further increase of the cycling speed results in slight ΔOD deterioration (Figure 4.6 C). Notably, the ECD can switch between redox states with speeds as fast as 1 s, with very little reduction to the ΔOD. This was the fastest switching of ECDs based on Fe 4'T ECM ever reported by us; for all previous ECDs configurations, a significant loss of optical density was observed when cycled with 7.5 second holds. In this particular case, surface-enhanced CE does not limit the rate of ion transport, allowing for the redox transition to occur much faster.

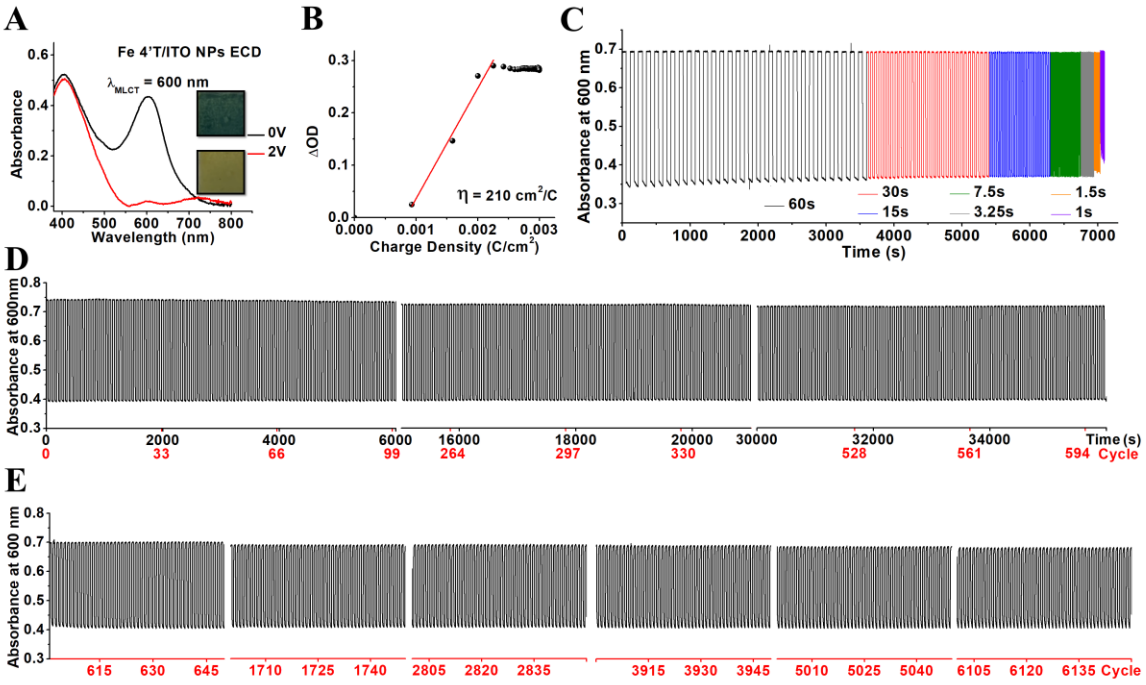

Figure 4.6. Spectroelectrochemistry of Fe 4'T/ITO NPs ECD: **A)** UV-vis absorbance spectra and photographs of ECD at oxidized (2 V) and reduced (0 V) states. **B)** Coloration efficiency (η) at 600 nm. **C)** Switching speeds at 600nm. **D)** The device was spectroelectrochemically cycled at 600 nm for 600 cycles (10 hrs. non-stop). Then, the device was stored for 3 months at ambient conditions, after which **E)** spectroelectrochemically cycling at 600 nm was continued to reach overall 6,000 cycles.

Spectroelectrochemical properties of the Fe 4'T/ITO NPs ECD which was cycled for 10 hrs, stored for 3 months at ambient conditions then cycled further remain nearly unchanged (Figure 4.6 D, E). Further spectroelectrochemical cycling demonstrates significant retention of the change in optical density. Thus the ΔOD after 6000 cycles was observed to be 28%, indicating a retention of 70%. As a result, the use of a high surface area ITO CE within the ECD allows for significantly enhanced optical properties, while improving the overall operational lifetime of the device.

4.5 Conclusions

Within this work, we have shown the importance of targeted design, optimization and detailed electrochemical analysis for electrochromic devices. We have discussed the importance of surface-enhanced electrodes for improved ion storage to prevent cell polarization and extend the cycling lifetime of an ECD. Furthermore, we have shown that electrochemical analyses such as CV and EIS can provide early monitoring and unambiguous identification of degradation pathways that cannot be detected solely through optical means. For instance, the Fe 4'T/ITO NPs and Fe 4'T Symmetric ECDs were operated for 20,000 cycles (28 days) and 50,000 cycles (69 days), respectively. By doing so, we were able to detect the degradation of the Fe 4'T electrochromic material that according to XPS elemental analysis, takes place via cleavage of the N-quaternized center in the molecule, resulting in the detachment of the EC molecule from the support. Prior to using enhanced-surface-area CEs reported here, the electrolyte and flat CE decomposition were the dominant weak points of these devices. As a result, the degradation pathway that includes the loss of electrochromic molecules from the surface was not previously observed. Regardless, the dissolution of EC molecules from the surface of ECM was shown to have little effect on the rate of redox-transition for both device architectures, while impedance data indicates minimal changes to the total layer resistance, electron mobility and conductivity of the systems after cycling. Additionally, we have employed galvanostatic charge-discharge cycling to measure the capacitance retentions of the systems after 10,000 charge-discharge cycles; the results of which have shown ~72% and 82% of initial capacitance retention for the Fe 4'T/ITO NPs and Fe 4'T Symmetric devices, respectively. Ultimately, the improved performance of the symmetric configuration can be

attributed directly to the device architecture. By employing identical materials at both the working and counter electrodes, there should be equal charge storage on each and, consequently, significantly boosted the overall charge density of the system. This results in a stable cell potential, that decreases the degradation of components such as the electrolyte, electrode and electrochromic material. We have shown that the electrochemical performance of these ECDs is also translated to the optical properties. By further investigating the Fe 4'T/ITO NPs ECD, we have shown that the device can achieve a decent coloration efficiency of 210 C/cm^2 at 600 nm with significantly improved switching rates (up to 1 s) when compared to a similar system without a surface-enhanced counter electrode.[18] Furthermore, we have shown that when cycling between colored (0 V) and bleached (2 V) states every 30 seconds, the device can be switched for 10 hours with only a 1.8% decrease in optical density. Although the optical properties of the Fe 4'T Symmetric ECD were not measured, the device showed optimal electrochemical durability compared to the Fe 4'T/ITO NPs ECD. As a result, this device architecture may be ideal for the future development of highly-durable double-sided electrochromic devices if the color-bleed from identically coloring counter electrodes can be minimized.

4.6 Acknowledgements

Financial support was provided by the National Sciences and Engineering Research Council of Canada through the Discovery Grants program (RGPIN-2020-05152, RGPIN-2016-05823) as well as Ontario Tech University. The authors acknowledge the Ontario Tech Science Materials Characterization Facility, which is supported by the Canada Foundation for Innovation (CFI), NSERC Research Tools and Instruments (RTI) and

Ontario Tech University. The authors also thank Dr. Peter M. Broderson at the Ontario Centre for the Characterization of Advanced Materials (OCCAM) at the University of Toronto (Toronto, ON, Canada) for performing XPS measurements.

4.7 Supplementary Information

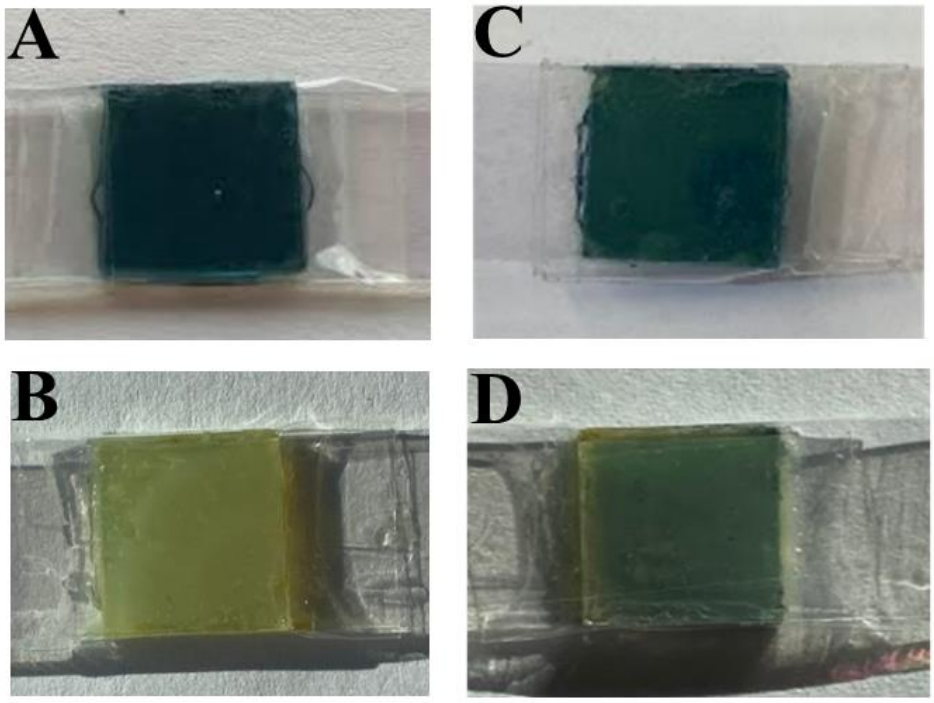

SI Figure 4.1. A) Pristine Fe 4'T/ITO NPs ECD. **B)** Fe 4'T/ITO NPs ECD after 20,000 cycles. **C)** Pristine Fe 4'T Symmetric ECD. **D)** Fe 4'T Symmetric ECD after 50,000 cycles. The photographs were taken when corresponding devices were not connected to any power supply.

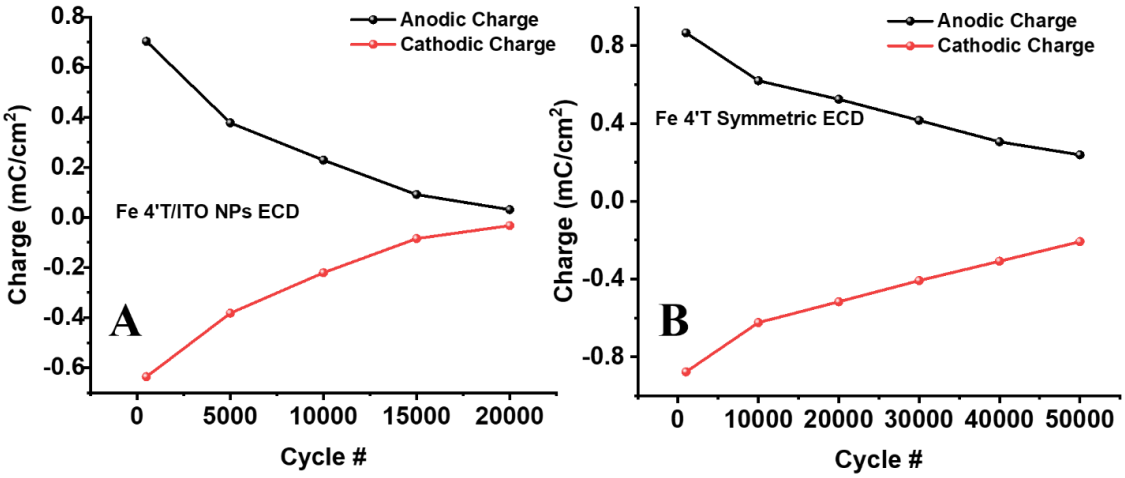

SI Figure 4.2. A) Charge vs Cycle number of Fe 4'T/ITO NPs ECD **B)** Charge vs Cycle number of Fe 4'T Symmetric ECD.

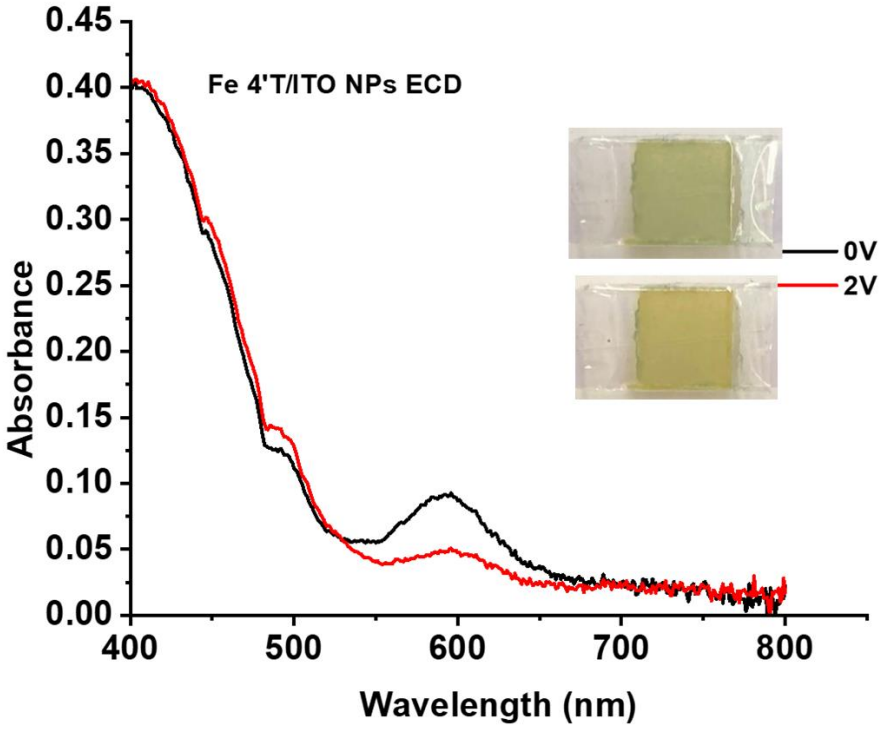

SI Figure 4.3. UV-visible diffuse reflectance spectrum of Fe 4'T/ITO NPs ECD after 20,000 cycles in the coloured (0 V) and bleached (2 V) state.

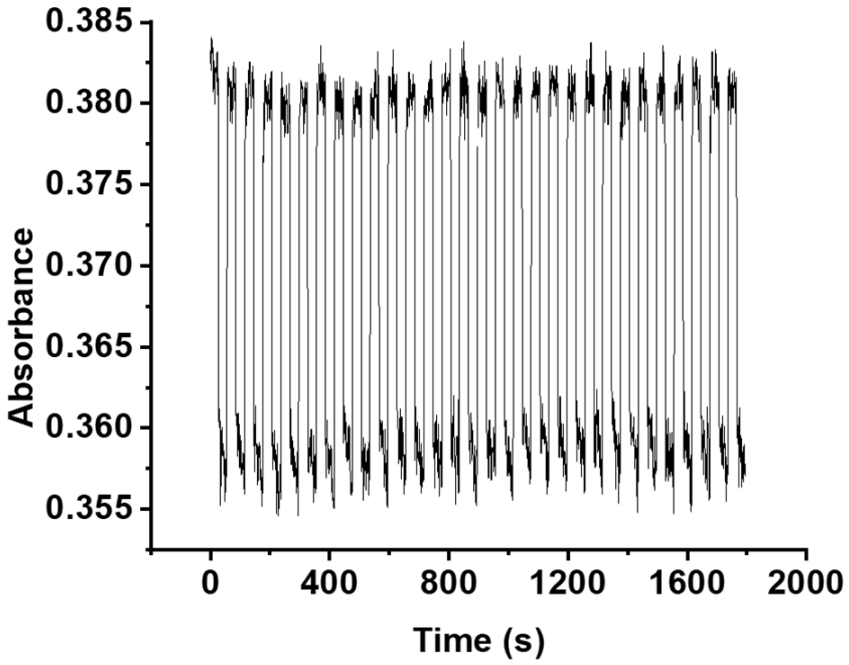

SI Figure 4.4. Spectroelectrochemical switching of the Fe 4'T/ITO NPs ECD after 20,000 cycles, performed with 30 s holds at 0 V and 2 V.

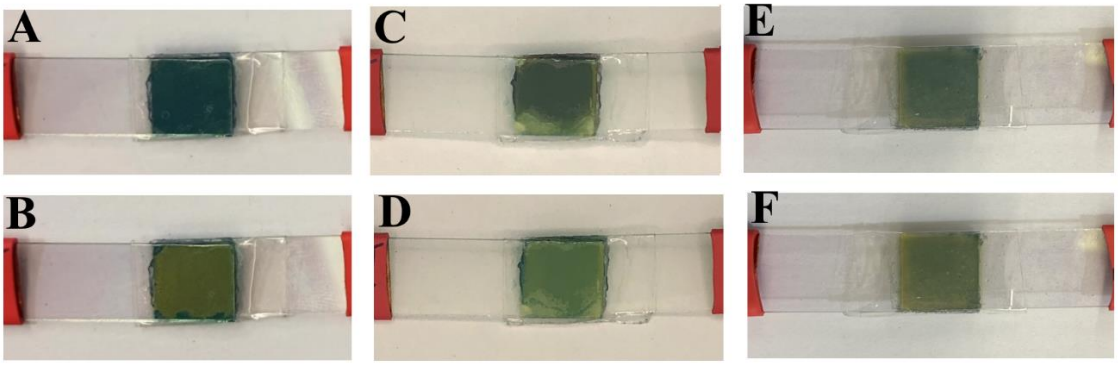

SI Figure 4.5. A) Pristine Fe 4'T Symmetric ECD at 0V. **B)** Pristine Fe 4'T Symmetric ECD at 2 V. **C)** Fe 4'T Symmetric ECD after 20,000 cycles of electrochemical switching at 0V. **D)** Fe 4'T Symmetric ECD after 20,000 cycles of electrochemical switching at 2V. **E)** Fe 4'T Symmetric ECD after 50,000 cycles of electrochemical switching at 0 V. **F)** Fe 4'T Symmetric ECD after 50,000 cycles of electrochemical switching at 2 V.

SI Table 4.1. RGB and L*a*b*values, colour, hue and colour differences (CDs) of electrochromic materials. Note: figures are taken fresh or disassembled and washed out of traces of electrolyte materials. See insets on Figure 4.4 for the actual images.

Material	R	G	B	L*	a*	b*	*Colour* /Hue	CD
ITO blank screen-printed film[90]	176	174	117	70.50	-9.50	29.70	*Pavlova*/Yellow[90]	-
Fresh Fe 4'T film-	20	42	67	16.90	0.05	-18.18	*Regal/blue*	72.5
WE of Fe 4'T/ITO NPs after 20,000 cycles	105	121	69	48.40	14.95	26.13	*Dingley*/green	33.2
CE of Fe 4'T/ITO NPs after 20,000 cycles	99	108	58	43.78	11.79	26.37	*Chalet Green* /green	34.3
WE- from Fe 4'T Symmetric after 50,000 cycles	90	112	65	44.44	16.91	23.11	*Chalet Green* /green	37.7
CE from Fe 4'T Symmetric after 50,000 cycles	46	77	56	29.85	16.66	8.57	*Goblin* /green	52.8

SI Table 4.2. RGB and L*a*b*values, colour, hue and colour differences of electrochromic devices.

Device	State	R	G	B	L*	a*	b*	Colour /Hue	CD
Fe 4'T/ITO NPs -ECD fresh	colored	30	61	59	23.44	-11.95	-2.70	*Blue Whale/ Blue*	43
	bleached	117	112	52	46.47	-6.57	33.24	*Himalaya/Yellow*	
Fe 4'T/ITO NPs -ECD after 20,000	colored	165	165	112	66.58	-8.20	26.98	*Green Smoke/Green*	
	bleached	181	167	98	68.27	-4.29	36.85	*Gimblet/Green*	10.7
Fe 4'T Symmetric-ECD fresh	colored	24	54	33	19.81	-16.89	9.59	*Deep Fir/Green*	
	bleached	79	79	38	32.69	-6.59	23.75	*Saratoga/Green*	21.7
Fe 4'T Symmetric -ECD after 20,000	colored	58	72	59	29.03	-8.47	5.62	*Timber Green/Green*	
	bleached	77	98	63	39.02	-14.93	17.04	*Tom Thumb/Green*	16.5
Fe 4'T Symmetric -ECD after 50,000	colored	46	64	49	25.17	-10.73	6.57	*Timber Green/Green*	
	bleached	84	92	63	37.66	-8.56	15.31		15.4

Chapter 5. Conclusions

Within this thesis, we have demonstrated the use of high-surface area CEs to allow for improved durability and performance when incorporated into a transition-metal based ECD architecture. By improving the properties of the CE, electrode potentials are better stabilized preventing unwanted degradation processes from occurring and allowing for drastically improved ECD lifetimes and improved optical properties.

In Chapter 3, comparisons between unmodified ITO glass substrates and highly porous modified substrates at the counter electrode were made. It was seen using XPS analysis that unmodified ITO glass undergoes irreversible reductive processes resulting in electrode and electrolyte degradation due to electrode polarization; this resulted in early device failure for ECDs that employed this material at the CE (Configuration 1). Alternatively, when materials with highly porous and capacitive properties were employed at the CE, these devices (configurations 2 and 3) showed exceptional stability with very little degradation during an identical cycling timescale of 3000 cycles. Furthermore, by rationally tuning the operating potential windows of the ECDs, we were able prevent unwanted side-reactions from occurring which may contribute to degradation and early device failure.

Chapter 4 builds upon the previous work by determining the cycling lifetime of the improved ECD configurations. Fe 4'T/ITO NPs and Fe 4'T Symmetric ECDs were cycled for a total of 28 days (20,000 cycles) and 69 days (50,000 cycles) of cycling respectively; a significant increase to the previously studied cycling times of 3000 cycles. By drastically increasing the amount of time the durable ECDs were cycled for, we were able to observe ECM degradation; a pathway that was previously obstructed due to more dominant

degradation of the electrolyte and electrode. By eliminating these degradation pathways, ECM degradation was observed to occur at a significantly slower timescale. This was confirmed by XPS analysis which shows that post-cycling, the ECM has been cleaved at the quaternary nitrogen and dissolved into the electrolyte. Furthermore, this work shows that these ECDs not only display an improvement in electrochemical properties, but an improvement in optical properties such as optical durability and Spectroelectrochemical switching speeds. In this case, the Fe 4'T/ITO-50 NPs ECD was able to switch as fast as every 1.5 s without affecting the optical density. Additionally, long-term optical durability showed minor decreases in optical density even after 6600 switching cycles, indicating these ECDs may be operated for longer periods of time before significant optical degradation is observed.

Future work that may build upon the research presented in this thesis may include investigating the impact of different electrolytes on ECD performance; by individually analyzing each component it may be possible to further improve upon the cycling lifetimes demonstrated here as well as better understand the effect of electrolyte composition. Furthermore, it may also be worth investigating different mechanisms to attach transition-metal complexes to the electrode surface in order to solve the issue of ECM cleavage. Lastly, the development of double-sided ECDs is rarely reported and may introduce new materials for applications outside of smart windows such as signage and displays.

REFERENCES

1. Larsen, M. A. D.; Petrović, S.; Radoszynski, A. M.; McKenna, R.; Balyk, O., Climate Change Impacts on Trends and Extremes in Future Heating and Cooling Demands over Europe. *Energy Build.* **2020,** *226*, 110397.

2. Somani, P. R.; Radhakrishnan, S., Electrochromic Materials and Devices: Present and Future. *Mater. Chem. Phys.* **2003,** *77* (1), 117-133.

3. Rauh, R. D., Electrochromic Windows: An Overview. *Electrochim. Acta* **1999,** *44* (18), 3165-3176.

4. Phan, G. T.; Pham, D. V.; Patil, R. A.; Tsai, C.-H.; Lai, C.-C.; Yeh, W.-C.; Liou, Y.; Ma, Y.-R., Fast-Switching Electrochromic Smart Windows Based on Nio-Nanorods Counter Electrode. *Sol. Energy Mater. Sol. Cells* **2021,** *231*, 111306.

5. Oh, M.; Roh, S.; Jang, M.; Park, J., Evaluation of Heating and Cooling Load According to Applying Electrochromic Glass to Office Building Envelope in South Korea. *International Journal of Sustainable Building Technology and Urban Development* **2018,** *9* (3), 158-169.

6. Mortimer, R. J.; Dyer, A. L.; Reynolds, J. R., Electrochromic Organic and Polymeric Materials for Display Applications. *Displays* **2006,** *27* (1), 2-18.

7. Deb, S. K., Optical and Photoelectric Properties and Colour Centres in Thin Films of Tungsten Oxide. *The Philosophical Magazine: A Journal of Theoretical Experimental and Applied Physics* **1973,** *27* (4), 801-822.

8. Granqvist, C.-G., Electrochromic Metal Oxides: An Introduction to Materials and Devices. In *Electrochromic Materials and Devices*, 2013; pp 1-40.

9. Granqvist, C. G., Electrochromic Tungsten Oxide Films: Review of Progress 1993–1998. *Sol. Energy Mater. Sol. Cells* **2000,** *60* (3), 201-262.

10. Wu, W.; Wang, M.; Ma, J.; Cao, Y.; Deng, Y., Electrochromic Metal Oxides: Recent Progress and Prospect. *Adv. Electron. Mater.* **2018,** *4* (8), 1800185.

11. Mortimer, R. J., Electrochromic Materials. *Annu. Rev. Mater. Res.* **2011,** *41* (1), 241-268.

12. Lu, H.; Li, X.; Lei, Q., Conjugated Conductive Polymer Materials and Its Applications: A Mini-Review. *Front. Chem.* **2021,** *9*, 732132.

13. Amb, C. M.; Dyer, A. L.; Reynolds, J. R., Navigating the Color Palette of Solution-Processable Electrochromic Polymers. *Chem. Mater.* **2010,** *23* (3), 397-415.

14. Sönmez, G.; Schwendeman, I.; Schottland, P.; Zong, K.; Reynolds, J. R., N-Substituted Poly(3,4-Propylenedioxypyrrole)S: High Gap and Low Redox Potential Switching Electroactive and Electrochromic Polymers. *Macromolecules* **2003,** *36* (3), 639-647.

15. Kawahara, J.; Ersman, P. A.; Engquist, I.; Berggren, M., Improving the Color Switch Contrast in Pedot:Pss-Based Electrochromic Displays. *Org. Electron.* **2012,** *13* (3), 469-474.

16. Nemani, S. K.; Chen, D.; Mohamed, M. H.; Sojoudi, H., Stretchable and Hydrophobic Electrochromic Devices Using Wrinkled Graphene and Pedot:Pss. *J. Nanomater.* **2018,** *2018*, 3230293.

17. Gomes, L.; Branco, A.; Moreira, T.; Feliciano, F.; Pinheiro, C.; Costa, C., Increasing the Electrical Conductivity of Electrochromic Pedot:Pss Films – a Comparative Study. *Sol. Energy Mater. Sol. Cells* **2016,** *144*, 631-640.

18. Laschuk, N. O.; Ebralidze, II; Poisson, J.; Egan, J. G.; Quaranta, S.; Allan, J. T. S.; Cusden, H.; Gaspari, F.; Naumkin, F. Y.; Easton, E. B.; Zenkina, O. V., Ligand Impact on Monolayer Electrochromic Material Properties. *ACS Appl. Mater. Interfaces* **2018,** *10* (41), 35334-35343.

19. Laschuk, N. O.; Ahmad, R.; Ebralidze, I. I.; Poisson, J.; Gaspari, F.; Easton, E. B.; Zenkina, O. V., Multiple Electrochemically Accessible Colour States in Surface-Confined Metal–Organic Monolayers: Stepwise Embedding of Individual Metal Centres. *Materials Advances* **2021,** *2* (3), 953-962.

20. Laschuk, N. O.; Ahmad, R.; Ebralidze, I. I.; Poisson, J.; Easton, E. B.; Zenkina, O. V., Multichromic Monolayer Terpyridine-Based Electrochromic Materials. *ACS Appl. Mater. Interfaces* **2020,** *12* (37), 41749-41757.

21. Bera, M. K.; Mori, T.; Yoshida, T.; Ariga, K.; Higuchi, M., Construction of Coordination Nanosheets Based on Tris(2,2′-Bipyridine)–Iron (Fe2+) Complexes as Potential Electrochromic Materials. *ACS Appl. Mater. Interfaces* **2019,** *11* (12), 11893-11903.

22. Takada, K.; Sakamoto, R.; Yi, S.-T.; Katagiri, S.; Kambe, T.; Nishihara, H., Electrochromic Bis(Terpyridine)Metal Complex Nanosheets. *J. Am. Chem. Soc.* **2015,** *137* (14), 4681-4689.

23. Elool Dov, N.; Shankar, S.; Cohen, D.; Bendikov, T.; Rechav, K.; Shimon, L. J. W.; Lahav, M.; van der Boom, M. E., Electrochromic Metallo-Organic Nanoscale Films: Fabrication, Color Range, and Devices. *J. Am. Chem. Soc.* **2017,** *139* (33), 11471-11481.

24. Choi, D.; Lee, M.; Kim, H.; Chu, W.-s.; Chun, D.-m.; Ahn, S.-H.; Lee, C. S., Investigation of Dry-Deposited Ion Storage Layers Using Various Oxide Particles to Enhance Electrochromic Performance. *Sol. Energy Mater. Sol. Cells* **2018,** *174*, 599-606.

25. Laschuk, N. O.; Ebralidze, I. I.; Easton, E. B.; Zenkina, O. V., Systematic Design of Electrochromic Energy Storage Devices Based on Metal–Organic Monolayers. *ACS Appl. Energy Mater.* **2021,** *4* (4), 3469-3479.

26. Cai, G.; Chen, J.; Xiong, J.; Lee-Sie Eh, A.; Wang, J.; Higuchi, M.; Lee, P. S., Molecular Level Assembly for High-Performance Flexible Electrochromic Energy-Storage Devices. *ACS Energy Lett.* **2020,** *5* (4), 1159-1166.

27. Liu, Y.; Sakamoto, R.; Ho, C.-L.; Nishihara, H.; Wong, W.-Y., Electrochromic Triphenylamine-Based Cobalt(Ii) Complex Nanosheets. *J. Mater. Chem. C* **2019,** *7* (30), 9159-9166.

28. Elgrishi, N.; Rountree, K. J.; McCarthy, B. D.; Rountree, E. S.; Eisenhart, T. T.; Dempsey, J. L., A Practical Beginner's Guide to Cyclic Voltammetry. *J. Chem. Educ.* **2018,** *95* (2), 197-206.

29. Laschuk, N. O.; Easton, E. B.; Zenkina, O. V., Reducing the Resistance for the Use of Electrochemical Impedance Spectroscopy Analysis in Materials Chemistry. *RSC Adv.* **2021,** *11* (45), 27925-27936.

30. Eric Shen, D.; Österholm, A. M.; Reynolds, J. R., Out of Sight but Not out of Mind: The Role of Counter Electrodes in Polymer-Based Solid-State Electrochromic Devices. *J. Mater. Chem. C* **2015,** *3* (37), 9715-9725.

31. Liu, L.; Yellinek, S.; Valdinger, I.; Donval, A.; Mandler, D., Important Implications of the Electrochemical Reduction of Ito. *Electrochim. Acta* **2015,** *176*, 1374-1381.

32. Macher, S.; Rumpel, M.; Schott, M.; Posset, U.; Giffin, G. A.; Löbmann, P., Avoiding Voltage-Induced Degradation in Pet-Ito-Based Flexible Electrochromic Devices. *ACS Appl. Mater. Interfaces* **2020,** *12* (32), 36695-36705.

33. Constable, E. C.; Thompson, A. M. W. C., Ligand Reactivity in Iron(Ii) Complexes of 4′-(4‴-Pyridyl)-2,2′ : 6′,2″-Terpyridine. *J. Chem. Soc., Dalton Trans.* **1992,** (20), 2947-2950.

34. Allan, J. T. S.; Quaranta, S.; Ebralidze, I. I.; Egan, J. G.; Poisson, J.; Laschuk, N. O.; Gaspari, F.; Easton, E. B.; Zenkina, O. V., Terpyridine-Based Monolayer Electrochromic Materials. *ACS Appl. Mater. Interfaces* **2017,** *9* (46), 40438-40445.

35. Choudhury, J.; Kaminker, R.; Motiei, L.; Ruiter, G. d.; Morozov, M.; Lupo, F.; Gulino, A.; Boom, M. E. v. d., Linear Vs Exponential Formation of Molecular-Based Assemblies. *J. Am. Chem. Soc.* **2010,** *132* (27), 9295-9297.

36. Motiei, L.; Altman, M.; Gupta, T.; Lupo, F.; Gulino, A.; Evmenenko, G.; Dutta, P.; van der Boom, M. E., Self-Propagating Assembly of a Molecular-Based Multilayer. *J. Am. Chem. Soc.* **2008,** *130* (28), 8913-8915.

37. Shankar, S.; Lahav, M.; van der Boom, M. E., Coordination-Based Molecular Assemblies as Electrochromic Materials: Ultra-High Switching Stability and Coloration Efficiencies. *J. Am. Chem. Soc.* **2015,** *137* (12), 4050-4053.

38. Wang, M.; Xing, X.; Perepichka, I. F.; Shi, Y.; Zhou, D.; Wu, P.; Meng, H., Electrochromic Smart Windows Can Achieve an Absolute Private State through Thermochromically Engineered Electrolyte. *Adv. Energy Mater.* **2019,** *9* (21).

39. Qiu, M.; Sun, P.; Zhang, B.; Yu, J.; Fu, Y.; Yu, X.; Zhao, C.; Mai, W., Reliable Information Encryption and Digital Display Applications Based on Multistate Smart Windows. *Adv. Opt. Mater.* **2018,** *6* (22), 1800338.

40. Granqvist, C. G.; Arvizu, M. A.; Bayrak Pehlivan, İ.; Qu, H. Y.; Wen, R. T.; Niklasson, G. A., Electrochromic Materials and Devices for Energy Efficiency and Human Comfort in Buildings: A Critical Review. *Electrochim. Acta* **2018,** *259*, 1170-1182.

41. Laschuk, N. O.; Obua, A.; Ebralidze, I. I.; Fruehwald, H. M.; Poisson, J.; Egan, J. G.; Gaspari, F.; Naumkin, F. Y.; Easton, E. B.; Zenkina, O. V., Spacer Conjugation and Surface Support Effects in Monolayer Electrochromic Materials. *ACS Appl. Electron. Mater.* **2019,** *1* (8), 1705-1717.

42. Liu, Q.; Xu, Z.; Qiu, W.; Hou, C.; Wang, Y.; Yao, P.; Yu, R.; Guo, W.; Liu, X. Y., Ultraflexible, Stretchable and Fast-Switching Electrochromic Devices with Enhanced Cycling Stability. *RSC Adv.* **2018,** *8* (33), 18690-18697.

43. Chen, Y.; Wu, Y.; Mechael, S. S.; Carmichael, T. B., Heterogeneous Surface Orientation of Solution-Deposited Gold Films Enables Retention of Conductivity with High Strain—a New Strategy for Stretchable Electronics. *Chem. Mater.* **2019,** *31* (6), 1920-1927.

44. Chen, W. H.; Li, F. W.; Liou, G. S., Novel Stretchable Ambipolar Electrochromic Devices Based on Highly Transparent Agnw/Pdms Hybrid Electrodes. *Adv. Opt. Mater.* **2019,** *7* (19).

45. Rai, V.; Singh, R. S.; Blackwood, D. J.; Zhili, D., A Review on Recent Advances in Electrochromic Devices: A Material Approach. *Adv. Eng. Mater.* **2020**.

46. Zhang, W.; Li, H.; Yu, W. W.; Elezzabi, A. Y., Transparent Inorganic Multicolour Displays Enabled by Zinc-Based Electrochromic Devices. *Light Sci. Appl.* **2020,** *9* (1).

47. Pugolovkin, L. V.; Cherstiouk, O. V.; Plyasova, L. M.; Molina, I. Y.; Kardash, T. Y.; Stonkus, O. A.; Yatsenko, D. A.; Kaichev, V. V.; Tsirlina, G. A., Electrodeposited Son-Stoichiometric Tungstic Acid for Electrochromic Applications: Film Growth Modes, Crystal Structure, Redox Behavior and Stability. *Appl. Surf. Sci.* **2016,** *388*, 786-793.

48. Kattouf, B.; Ein-Eli, Y.; Siegmann, A.; Frey, G. L., Hybrid Mesostructured Electrodes for Fast-Switching Proton-Based Solid State Electrochromic Devices. *J. Mater. Chem. C* **2013,** *1* (1), 151-159.

49. Wałęsa-Chorab, M.; Skene, W. G., Investigation of an Electroactive Immobilized Azomethine for Potential Electrochromic Use. *Sol. Energy Mater. Sol. Cells* **2019,** *200*, 109977.

50. Huang, Z.-j.; Mou, H.-r.; Xie, J.-p.; Li, F.; Gong, C.-B.; Tang, Q.; Fu, X.-K., Aie-Active Electrochromic Materials Based on Tetraphenylethylene Cored Benzoates with High Optical Contrast and Coloration Efficiency. *Sol. Energy Mater. Sol. Cells* **2020,** *206*.

51. Eisenberg, O.; Algavi, Y. M.; Weissman, H.; Narevicius, J.; Rybtchinski, B.; Lahav, M.; Boom, M. E., Dual Function Metallo–Organic Assemblies for Electrochromic–Hybrid Supercapacitors. *Adv. Mater. Interfaces* **2020**, 2000718.

52. Husson, J.; Abdeslam, E. T.; Guyard, L., A Missing Member in the Family of Chalcogenophene-Substituted 2,2′:6′,2″-Terpyridine: 4′-(Tellurophen-2-Yl)-2,2′:6′,2″-Terpyridine, Its Ru(Ii) Complex and Its Electropolymerization as a Thin Film. *J. Electroanalyt. Chem.* **2019,** *855*.

53. Laschuk, N. O.; Ebralidze, I. I.; Spasyuk, D.; Zenkina, O. V., Multi-Readout Logic Gate for the Selective Detection of Metal Ions at the Parts Per Billion Level. *Eur. J. Inorg. Chem.* **2016,** *2016* (22), 3530-3535.

54. Laschuk, N. O.; Ebralidze, I. I.; Quaranta, S.; T. W. Kerr, S.; Egan, J. G.; Gillis, S.; Gaspari, F.; Latini, A.; Zenkina, O. V., Rational Design of a Material for Rapid Colorimetric Fe^{2+} Detection. *Mater. Design* **2016,** *107*, 18-25.

55. Mondal, P. C.; Singh, V.; Jeyachandran, Y. L.; Zharnikov, M., Surface-Confined Heterometallic Triads on the Basis of Terpyridyl Complexes and Design of Molecular Logic Gates. *ACS Appl. Mater. Interfaces* **2015,** *7* (16), 8677-8686.

56. Poisson, J.; Geoffrey, H. L.; Ebralidze, I. I.; Laschuk, N. O.; Allan, J. T. S.; Deckert, A.; Easton, E. B.; Zenkina, O. V., Layer-by-Layer Assemblies of Coordinative Surface-Confined Electroactive Multilayers: Zigzag Vs Orthogonal Molecular Wires with Linear Vs Molecular Sponge Type of Growth. *J. Phys. Chem. C* **2018,** *122* (6), 3419-3427.

57. Malik, N.; Elool Dov, N.; de Ruiter, G.; Lahav, M.; van der Boom, M. E., On-Surface Self-Assembly of Stimuli-Responsive Metallo-Organic Films: Automated Ultrasonic Spray-Coating and Electrochromic Devices. *ACS Appl. Mater. Interfaces* **2019,** *11* (25), 22858-22868.

58. Munzert, S. M.; Stier, S. P.; Schwarz, G.; Weissman, H.; Rybtchinski, B.; Kurth, D. G., The Kinetics of Growth of Metallo-Supramolecular Polyelectrolytes in Solution. *Chem. Eur. J.* **2018,** *24* (12), 2898-2912.

59. Eh, A. L.-S.; Tan, A. W. M.; Cheng, X.; Magdassi, S.; Lee, P. S., Recent Advances in Flexible Electrochromic Devices: Prerequisites, Challenges, and Prospects. *Energy Tech.* **2018,** *6* (1), 33-45.

60. Chen, Y.; Carmichael, R. S.; Carmichael, T. B., Patterned, Flexible, and Stretchable Silver Nanowire/Polymer Composite Films as Transparent Conductive Electrodes. *ACS Appl. Mater. Interfaces* **2019,** *11* (34), 31210-31219.

61. Remmele, J.; Shen, D. E.; Mustonen, T.; Fruehauf, N., High Performance and Long-Term Stability in Ambiently Fabricated Segmented Solid-State Polymer Electrochromic Displays. *ACS Appl. Mater. Interfaces* **2015,** *7* (22), 12001-8.

62. Tsao, H. N.; Burschka, J.; Yi, C.; Kessler, F.; Nazeeruddin, M. K.; Grätzel, M., Influence of the Interfacial Charge-Transfer Resistance at the Counter Electrode in Dye-Sensitized Solar Cells Employing Cobalt Redox Shuttles. *Energy Environ. Sci.* **2011,** *4* (12).

63. Saleh, F. S.; Easton, E. B., Diagnosing Degradation within Pem Fuel Cell Catalyst Layers Using Electrochemical Impedance Spectroscopy. *J. Electrochem. Soc.* **2012,** *159* (5), B546-B553.

64. Bressers, P. M. M. C.; Meulenkamp, E. A., The Electrochromic Behavior of Indium Tin Oxide in Propylene Carbonate Solutions. *J. Electrochem. Soc.* **1998,** *145* (7), 2225.

65. Easton, E. B.; Pickup, P. G., An Electrochemical Impedance Spectroscopy Study of Fuel Cell Electrodes. *Electrochim. Acta* **2005,** *50* (12), 2469-2474.

66. Gasteiger, H. A.; Kocha, S. S.; Sompalli, B.; Wagner, F. T., Activity Benchmarks and Requirements for Pt, Pt-Alloy, and Non-Pt Oxygen Reduction Catalysts for Pemfcs. *Appl. Catal. B.* **2005,** *56* (1-2), 9-35.

67. Moghaddam, R. B.; Easton, E. B., The Interplay between Impedance Parameters, Structure, and Performance of Fuel Cell Catalyst Layers. *Chem. Eng. Sci.* **2020,** *224*.

68. Stranick, M. A.; Moskwa, A., Sno2 by Xps. *Surf. Sci.. Spectra* **1993,** *2* (1), 50-54.

69. Korotcenkov, G.; Brinzari, V.; Nehasil, V., Xps Study of Rh/In2o3 System. *Surf. Interfaces* **2021,** *22*, 100794.

70. Donley, C.; Dunphy, D.; Paine, D.; Carter, C.; Nebesny, K.; Lee, P.; Alloway, D.; Armstrong, N. R., Characterization of Indium−Tin Oxide Interfaces Using X-Ray Photoelectron Spectroscopy and Redox Processes of a Chemisorbed Probe Molecule: Effect of Surface Pretreatment Conditions. *Langmuir* **2002,** *18* (2), 450-457.

71. Charlton, M. R.; Suhr, K. J.; Holliday, B. J.; Stevenson, K. J., Electrochemical Modification of Indium Tin Oxide Using Di(4-Nitrophenyl) Iodonium Tetrafluoroborate. *Langmuir* **2015,** *31* (2), 695-702.

72. Dalby, K. N.; Nesbitt, H. W.; Zakaznova-Herzog, V. P.; King, P. L., Resolution of Bridging Oxygen Signals from O 1s Spectra of Silicate Glasses Using Xps: Implications for O and Si Speciation. *Geochim. Cosmochim. Acta* **2007,** *71* (17), 4297-4313.

73. Egan, J. G.; Hynes, A. J.; Fruehwald, H. M.; Ebralidze, I. I.; King, S. D.; Alipour Moghadam Esfahani, R.; Naumkin, F. Y.; Easton, E. B.; Zenkina, O. V., A Novel Material for the Detection and Removal of Mercury(Ii) Based on a 2,6-Bis(2-Thienyl)Pyridine Receptor. *J. Mater. Chem. C* **2019,** *7* (33), 10187-10195.

74. A. V. Naumkin, A. K.-V., S.W. Gaarenstroom, C.J.Powell, Nist X-Ray Photoelectron Spectroscopy Database. In *NIST Standard Reference Database Number 20*, National Institute of Standards and Technology, Gaithersburg MD, 20899 (2000): 2012.

75. Samadi Khoshkhoo, M.; Maiti, S.; Schreiber, F.; Chasse, T.; Scheele, M., Surface Functionalization with Copper Tetraaminophthalocyanine Enables Efficient Charge Transport in Indium Tin Oxide Nanocrystal Thin Films. *ACS Appl. Mater. Interfaces* **2017,** *9* (16), 14197-14206.

76. Kim, M.; Kim, J.; Cho, J.; Kim, H.; Lee, N.; Choi, B., A Study of the Characteristics of Indium Tin Oxide after Chlorine Electro-Chemical Treatment. *Mater. Res. Bull.* **2016,** *82*, 115-121.

77. Fruehwald, H. M.; Ebralidze, I. I.; Melino, P. D.; Zenkina, O. V.; Easton, E. B., Probing the Influence of the Carbon Support on the Activity of Fe-N3/C Model Active Sites for the Oxygen Reduction Reaction. *J. Electrochem. Soc.* **2020,** *167* (8), 084520.

78. Kuhn, H.; Andreaus, B.; Wokaun, A.; Scherer, G. G., Electrochemical Impedance Spectroscopy Applied to Polymer Electrolyte Fuel Cells with a Pseudo Reference Electrode Arrangement. *Electrochim. Acta* **2006,** *51* (8), 1622-1628.

79. Algharaibeh, Z.; Pickup, P. G., An Asymmetric Supercapacitor with Anthraquinone and Dihydroxybenzene Modified Carbon Fabric Electrodes. *Electrochem. Commun.* **2011,** *13* (2), 147-149.

80. Moghaddam, R. B.; Pickup, P. G., Electrochemical Impedance Study of the Polymerization of Pyrrole on High Surface Area Carbon Electrodes. *Phys. Chem. Chem. Phys.* **2010,** *12* (18).

81. Reid, O. O.; Saleh, F. S.; Easton, E. B., Application of the Transmission Line Eis Model to Fuel Cell Catalyst Layer Durability. *ECS Trans.* **2014,** *61* (23), 25-32.

82. Easton, E. B.; Fruehwald, H. M.; Randle, R.; Saleh, F. S.; Ebralidze, I. I., Probing the Degradation of Carbon Black Electrodes in the Presence of Chloride by Electrochemical Impedance Spectroscopy. *Carbon* **2020,** *162*, 502-509.

83. Alipour Moghadam Esfahani, R.; Fruehwald, H. M.; Laschuk, N. O.; Sullivan, M. T.; Egan, J. G.; Ebralidze, I. I.; Zenkina, O. V.; Easton, E. B., A Highly Durable N-Enriched Titanium Nanotube Suboxide Fuel Cell Catalyst Support. *Appl. Catal. B* **2020,** *263*.

84. Lu, Z.; Zhong, X.; Liu, X.; Wang, J.; Diao, X., Energy Storage Electrochromic Devices in the Era of Intelligent Automation. *Phys. Chem. Chem. Phys.* **2021,** *23* (26), 14126-14145.

85. Krebs, F. C., The New Black. *Nat. Mater.* **2008,** *7* (10), 766-767.

86. Zhang, Y.-M.; Wang, X.; Zhang, W.; Li, W.; Fang, X.; Yang, B.; Li, M.; Zhang, S. X.-A., A Single-Molecule Multicolor Electrochromic Device Generated through Medium Engineering. *Light Sci. Appl.* **2015,** *4* (2), e249-e249.

87. Chaudhary, A.; Pathak, D. K.; Tanwar, M.; Yogi, P.; Sagdeo, P. R.; Kumar, R., Polythiophene–Pcbm-Based All-Organic Electrochromic Device: Fast and Flexible. *ACS Appl. Electron. Mater.* **2019,** *1* (1), 58-63.

88. Chang, L.; Hou, Y.; Bai, J.; Xu, H.; Zhang, Y.; Miao, S.; Wang, C., Optoelectronic/Memory Storage Properties of Triphenylamine-Based Dual-Function Electrochromic Materials. *Mater. Chem. Phys.* **2022,** *275*, 125196.

89. Wang, K.; Meng, Q.; Wang, Q.; Zhang, W.; Guo, J.; Cao, S.; Elezzabi, A. Y.; Yu, W. W.; Liu, L.; Li, H., Advances in Energy-Efficient Plasmonic Electrochromic Smart Windows Based on Metal Oxide Nanocrystals. *Advanced Energy and Sustainability Research* **2021**.

90. Laschuk, N. O.; Ebralidze, II; Easton, E. B.; Zenkina, O. V., Post-Synthetic Color Tuning of the Ultra-Effective and Highly Stable Surface-Confined Electrochromic Monolayer: Shades of Green for Camouflage Materials. *ACS Appl. Mater. Interfaces* **2021,** *13* (33), 39573-39583.

91. Ebralidze, I. I.; Zenkina, O. V., Dynamic Electrochromic Play Via "Mix-and-Match" Reversible Metal-Ligand Interactions. *Chem* **2021,** *7* (5), 1146-1148.

92. Chen, X.; Dou, S.; Li, W.; Liu, D.; Zhang, Y.; Zhao, Y.; Li, Y.; Zhao, J.; Zhang, X., All Solid State Electrochromic Devices Based on the Lif Electrolyte. *ChemComm* **2020,** *56* (37), 5018-5021.

93. Guan, S.; Wang, W.; Zheng, J.; Xu, C., A Method to Achieve Full Incorporation of Pmma-Based Gel Electrolyte in Fiber-Structured Pvb for Solid-State Electrochromic Device Fabrication. *Electrochim. Acta* **2020,** *354*.

94. Leones, R.; Sabadini, R. C.; Sentanin, F. C.; Esperança, J. M. S. S.; Pawlicka, A.; Silva, M. M., Polymer Electrolytes for Electrochromic Devices through Solvent Casting and Sol-Gel Routes. *Sol. Energy Mater. Sol. Cells* **2017,** *169*, 98-106.

95. Eh, A. L.-S.; Tan, A. W. M.; Cheng, X.; Magdassi, S.; Lee, P. S., Recent Advances in Flexible Electrochromic Devices: Prerequisites, Challenges, and Prospects. *Energy Technology* **2018,** *6* (1), 33-45.

96. Wen, R. T.; Niklasson, G. A.; Granqvist, C. G., Strongly Improved Electrochemical Cycling Durability by Adding Iridium to Electrochromic Nickel Oxide Films. *ACS Appl. Mater. Interfaces* **2015,** *7* (18), 9319-22.

97. Ahmad, R.; Laschuk, N. O.; Ebralidze, I. I.; Zenkina, O. V.; Easton, E. B., Probing the Influence of Counter Electrode Structure on Electrochromic-Device Operating Potentials and Performance Using Electrochemical Impedance Spectroscopy. *ChemElectroChem* **2021,** *8* (12), 2193-2204.

98. Reid, O. R.; Saleh, F. S.; Easton, E. B., Determining Electrochemically Active Surface Area in Pem Fuel Cell Electrodes with Electrochemical Impedance Spectroscopy and Its Application to Catalyst Durability. *Electrochim. Acta* **2013,** *114*, 278-284.

99. Ebralidze, I. I.; Hanif, M.; Arjumand, R.; Azmi, A. A.; Dixon, D.; Cann, N. M.; Crudden, C. M.; Horton, J. H., Solvent Induced Adhesion Interactions between Dichlorotriazine Films. *J. Phys. Chem. C* **2012,** *116* (6), 4217-4223.

100. Keisar, H.; de Ruiter, G.; Velders, A. H.; Milko, P.; Gulino, A.; Evmenenko, G.; Shimon, L. J. W.; Diskin-Posner, Y.; Lahav, M.; van der Boom, M. E., Sorting of Molecular Building Blocks from Solution to Surface. *J. Am. Chem. Soc.* **2018,** *140* (26), 8162-8171.

101. Wagner, C. D.; Davis, L. E.; Zeller, M. V.; Taylor, J. A.; Raymond, R. H.; Gale, L. H., Empirical Atomic Sensitivity Factors for Quantitative Analysis by Electron Spectroscopy for Chemical Analysis. *Surf. Interface. Anal.* **1981,** *3* (5), 211-225.

102. Zhang, W.; Li, H.; Hopmann, E.; Elezzabi, A. Y., Nanostructured Inorganic Electrochromic Materials for Light Applications. *Nanophotonics* **2021,** *10* (2), 825-850.

103. Jang, Y. J.; Kim, S. Y.; Kim, Y. M.; Lee, J. K.; Moon, H. C., Unveiling the Diffusion-Controlled Operation Mechanism of All-in-One Type Electrochromic Supercapacitors: Overcoming Slow Dynamic Response with Ternary Gel Electrolytes. *Energy Storage Mater.* **2021,** *43*, 20-29.